

Università degli Studi di Trieste

FACOLTÀ DI SCIENZE MATEMATICHE FISICHE E NATURALI

Corso di Laurea Specialistica in Astrofisica e Fisica Spaziale

Analysis and characterization of thermal systematic effects on the PLANCK LFI data

Analisi e caratterizzazione degli effetti
sistematici di tipo termico sui dati di PLANCK - LFI

Tesi di Laurea di:
Tanja Petruševska

Relatore:
Dott.ssa Anna Gregorio
Correlatore:
Dott. Aniello Mennella

Contents

Abstract	1
1 Cosmic Microwave Background radiation	5
1.1 Introduction	5
1.2 Friedmann-Robertson-Walker Cosmological Model	6
1.3 Cosmic microwave background radiation	7
1.4 CMB anisotropies	8
1.5 Measuring the cosmic background radiation	16
2 CMB experiments	21
2.1 Introduction	21
2.2 Ground based experiments	21
2.3 Balloon-borne experiments	24
2.4 Satellite experiments	25
2.4.1 COBE	25
2.4.2 WMAP	27
3 The Planck mission	33
3.1 Introduction	33
3.2 The Planck satellite	34
3.2.1 Planck cryogenic system	35
3.2.2 High Frequency Instrument	38
3.2.3 Low Frequency Instrument	38
3.2.4 Systematic effects	42
3.3 Data processing	43
4 Assessment of thermal systematic effects on maps and power spectra	49
4.1 Characteristics of thermal systematic effects	51

4.1.1	Front-end temperature fluctuations	51
4.1.2	Back-end temperature fluctuations	51
4.1.3	4 K reference load temperature fluctuations	52
4.2	Time-ordered data generation	52
4.3	Destriping and map generation	54
5	Results and discussion	57
5.1	Back-end temperature fluctuations	57
5.1.1	Analysis of the period from OD 91 to OD 389	57
5.1.2	Analysis in the periods OD 91-115 and OD 275-389	65
5.2	Front-end temperature fluctuations	72
5.2.1	Analysis of the period from OD 91 to OD 389	72
5.2.2	Analysis in the periods OD 91-115 and OD 275-389	80
5.3	4 K reference load temperature fluctuations	85
5.3.1	Analysis of the period from OD 91 to OD 389	85
6	Conclusions and perspectives	97
	Appendix A	100
	Bibliography	106

Abstract

La radiazione cosmica di fondo nelle microonde scoperta nel 1965 da Penzias e Wilson, è considerata una delle più importanti prove sperimentali a favore del modello cosmologico standard noto come *Big Bang caldo*. Questa radiazione, fornisce un'immagine dell'Universo quando aveva circa 380.000 anni ed ha una distribuzione spettrale di corpo nero alla temperatura $T = 2.725 \pm 0.002$ K, indice dell'equilibrio termodinamico con la materia nell'epoca quando è stata rilasciata. La radiazione cosmica di fondo presenta anisotropie a livello di 10^{-5} che forniscono delle informazioni preziose riguardo l'origine e l'evoluzione dell'Universo.

Dopo la scoperta della radiazione di fondo, sono stati condotti decine di esperimenti per misurare la radiazione e le sue anisotropie. Nel 1992, il satellite COBE ha rivoluzionato la cosmologia rilevando queste anisotropie per la prima volta. Lanciata il 14 maggio 2009, *Planck* è una missione dell'Agenzia Spaziale Europea progettata per misurare le anisotropie della radiazione cosmica di fondo con una precisione senza precedenti. Planck osserva tutto il cielo con sensibilità $\Delta T/T \sim 2 \cdot 10^{-6}$, risoluzione angolare fino a $5'$ e copertura in 9 bande di frequenza da 30 a 857 GHz. Per raggiungere questi ambiziosi requisiti, Planck utilizza un sistema criogenico che raffredda gli strumenti fino a 0.1 K. L'elevata sensibilità dello strumento e il complesso sistema criogenico rende lo studio degli effetti termici sistematici (argomento principale di questa tesi) di importanza fondamentale per il successo scientifico della missione.

La tesi si articola in sei capitoli:

1. nel Capitolo 1 si presentano le proprietà della radiazione cosmica di fondo e le sue anisotropie;
2. nel Capitolo 2 si fa una breve panoramica dei vari esperimenti dedicati allo studio della radiazione cosmica di fondo;
3. nel Capitolo 3 si descrive la missione Planck, i suoi strumenti ed i suoi

scopi, in particolare lo strumento di bassa frequenza (Low Frequency Instrument, LFI) e la sua struttura termica;

4. nel Capitolo 4 si descrive l'analisi dei dati sulla stabilità termica dello strumento LFI di Planck. Il lavoro è stato effettuato presso il dipartimento di fisica dell'Università di Trieste e presso il Data Processing Centre di LFI situato presso INAF (Istituto Nazionale di AstroFisica) - OATS (Osservatorio Astronomico di Trieste).
5. nel Capitolo 5 si presentano i risultati di questa analisi;
6. nel Capitolo 6 si traggono le conclusioni e si mostrano le proposte per il futuro proseguimento del lavoro.

Abstract

The cosmic microwave background radiation discovered by Penzias and Wilson in 1965, is considered one of the most important experimental evidences in favour of the *Hot Big Bang* standard cosmological model. This radiation provides an image of the Universe when it was about 380,000 years old and has a blackbody spectral distribution at temperature $T=2.725\pm 0.002$ K, index of thermodynamic equilibrium with the mater in epoch when it was released. The cosmic background radiation presents anisotropies at level of 10^{-5} which provide valuable information about the origin and the evolution of the Universe.

After the discovery of background radiation, tens of experiments have been performed to measure this radiation and its anisotropies. In 1992 the COBE satellite revolutionized cosmology by detecting temperature anisotropies for the first time. Launched on May 14, 2009, *Planck* is a European Space Agency mission designed to measure the CMB anisotropies with an accuracy set by fundamental astrophysical limits. To do this, *Planck* is imaging the whole sky with an unprecedented combination of sensitivity ($\Delta T/T \sim 2 \cdot 10^{-6}$), angular resolution (to 5'), and 9 frequency coverage (30 – 857 GHz). To reach these ambitious requirements, *Planck* uses an active cryogenic thermal system which cools the instruments to 0.1 K. The high sensitivity of the instrument and the cryogenic system makes the thermal systematic effects study of crucial importance to the scientific success.

The thesis is divided into six chapters:

1. Chapter 1 explains the properties of the cosmic background radiation and its anisotropies;
2. Chapter 2 presents a short overview of the various experiments dedicated to the study of cosmic background radiation;
3. Chapter 3 describes the *Planck* mission, its instruments and its goals, in

particular the Low Frequency Instrument (LFI) and its thermal structure;

4. Chapter 4 discusses the analysis of the LFI thermal stability. This work was carried out in the Physics department at the University of Trieste, at the LFI Data Processing Centre located at INAF (Istituto Nazionale di AstroFisica) - OATS (Astronomical Observatory of Trieste);
5. Chapter 5 presents the results of this analysis;
6. in Chapter 6 conclusions are drawn and proposals for future work are discussed.

Chapter 1

Cosmic Microwave Background radiation

1.1 Introduction

In the past few decades, the field of cosmology has entered the era of the so called *precision cosmology*, going from a science in need for data in which often highly speculative theories went unconstrained to a research driven by experiments where many models have been ruled out leaving space for the *standard cosmology*. The Cosmic Microwave Background (CMB) is at the centre of this revolution as the one of the main instruments of the modern cosmology.

The standard cosmological model *Hot Big Bang* currently represents the best model to describe the origin and the evolution of the Universe. It is based on three observational evidences: the expansion of the Universe, the primordial nucleosynthesis and the cosmic microwave background. In this model the Universe began in a very hot, dense state from which it expanded and cooled. When the Universe was one millionth of its present size, the temperature would have been about 3 000 000 K: a temperature high enough that the typical energy of a photon in the thermal distribution was considerably more than the ionization energy of hydrogen atom. The Universe at that time was therefore a sea of free nuclei and electrons, and because photons interact strongly with free electrons via Thomson scattering, the mean free path of the photons was short. As the Universe expanded and cooled, the photons lost energy and became less and less able to ionize the forming atoms. Eventually all the electrons found their way into the ground state and the photons were no longer able to interact at all. When the Universe was 380000 years old,

it switched from being opaque to being completely transparent. Then, the photons were able to travel undisturbed for the rest of the Universe evolution. These photons are what today is observed as cosmic microwave background radiation.

The CMB is present today as a 2.7 K thermal background and it represents the most distant direct image of the Universe one *can* see. The microwave background visible today was once in thermal equilibrium with the primordial plasma of the Universe, and the Universe at that time was highly uniform. At the last-scattering redshift, gravitational instability theory says that fractional density perturbations must have existed in order for galaxies and clusters to form. The study of small temperature and polarisation fluctuations in the microwave background, which are only a few parts in 10^5 over the sky, are reflecting small variations in density and velocity in the early Universe, and have the potential to provide precise constraints on the overall properties of the Universe.

Table 1.1: *History of the early Universe evolution with the redshifts and times of the most relevant events for the CMB.*

Event	Redshift	Time
Today	$z = 0$	$t \sim 6(\Omega_M h^2)^{-1/2}$ Gyears
Recombination	$z \sim 1000$	$t \sim 200000(\Omega_M h^2)^{-1/2}$ years
Matter radiation equality	$z \sim 3100$	$t = 700(\Omega_M h^2)^{-2}$ years
CMB blackbody formed	$z \sim 10^7$	$t = 70(T/2.7)^{-2}$ hours
Big Bang nucleosynthesis	$z \sim 10^{10}$	$t = 10^{-2} - 10^2$ sec
Inflation		$t \sim 10^{-32}$ sec

1.2 Friedmann-Robertson-Walker Cosmological Model

The very existence of the microwave background provides crucial support for the *Hot Big Bang* cosmological model [1], [2]. This radiation appears to come from a spherical surface around the observer such that the radius of the shell is the distance each photon has travelled since it was last scattered at the epoch of recombination. This surface is what is called the *last scattering surface*.

The cosmological redshift z is defined in terms of the ratio between

observed wavelength and wavelength at emission:

$$1 + z = \frac{\lambda_{obs}}{\lambda_{em}} = \frac{a_{obs}}{a_{em}} \quad (1.1)$$

The cosmological expansion parameter $a(t)$ is a function of time that represents the relative expansion of the Universe. The formal description of the Universe at early epoch is described by the Robertson-Walker metric [3]:

$$-c^2 d\tau^2 = -c^2 dt^2 + a(t)^2 \left(\frac{dr^2}{1 - kr^2} + r^2(d\theta^2 + \sin^2\theta d\phi^2) \right) \quad (1.2)$$

Starting from the Robertson-Walker metric and applying the Einstein field equations to the Universe, the evolution of the cosmological scale factor $a(t)$ is obtained from the Friedmann equations [4]:

$$H^2 = \left(\frac{\dot{a}}{a} \right)^2 = \frac{8\pi G\rho}{3} - \frac{kc^2}{a^2} + \frac{\Lambda c^2}{3} \quad (1.3)$$

where k indicates the geometry of the space and Λ is the cosmological constant. From the Friedmann equations the critical density of the Universe can be defined $\rho_{cr} \equiv \frac{3H^2}{8\pi G}$ and the density parameter: $\Omega \equiv \frac{\rho}{\rho_{cr}} = \frac{8\pi G\rho}{3H^2}$. The different observations suggest that the geometry of the space is near to Euclidean [5], so $k = 0$. Together with the evidence that the contribution from the barionic Ω_b and dark matter is $\Omega_M \approx 0.3$, the contribution from dark energy should be $\Omega_\Lambda \approx 0.7$ [6]. The cold dark matter (Λ CDM) model gives a fairly definite and strikingly successful prescription for the initial conditions for this gravitational instability picture, and the Λ CDM model accordingly is widely used in analyses of structure formation.

1.3 Cosmic microwave background radiation

Since the 1940s, the existence of the cosmic microwave background radiation was theorised by different authors as an observable consequence of the Big Bang [7], [8]. Soon after it was figured out that the CMB frequencies are detectable from the Earth. In 1965, two radio astronomers at Bell Laboratories in New Jersey, Arno Penzias and Robert Wilson, using a sensitive microwave horn radiometers made the discovery almost by accident [9]. Even though was already predicted previously by different authors that a background radiation from the Big Bang should remain observable today, Penzias and Wilson received a Nobel prize in 1978 for its detection. The CMB has a thermal

spectrum of black body at a temperature of 2.725 ± 0.002 K, that peaks in the frequency of the microwave spectrum of 160.2 GHz, corresponding to a wavelength of 1.9 mm. In the early Universe, there were many interactions capable of thermalizing the background radiation. The expansion of the Universe does not change the blackbody nature of the spectrum, but cools the radiation such that the temperature at the epoch corresponding to redshift z is given by

$$T(z) = T_0(1 + z) \quad (1.4)$$

where T_0 is the present temperature and where $1 + z = \frac{a}{a_0}$. The most direct evidence that the redshift is a result of expansion is the thermal spectrum of the CMB. In the standard cosmological model the expansion of the Universe has two effects: it redshifts the photons, as $\lambda \propto a(t)$, and it dilutes the photon number density, as $n \propto a(t)^{-3}$.

1.4 CMB anisotropies

The CMB indeed is almost perfectly isotropic and homogeneous: in 1965, this property enabled Penzias and Wilson to distinguish the background radiation from radiation emitted by Earth's atmosphere. The CMB does have small variations in direction that are too small to have been detected in 1965: these departures from perfect isotropy provides some of the most important information available about the evolution of the Universe.

The usual procedure to describe the fluctuations in the temperature is to expand the distribution of T on the sky as a sum over spherical harmonics [2]:

$$\frac{\Delta T}{T}(\theta, \phi) = \sum_l \sum_{m=l} a_{lm} Y_{lm}(\mathbf{n}) \quad (1.5)$$

where θ e ϕ are the spherical coordinates, $l \approx 180^\circ / \Delta\theta$ represents the order of multipole and a_{lm} represents the moment multipole relative to a l and one of the $(2l + 1)$ values of m .

The term $\frac{\Delta T}{T}(\theta, \phi)$, with $l = 0$ is called *monopole*, which corresponds to the mean value of $\frac{\Delta T}{T}$ on sky background, which for definition, is zero. The ($l = 1$) term is called the *dipole* term which, as it can be seen in the next section, is attributable to our motion through space, so it is not of cosmological origin. The remaining modes, from the *quadrupole* ($l = 2$) and upwards, are usually attributed to intrinsic anisotropy produced by effects either at the time

of recombination or secondary anisotropies in the time afterwards. That is why the sum in equation (1.5) is generally taken over $l \geq 2$. If assumed that the processes are Gaussian, the variance can be defined as:

$$\langle a_{lm} a_{l'm'}^* \rangle = C_l \delta_{ll'} \delta_{mm'} \quad (1.6)$$

where $\delta_{ll'}$ is the Kronecker symbol and the average is taken over an ensemble of realisations. It can be showed that $\langle |a_{lm}|^2 \rangle$ depends only from l , and not from m for the rotational symmetry:

$$\langle |a_{lm}|^2 \rangle = a_l^2 = C_l \quad (1.7)$$

The quantity C_l is the angular power spectrum,

$$C_l \equiv \langle a_{lm}^2 \rangle \quad (1.8)$$

and if the processes are Gaussian, to define the properties of the CMB it is sufficient to know the C_l given that $\langle a_{lm} \rangle = 0$.

There is an intrinsic limit known as *cosmic variance* concerning the angular spectrum coefficients. Given that there is only one realisation of the Universe to observe, there is no certainty that the parameters obtained will be same as the ideal average of the ensemble of Universes realized with the same base cosmological parameters. On the other hand, one cannot average over positions from which to view the CMB and what is actually observed is a quantity averaged over m and not position. The fact that the a_{lm} coefficients are Gaussian distributed random variables, at a given l , and therefore their variance, C_l , is χ^2 distributed with $(2l + 1)$ degrees of freedom. The relative variance $\frac{\delta C_l}{C_l}$ is equal to $\sqrt{2/2l + 1}$ thus prevents high accuracy on the low l in the CMB power spectrum [10].

The cosmic microwave background shows a dipole anisotropy, which is usually interpreted as Doppler effect due to the motion of our Galaxy with respect to a cosmologically comoving frame in which the CMB is isotropic [11]. This can be expressed as:

$$T_{dipole} = T_0 \left(1 + \beta \cos\theta + \frac{1}{2} \beta^2 \cos 2\theta + \mathcal{O}^3 \right) \quad (1.9)$$

The dipole is proportional to $\cos\theta$, where θ is the angle between the observation and the direction of motion of the observer. The actual level of anisotropy is of order $\beta = v/c \sim 10^{-3}$. It was first discovered in 1969 by a ground-based

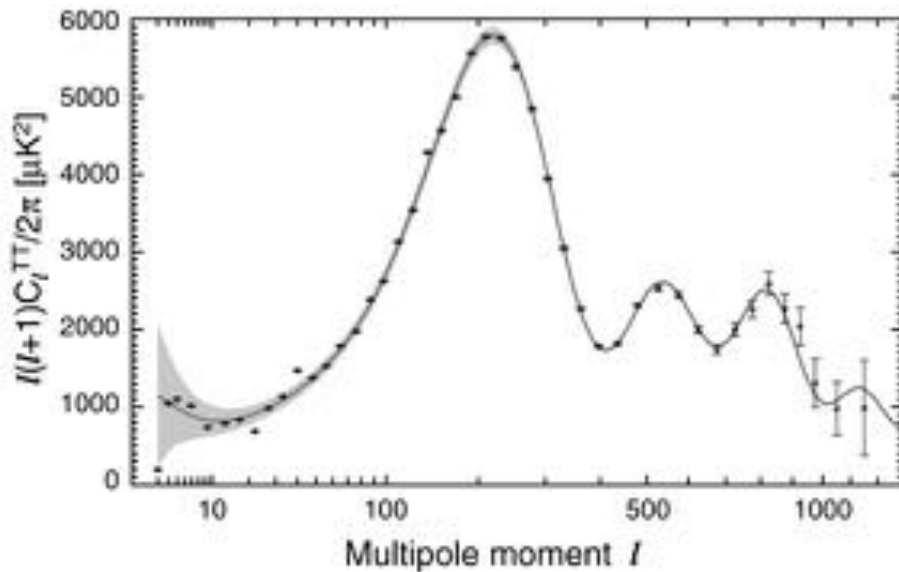


Figure 1.1: Angular power spectra for the CMB plotted against angular wavenumber l in radians^{-1} . The experimental data comes from different ground, balloon and satellite experiments, while the line represents the theoretical curve from the Λ CDM model.

radiometer, but the full velocity vector was measured in 1977 by a Berkeley group outside the Earth's atmosphere. COBE measured this component to be 3.372 ± 0.007 mK (Figure 1.2), but before the launch of the COBE mission, the dipole was the only temperature anisotropy detected in the CMB [12].

The anisotropies of the cosmic microwave background can be distinguished into primary and secondary [1]. Primary anisotropies are due to effects which occur at the last scattering surface and before, these are intrinsic anisotropies which have their origin in the early Universe. The secondary anisotropies are due to effects such as interactions with hot gas or gravitational potentials along the line of sight, between the last scattering surface and the observer.

There are three basic primary anisotropies which are important on respectively large, intermediate and small angular scales:

1. The gravitational redshift or blueshift due to fluctuations in the gravitational potential at last scattering dominant at $10 \leq l \leq 50$;

This is known as the *Sachs-Wolfe effect* [13] and it is a relativistic effect due to the fact that the photons that leave the last scattering surface meet on their line of travel a perturbation in the metric which change their frequency. It can be seen as a sum of two effects: the first as

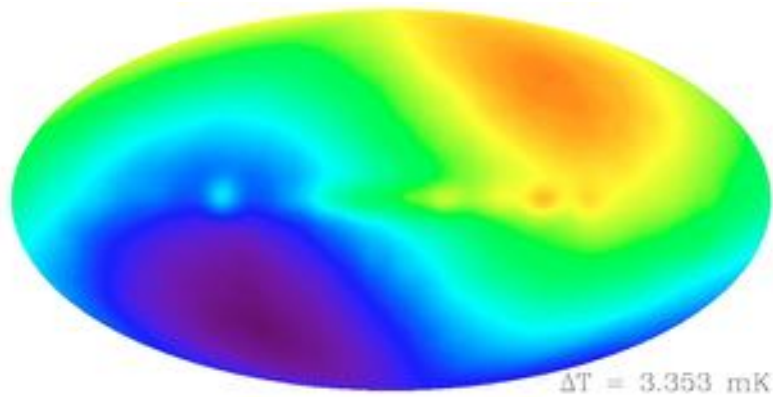


Figure 1.2: The dipole effect in the CMB imaged by COBE with $\Delta T = 3.372 \pm 0.007$ mK [11]. The overall variation indicate the CMB dipole. The faint features in the center of the map represent the plane of our Galaxy.

gravitational redshift and the second as temporal dilatation. The net effect of the potential perturbation at last scattering is:

$$\left(\frac{\Delta T(\mathbf{n})}{T_0}\right)_{SW} = \frac{1}{3}\delta\phi(\mathbf{n}_{rL}) \quad (1.10)$$

2. The acoustic peaks dominant at $100 \leq l \leq 1000$;

On sub-degree scales, the rich structure in the anisotropy spectrum is the consequence of gravity-driven acoustic oscillations occurring before the atoms in the universe became neutral. Perturbations inside the horizon at last scattering have been able to evolve causally and produce anisotropy at the last scattering epoch which reflects that evolution.

3. The damping tail dominant at $l \geq 1000$;

The recombination process is not instantaneous, giving a thickness to the last scattering surface. This leads to a damping of the anisotropies at the highest l , corresponding to scales smaller than that subtended by this thickness. The photon-baryon fluid had imperfect coupling, there is diffusion between the two components, and the oscillations have amplitudes that decrease with time. These effects lead to a damping of the angular power coefficients, called *Silk damping* [14].

Secondary anisotropies can be divided into two classes: those due to gravitational effects and those induced by scattering of the electrons. An important secondary gravitational effect which is not intrinsic of the surface of

last scattering is known as the *integrated Sachs-Wolfe effect* [13]. It is caused by gravitational redshifts or blueshifts due to time-dependent fluctuations in the gravitational potential between the time of last scattering and the present. This effects is dominant at large angular scales and is strongly dependent on the dark energy content of the Universe, but is unfortunately difficult to detect due to the presence of cosmic variance uncertainties at low multipoles.

In a variety of models of galaxy formation, it is likely that the intergalactic medium will become reionized at high redshift [15]. It is known empirically that in quasars such *reheating*, called *reionisation of the Universe* did occur at $z \geq 5$. What produced the required energy input into the intergalactic medium is not well understood; the most common suggestion is that the first generation of star formation was responsible. This reionization will introduce secondary anisotropies and their overall effect is to erase anisotropies that occur on smaller scales. While anisotropies on small scales are erased, polarization anisotropies are actually introduced due to the reionization. By looking at the observed CMB anisotropies, and comparing with what they would have look like if reionization not taken place, the electron column density at the time of reionization can be determined. With this, the age of the Universe when reionization occurred can be estimated.

There is another contribution to the secondary anisotropy of the CMB due to the inverse Compton scattering by electrons in intergalactic space within clusters of galaxies along the line of sight. This is known as the *Sunyaev-Zeldovich effect* [16]. In this case, a small percentage of the CMB photons from the Rayleigh-Jeans zone that encounter the hot gas electrons, gain energy so they bring the CMB spectrum peak to a higher energy. Given that the number of CMB photons at higher frequency is much smaller than the one at low frequency, besides the temperature drop in the Raleigh-Jeans there is a spectral distortion. This distortion at low frequency (Figure 1.3) is described by the parameter y which is related to the temperature drop, $\delta T/T = -2y$:

$$y = \int dt \sigma_T n_e(t) T_e / m_e \quad (1.11)$$

where n_e , T_e and m_e are the numerical density, temperature and mass of the electron, respectively. Galaxy clusters with an distance between 100 and 1000 h^{-1} Mpc make CMB anisotropies at $l \sim 600 - 6000$.

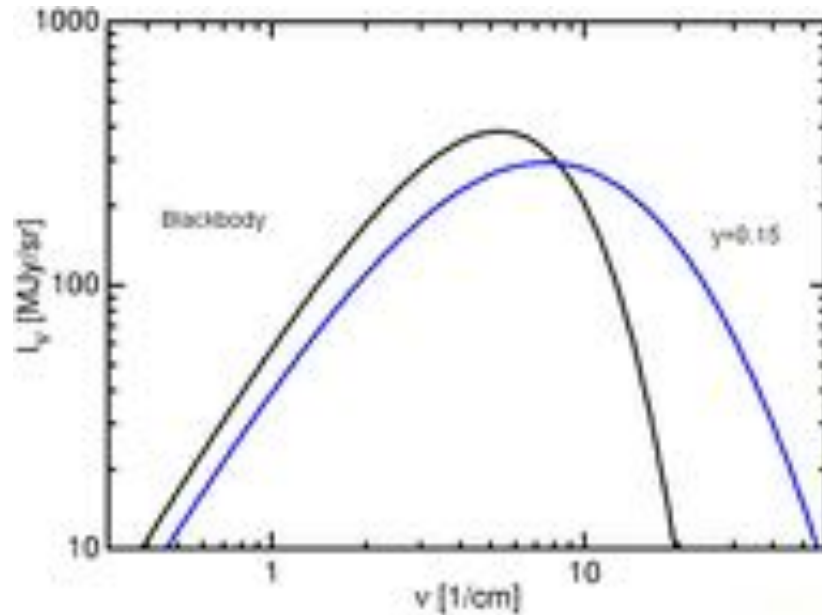


Figure 1.3: The Sunyaev-Zeldovich effect on the cosmic background radiation.

CMB polarisation

The cosmic microwave background is polarised at the level of a few μK due to the Thomson scattering of CMB photons at the last scattering surface [17]. The polarization pattern of the CMB (represented by the linear Stokes vector components Q and U) can be distinguished into divergence-free and curl-free components. The E-mode, or curl-free component, of the CMB polarization resulted from the Thomson scattering of CMB photons off of electrons in the anisotropic velocity field which was generated by quadrupolar fluctuations in density, and thus temperature, at the surface of last scattering and during reionization. E-mode polarization data used alone (the EE auto-correlation) and with temperature data (the TE cross-correlation) can improve our estimates of various cosmological parameters, in some cases breaking the degeneracies between parameters measured using CMB temperature anisotropy data alone. Although the E-mode polarization signal is weaker than that from the temperature anisotropies by roughly an order of magnitude, it has already been detected by a number of experiments.

The B-modes, which have not been measured and are thought to have an amplitude of at most a $0.1 \mu\text{K}$, are not produced from the plasma physics alone. Density perturbations cannot create B-type polarisation while

primordial gravity waves can. Detecting the B-modes will be extremely difficult, particularly given that the degree of foreground contamination is unknown, and the weak gravitational lensing signal mixes the relatively strong E-mode signal with the B-mode signal.

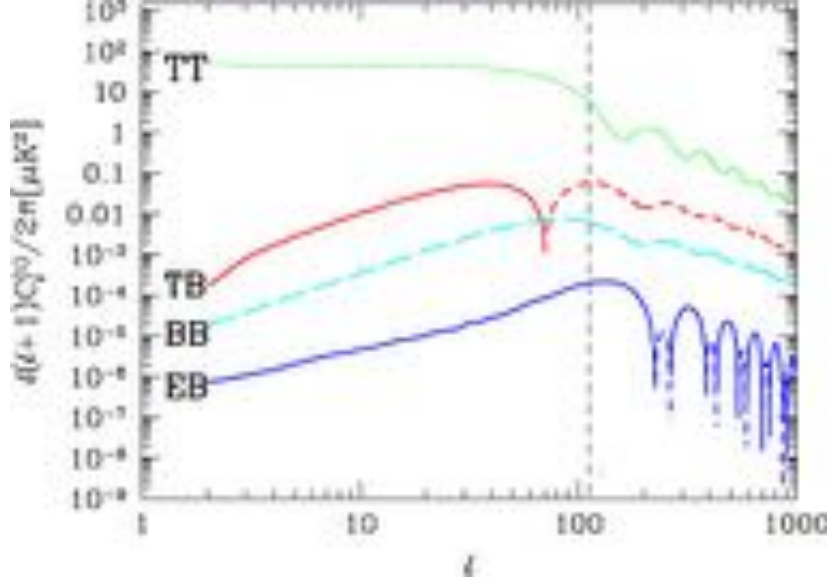


Figure 1.4: Simulated power spectrum (in a logarithmic scale) of the temperature anisotropy, polarization and their cross correlation.

The temperature and polarisation fields are partially correlated. The multipole moments are used to define the correlation power spectra:

$$\langle a_{lm}^{T*} a_{l'm'}^E \rangle = C_l^{TE} \delta_{ll'} \delta_{mm'} \quad (1.12)$$

$$\langle a_{lm}^{E*} a_{l'm'}^E \rangle = C_l^{EE} \delta_{ll'} \delta_{mm'} \quad (1.13)$$

$$\langle a_{lm}^{B*} a_{l'm'}^B \rangle = C_l^{BB} \delta_{ll'} \delta_{mm'} \quad (1.14)$$

On subdegree angular scale temperature, polarization and their cross correlation show acoustic oscillations (Figure 1.4), but in the polarization and cross correlation spectra the peaks are much sharper. The polarization is produced by velocity gradients of the photon-baryon fluid at the last scattering surface. The temperature receives contributions from density and velocity perturbations and these partially cancel each other making the features in the temperature spectrum less sharp. The dominant contribution to the temperature comes from the oscillations in the density, which are out of phase with the velocity.

Non Gaussianity

In the favoured model of structure formation driven by inflation (see Table 1.1), primordial fluctuations are expected to be Gaussian distributed [18]. In this case all the statistical information encoded into CMB anisotropies is completely described by their angular power spectrum C_l . The consistency test for an acceptable set of cosmological parameters is that one has to be able to assign a physically sensible initial condition that evolves into the present structure of the Universe. The inflationary models predict that the scalar component of the fluctuations obeys a power law:

$$P(k) \propto k^{n_s-1} \quad (1.15)$$

where k is the wavenumber of the fluctuations. For scalar fluctuations, n_s is referred to as the scalar spectral index, with $n_s = 1$ corresponding to scale invariant fluctuations. The statistical properties of the primordial fluctuations can be inferred from observations of anisotropies in the cosmic microwave background and from measurements of the distribution of matter, e.g., galaxy redshift surveys. Using the Sachs-Wolfe effect, a relation between the CMB power spectrum and the matter fluctuations spectrum can be found.

The values of cosmological parameters influence the shape of the C_l spectrum. The main features of the spectra in Figure 1.4 are the acoustic peaks. The CMB spectrum is mainly sensitive to six parameters, $\Omega_b h^2$ and $\Omega_M h^2$, the distance and the optical depth to the last scattering surface, amplitude and spectral index of the primordial gravitational potential power spectrum. The multipole number l is related to the first acoustical peak (Figure 1.1) by:

$$l_s \approx 200\sqrt{\Omega_M} \quad (1.16)$$

The dependence of $\Omega_b h^2$ and $\Omega_M h^2$ is not at all surprising, at high redshift the only relevant contributions to the energy density of the Universe comes from matter and radiation. The scaling of both the contributions from the cosmological constant and curvature makes them negligible at high redshift. This implies that there are certain degeneracies in the CMB data set because cosmological models with different parameters that keep the six combinations constant produce almost the same C_l spectra. That is why the CMB observations are needed to constrain the degeneracy in the cosmological parameters.

Although some inflation models predict potentially observable departures from Gaussianity on small angular scales ($l \geq 100$), no such non-Gaussianity has yet been found. The primary challenge in studies of non-Gaussianity is in choosing the statistics that quantifies it. The secondary challenge is to optimize the statistics against the Gaussian *noise* of the primary anisotropies and instrumental or astrophysical systematics. Most of the secondary anisotropies are not linear in nature and hence produce non-Gaussian signatures, so measuring non-Gaussianity in the gravitational and Sunyaev-Zeldovich effects in the CMB signal will be important for their isolation. The same is true for contaminants such as galactic and extragalactic foregrounds.

1.5 Measuring the cosmic background radiation

In this section the observational aspects of the CMB cosmology will be explained which leads to the subject of this thesis.

As mentioned before, there is an intrinsic limit in observing the CMB angular spectrum coefficients due to the the cosmic variance. Another unavoidable limit are the the astrophysical foregrounds: observing the CMB also means the ability of the instrument to separate the CMB from astrophysical foregrounds. The CMB anisotropy signal has proven to be dominant over a wide range of frequencies and angular scales while the other contributions, Galactic or extragalactic, in general have a different spectral dependence (as shown in Figure 1.5). While the peak of the CMB anisotropy intensity lies at about 90 GHz, other contributions dominate at other frequencies. Removal of the astrophysical foreground is of key importance for CMB polarisation measurements since Galactic emission dominates the polarised sky. Various astrophysical emission that interfere with the CMB detection can be distinguish in (Figure 1.6):

- Galactic synchrotron emission which dominates the microwave sky at $\nu \leq 10$ GHz
- Galactic free-free emission, important at $\nu > 30 - 60$ GHz where the Galactic signal dominates above the CMB signal.
- Galactic dust emission due to dust grains which changes according to the line of sight.

- Extragalactic sources, such as radio-galaxies, BL Lac objects, blazars and quasars.

Emission from dust (and dusty external galaxies) is expected to dominate the CMB at higher frequencies; synchrotron and free-free emission (and galaxies radiating by these methods) dominate at lower frequencies.

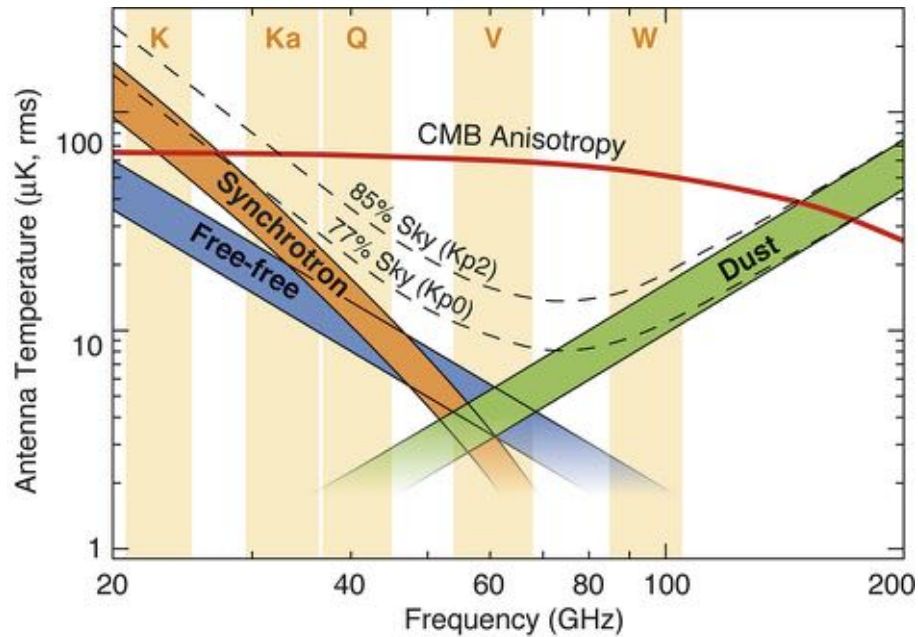


Figure 1.5: Foregrounds spectra compared to CMB one. Amplitudes are normalized to the Sachs-Wolfe plateau. Synchrotron and free-free are dominating at low frequency until 30 GHz. Dust is dominating at higher frequency (above 300 GHz)

The observational strategy of the sky is very important in a CMB experiment. Incomplete sky coverage (which is unavoidable for ground-based and balloon experiments) limits the statistical information about the power spectrum coefficients since it increases the sample variance and it smears out features in the power spectrum. Sky coverage is one of the main reason for planning a space mission.

The instrument related variance and systematics also affect the received CMB data. Detector sensitivity and angular resolution are key performance parameters [10]. Combining cosmic, sample and instrumental effects, assuming perfect foreground removal, ideal calibration and no systematic effects, the final

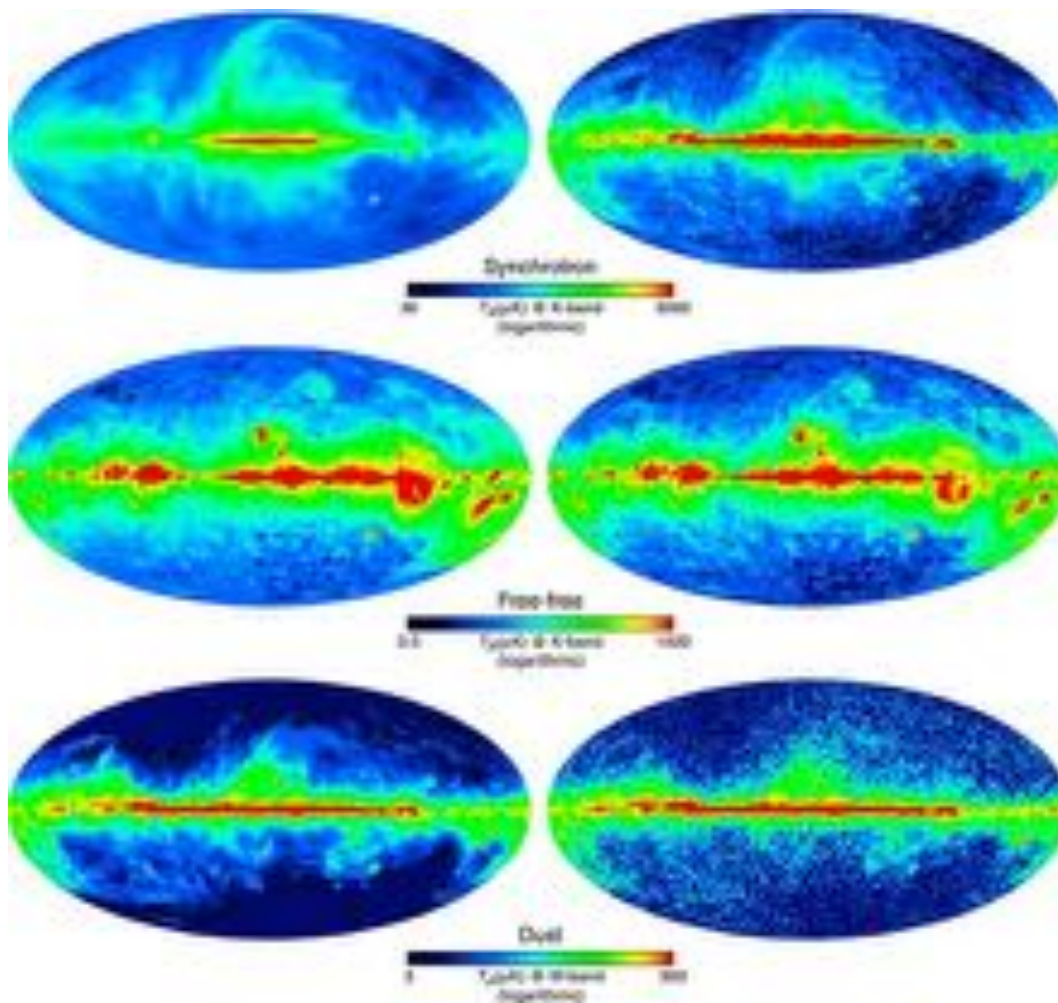


Figure 1.6: Foreground maps of different astrophysical components made by WMAP.

fractional error on the angular power coefficients can be written as follows [19]:

$$\frac{\delta C_l}{C_l} = \sqrt{\frac{2}{f_{sky}(2l+1)}} \left(1 + \frac{A\sigma^2}{N_{pix}C_lW_l} \right) \quad (1.17)$$

where f_{sky} is the fraction of the sky surveyed, A is the physical dimension of the surveyed area, σ is the root-mean-square noise per pixel, N_{pix} is the number of observed pixels and W_l represents the beam window function.

The main objective of an ideal CMB experiment is to map its temperature (and/or polarisation) anisotropy in the sky in order to accurately reconstruct the power spectrum, C_l , in the whole range of multipoles up to $l \sim 1500 - 2000$. To reach relative uncertainties $\frac{\delta C_l}{C_l}$ of order of 5% there are profound implications on the design of an instrument. In order to minimize the relative uncertainties $\frac{\delta C_l}{C_l}$, from equation 1.17 can be seen that it is necessary to have: *i*) full sky coverage which requires the experiment to be run from space, *ii*) a ~ 10 arc-minute angular resolution at (for example) 100 GHz requires the implementation of a reflector antenna with an aperture of the order of $\sim \lambda/\theta \sim 1.5$ m and *iii*) μ K sensitivity calls for multi-feed detector arrays operating at low temperatures with long integration times (≥ 1 year) [10].

It is not well standardized what represents the *systematic effect* in the CMB experiments. Regardless, various effects can be distinguished [10]:

- From ground, the detection of the Cosmic Microwave Background (CMB) anisotropy at the level $\Delta T/T \sim 10^{-5}$ is a challenging problem and a wide range of experimental difficulties occur when conceiving and building an experiment. The dominating source of contamination is the atmospheric emission, in particular the oxygen lines near 60 GHz make the atmosphere completely opaque at this important frequency, and much above 150 GHz the atmospheric windows are pretty opaque. For these reasons, balloon experiments still are important. However, if the atmospheric windows are used, much can be done from the ground, also because the atmosphere is almost completely unpolarized. For example, the cold weather, the thinner atmosphere and less water vapour makes the South Pole the favourite location for a ground-based CMB experiment.
- Deviations from ideality in the feed-horns, usually used in the observation in the CMB. There can be different effects related to optical effects due

to main beam distortions and side-lobe radiation. Main beam distortions come from deviations of the real main beams from perfect Gaussian beams and differences between beam shapes at the same frequency. These distortions result in a degradation of the angular resolution and sensitivity of the instrument. The side-lobe radiation instead rises from the radiation with a spurious provenience. This spurious radiation can be internal and external to the instrument; internal radiation can be due to the warm parts of the instrument, and the external to signals coming from celestial sources.

- Instrument intrinsic effects arising from the non-ideality of the radiometers or the bolometers themselves. For example, one of these is the noise intrinsic to all detectors, known as *1/f noise* or *Flicker noise* which is due to fluctuations in the mobility and/or of carriers of electrons. It is unknown the exact source of these fluctuations, but the fluctuations occur mainly in low frequencies. The $1/f$ is measured for every specific device, in particular the knee frequency which means the value when the $1/f$ graph approaches its limit. There are various techniques how to eliminate this noise in the CMB experiments.
- In the satellite missions, the pointing errors must be taken into account. The pointing errors depend on the limitations of the satellite attitude control system and on the ability to reconstruct the orientation of the beam using star sensors and instrument data.
- Systematic effects from the thermal and periodic fluctuations. In order to achieve a 10^{-5} sensitivity in the anisotropy detection, a cryogenic thermal design is needed. This implies a rigorous control of the systematic effects due to the various temperature fluctuations.

The work of this thesis concentrates on the thermal systematic effects from the Low Frequency Instrument of the Planck mission. Planck uses an active cryogenic thermal system which cools the instruments to 0.1 K. The high sensitivity of the instrument and the cryogenic system makes the thermal systematic effects of crucial importance to the scientific success.

Chapter 2

CMB experiments

2.1 Introduction

Since its discovery in 1965, it has been dedicated a lot of attention in studying the CMB with more than 40 experiments involved. Nevertheless, the CMB anisotropies remained undiscovered until 1992, when the first results from COBE satellite confirmed their existence. COBE gave information only about the anisotropy for relatively small l , well below the first acoustic peak at $l \sim 200$ [12]. This discovery was followed by a series of balloon and ground-based observations, which gave definite evidence for the first acoustic peak, and some data on higher peaks extending up to values of l beyond the position of the fifth acoustic peak, at $l \sim 1400$ [20]. The accuracy of these measurements up to about $l \sim 600$ was then greatly improved by observations performed by the satellite mission WMAP. NASA's Wilkinson Microwave Anisotropy Probe (WMAP) established that our Universe is close to spatially flat, it provided compelling evidence that our Universe is dominated by dark energy and dark matter and that present-day structure grew from nearly scale invariant primordial fluctuations. Furthermore, the third CMB mission generation ESA's *Planck* with its improved resolution, sensitivity and multi frequency band coverage will outcome COBE and WMAP by measuring the CMB fluctuations with accuracy set by fundamental astrophysical limits.

2.2 Ground based experiments

The solution for a ground-based experiment is to run it at a suitable frequency so that the contamination is kept low. There is a window between ~ 10 and ~ 40 GHz where both atmospheric and galactic emissions should be lower than

the typical CMB flux. For example, the Tenerife experiments were running at 10, 15 and 33 GHz and the Cambridge Cosmic Anisotropy Telescope (CAT) at 15 GHz (Table 2.1). However, in order to reach the level of accuracy needed, spectral discrimination of foregrounds using multi-frequency data is necessary. Concerning the atmospheric emission, in particular at frequencies higher than ~ 10 GHz, three basic techniques, which are all still being used, have been developed in order to fight against the atmospheric emission problem [20]:

- The Tenerife experiments used the *switched beam method*. In this case the telescope switches rapidly between two or more beams so that a differential measurement can be made between two different patches of the sky, allowing one to filter out the atmospheric variations.
- A more modern and flexible version of the switched beam method is the *scanned beam method* (e.g. Saskatoon and Python telescopes). These systems have a single receiver in front of which a continuously moving mirror allows scanning different patches of the sky. The motion pattern of the mirror can be resynthesised by software. This technique provides a great flexibility regarding the angular-scale of the observations.
- An alternative to differential measurement is the use of interferometric techniques. Here, the output signals from each of the baseline horns are cross-correlated so that the Fourier coefficients of the sky are measured. The projects such as the Cosmic Background Imager (CBI), Cosmic Anisotropy Telescope (CAT), Very Small Array (VSA) and the Very Compact Array (VCA/DASI) are also using this technique.

A number of ground-based interferometers provided measurements of the CMB anisotropies and polarisation: the Very Small Array (VSA), Degree Angular Scale Interferometer (DASI) and the Cosmic Background Imager (CBI).

The Cosmic Anisotropy Telescope (CAT) [21] was a three-element interferometer at 13 to 17 GHz based at the Mullard Radio Astronomy Observatory in England in the period 1994–1997. It had observing bandwidth of 500 MHz and a system temperature of 50 K. The CAT simultaneously recorded data from orthogonal linear polarisations. Its first results, published in 1996, were the highest resolution CMB detection at that time, and showed that the rise in fluctuation power towards scales of $\sim 1^\circ$ ($l \sim 200$) and a decline

Table 2.1: *Performance of a selection of ground-based CMB experiments (T stands for Temperature, P for Polarisation)*

Experiment	Frequency (GHz)	Angular Resolution ($^{\circ}$)	Scales (l)	Measured quantity
MAT	30 – 140	0.1 – 60	30 – 1100	T
VSA	26 – 36	0.1 – 60	30 – 1100	T
Ryle	15	0.023 – 0.05	4000 – 8000	T
Viper	90	0.45 – 9	20 – 400	T
White Dish	90	0.21 – 0.47	381 – 851	T
CBI	26 – 36	0.08 – 1.0	300 – 3000	T
DASI	26 – 36	0.25 – 1.15	125 – 700	P
ATCA	9	0.03 – 0.05	3500 – 5780	T
SuZIE	150 – 350	0.05 – 0.18	1000 – 3700	P
VLA	5, 8, 15	0.02 – 0.04	5000 – 9000	P
POLAR	26 – 46	6 – 90	2 – 30	P
Polatron	100	0.09 – 0.9	200 – 2000	T
Saskatoon	26 – 46	0.45 – 3.46	502 – 401R	T
Phyton	30 – 90	0.75 – 3.27	55 – 240	T
CAT	13 – 17	0.25 – 0.53	339 – 722	T
OVRO	20	0.07 – 0.16	1100 – 2750	P
DIMES	2 – 100	10	18	P
Tenerife	10 – 15 – 33	0.1 – 5	13 – 30	P

in power at smaller angles ($l = 500 - 700$), thus showing the existence of the long-predicted acoustic peaks in the CMB power spectrum. Further results were published in 1999.

The Very Small Array [22] is a 14-element radio interferometer operating between 26-36 GHz, designed expressly to perform high resolution observations of the CMB on angular scales around and below one degree. The design of the VSA is strongly based on the previous successful CMB imaging experiment CAT. The key results were the CMB power spectra between multipoles of 150 and 900, and the resulting limits on cosmological parameters when combined with observational data from other experiments. The second observing session produced an improved power spectrum of the CMB, going up to a multipole of 1400 and refined cosmological parameters.

The Cosmic Background Imager (CBI) [23], operative from 2002, is located at an altitude of 5080 meters near San Pedro de Atacama, in northern Chile. The CBI is a 13-element interferometer mounted on a 6 meter platform operating in ten 1-GHz frequency bands from 26 GHz to 36 GHz. The instantaneous field of view of the instrument is 44' and its resolution ranges

from 4.5 to 10'. It consists of HEMT amplifiers, cooled to 6 K. Unresolved extragalactic sources are measured with the 40 meter telescope at the Owens Valley Radio Observatory, and subtracted from the CBI images. The CBI shares many design elements with DASI, an interferometer that probes larger angular scales.

The Degree Angular Scale Interferometer (DASI) [24] was a experiment located in Antarctica operative from 2001 to 2003 and developed by a collaboration between the University of Chicago and CalTech. It is a 13-element interferometer operating between 26 and 36 GHz in ten bands. Each element consists of a 20 cm diameter corrugated feed horn, cryogenically cooled 4-stage InP HEMT amplifier. Receiver temperatures range between 18 – 25 K at the center of the band, including the warm lens, feed horn and throat, and cold isolator and polarizer. The greatest result of DASI was in 2002 when the team reported discovery of the CMB polarization.

2.3 Balloon-borne experiments

An economic solution consists in using high altitude balloon flights, generally at around 40,000 metres above the surface where it is possible to reduce the atmospheric absorption of microwave radiation to a minimum. There have been many balloon-borne experiments (Table 2.2), but the most remarkable are MAXIMA and BOOMERanG.

Table 2.2: *Performance of balloon-borne CMB experiments*

Experiment	Year	Frequency (GHz)	Scales (l)
FIRS	1989	3 – 29	170 – 680
Argo	1988, 1990, 1993	150 – 600	53 – 180
MSAM	1992 – 1997	69 – 362	150 – 650
MAXIMA	1995, 1998, 1999	50 – 70	150 – 420
QMAP	1996	30 – 850	30 – 140
Archeops	1999 – 2002	143, 217, 353, 545	10 – 700
Bam	1995	30 – 100	110 – 250
BOOMERanG	1997 – 2003	25 – 1025	90 – 420
PIQUE	2002	69 – 362	90
TopHat	2002 – 2004	10 – 700	150 – 720
EBEX	Future	25 – 1000	150 – 450

The *Millimeter Anisotropy eXperiment IMaging Array* (MAXIMA) [25] consisted of two flights, one in 1998 and one in 1999. For each flight the

balloon was sent at the US territory and for over 8 hours took data from about 0.3 percent of the sky. A 1.3-m primary mirror, along with a smaller secondary and tertiary mirror, was used to focus the microwaves onto the feed horns, then a bolometer array measured the incident radiation. The feed horns had spectral bands centred at 150, 240 and 420 GHz with a resolution of 10 arcminutes. By the end of the year 2000 the experiment provided the most accurate measurements of the CMB fluctuations on small angular scales. With these data it was possible to calculate the first three acoustic peaks from the CMB power spectrum.

The BOOMERanG experiment [26] (Balloon Observations Of Millimetric Extragalactic Radiation and Geophysics) was a project of Caltech and the University of Rome La Sapienza. The BOOMERanG flew around Antarctica, carried by a stratospheric long-duration balloon in 1998 and 2003. It flew on an altitude of 37 km carrying a telescope of a 1.3 m off-axis paraboloidal mirror feeding a pair of cold (1.5 K) ellipsoidal mirrors which re-image the prime focus onto an array of feed horns. These concentrate the incoming radiation onto bolometric detectors, cooled to 0.28 K by a helium refrigerator. It operated on four frequencies: 90, 150, 240 and 400 GHz with angular resolution of 0.30, 0.17, 0.23 and 0.22 degrees respectively. BOOMERanG covered only 3% of the whole sky. It was the first experiment, in 1998, to map out the structure of the anisotropies on angular scales from several degrees down to 10 arcminutes, and in doing so provided the first convincing evidence that the geometry of the Universe was close to spatial flatness.

2.4 Satellite experiments

There is a great advantage of going into space: the atmospheric thermal emission is avoided and it is possible to get a whole coverage of the sky. A space mission is highly costly and complex to achieve, so it takes several years from the planning to the launching of the satellite.

2.4.1 COBE

The COBE satellite was launched in 1989 and in 1992 revolutionized cosmology by detecting CMB temperature anisotropies for the first time. For this discovery in 2006 John Mather and George Smoot received a Nobel prize.

COBE [12] is an acronym for NASA's COsmic Background Explorer

satellite. Its orbit nearly passed over the Earth's poles at an altitude of 900 km. The orbital plane was inclined by 99° to the Equator, causing the orbit to precess to follow the apparent motion of the Sun relative to the Earth. The spin axis stayed pointed almost perpendicular to the direction of the Sun and in a generally outward direction from the Earth. As the COBE orbited the Earth once every 103 minutes, it was viewing a circle on the sky 94° away from the Sun, and as the Earth moves around the Sun over one year the COBE gradually scanned the entire sky.

COBE actually carried on several experiments (as shown in Figure 2.1) to probe the large-scale radiation field over the wavelength range $1 \mu\text{m}$ to 1 cm :

- Differential Microwave Radiometer (DMR) - a microwave instrument to map the anisotropies in the CMB. The DMR experiment produced a map of the sky,
- Far-InfraRed Absolute Spectrophotometer (FIRAS) - a spectrophotometer used to measure the spectrum of the CMB,
- Diffuse InfraRed Background Experiment (DIRBE) - a multiwavelength infrared detector used to map dust emission.

The DMR detector consists of two horns at an angle of 60° ; a radiometer measures the difference in temperature between these two horns. There were six differential radiometers, two channels at each of three frequencies: 31.5, 53 and 90 GHz, respectively. These frequencies were chosen in a way to allow measurements where the CMB signal is maximum, while the various sources of galactic emission, such as dust and synchrotron radiation are low. For DMR the objective was to search anisotropies at these three frequencies in the CMB with an angular resolution of about 7° (Figure 2.3). For FIRAS the objective was to measure the spectral distribution of the CMB in the range $0.1 - 10 \text{ mm}$ and compare it with the black-body form expected from the Big Bang model. FIRAS had two separate interferometers measuring the difference between the sky signal and an on-board blackbody calibrator. For DIRBE, the objective was to measure the infrared background radiation.

After 4 years since its launch, COBE was a great success. It gave values of C_l measured from $l = 2$ to $l = 40$. Predictions of the Big Bang were confirmed: temperature fluctuation of order 10^{-5} were found and the CMB

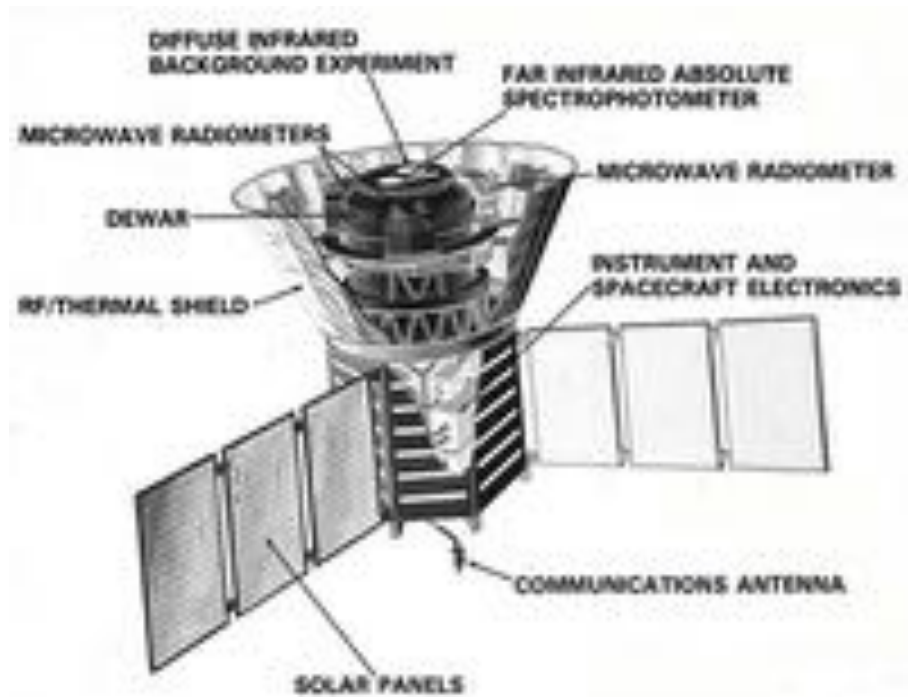


Figure 2.1: Scheme of the COBE spacecraft

with a temperature of 2.725 ± 0.001 K follows a very precisely a blackbody spectrum (Figure 2.2). COBE's results were soon confirmed by a number of balloon-borne experiments. COBE was sensitive only to broad fluctuations of large size where the Sachs - Wolfe effect is dominant, so the next generation satellite was needed to replace it. After COBE, the goal of CMB experiments has been to increase the angular resolution of the maps to study the small scale features in the angular power spectrum.

2.4.2 WMAP

The Wilkinson Microwave Anisotropy Probe (WMAP) [27] is a NASA Explorer mission that was launched in 2001 and it represents the second generation of CMB experiments: it was 45 times more sensitive, 33 times better angular resolution than COBE. A scheme of the WMAP spacecraft is shown in Figure 2.4. It had an angular resolution of at least 0.3° , a sensitivity of $20 \mu\text{K}$ per 0.3° square pixel, with systematic artifacts limited to $5 \mu\text{K}$ per pixel. WMAP mapped the CMB temperature over the full sky from the second Lagrangian point. It carried on board a pair of back-to-back telescopes roughly 140°

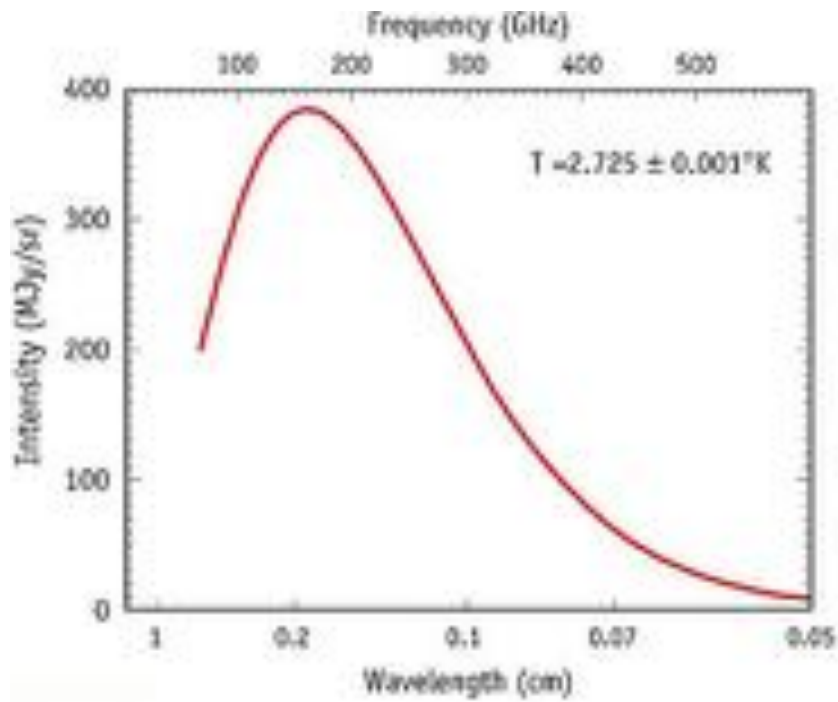


Figure 2.2: Spectrum of the cosmic background as measured by COBE. It confirmed its blackbody distribution.

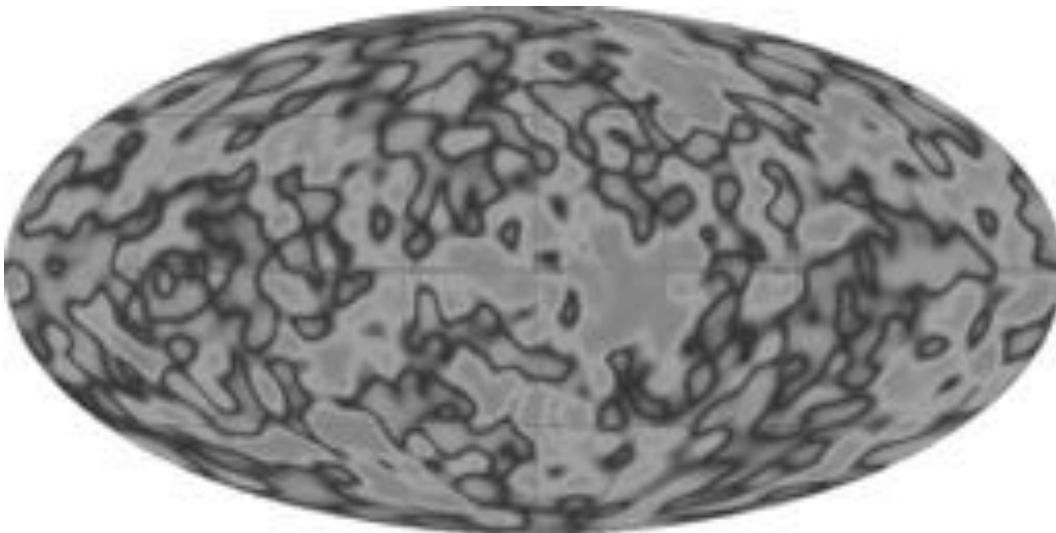


Figure 2.3: COBE DMR four-year data map. The typical angular scale of fluctuations is around 10° and the typical amplitude is around $30 \mu\text{K}$

apart, so it observed the sky in two directions and consequently made the difference between the signal and the sky signal. The signal was received by the polarization-sensitive differential radiometers in 5 different frequency bands from 23 GHz to 94 GHz, afterward amplified with HEMT low-noise amplifiers. The output of each assembly was proportional to the temperature difference

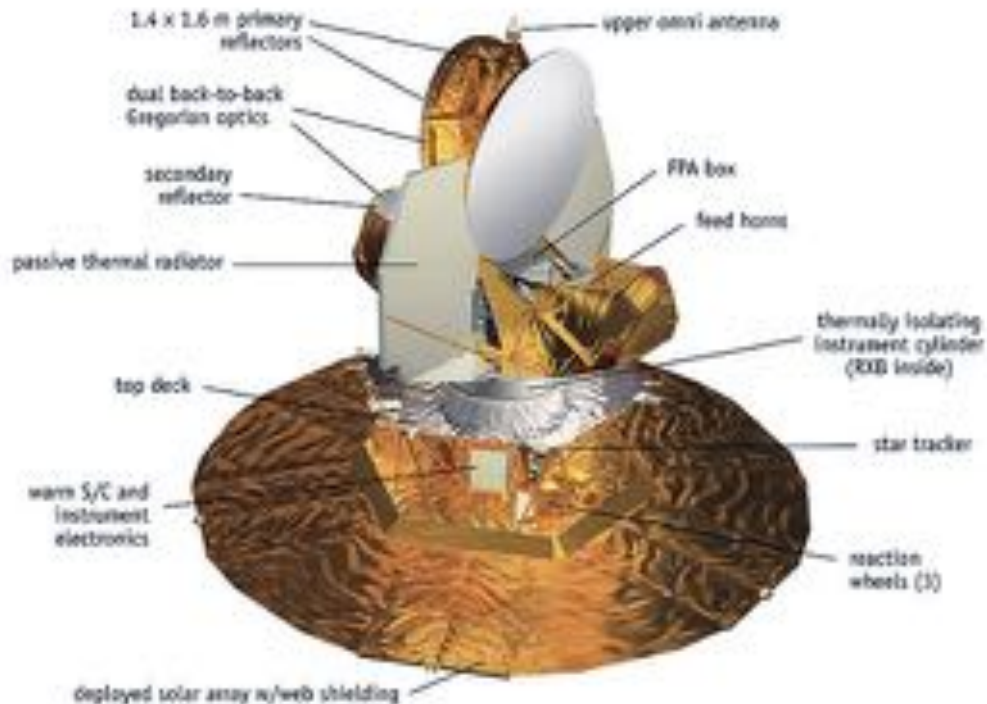


Figure 2.4: WMAP spacecraft scheme.

between the two lines of sight on the sky. To improve sensitivity and stability the system, it had a cold section where the first stages of microwave signal amplification occurs, then a warm section where the remaining amplification occurs before being converted to an electrical signal (as shown in Figure 2.5). The cold portion resides in the Focal Plane Assembly (FPA) box and is passively-cooled by large radiators on either side of the primary telescope mirrors. The warm portion resides below the FPA in the Receiver Box (RXB), which is located inside the thermally isolating cylinder that separates the warm spacecraft hub from the cold FPA and optics.

WMAP has been very successful, it produced the first fine-resolution (within 0.2 degree) full-sky map of the microwave sky (see Figure 2.6), but

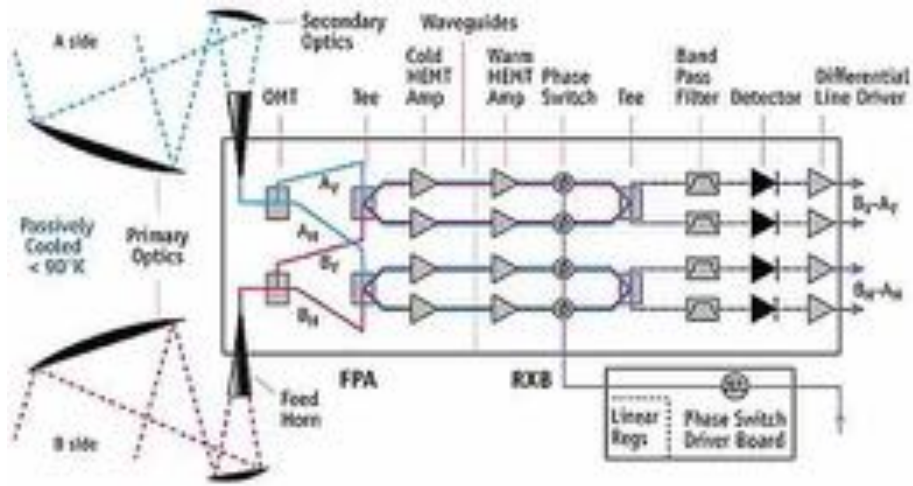


Figure 2.5: WMAP: scheme of the focal plane assembly and receiver box

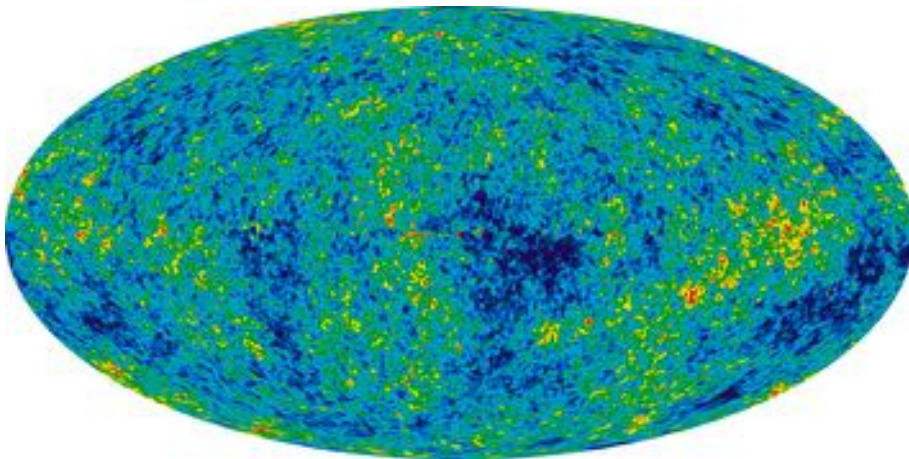


Figure 2.6: WMAP seven-year data map at 60 GHz.

also put constraints to many cosmological parameters:

- it determined the age of the universe to be 13.73 billion years old to within 1% (0.12 billion years);
- it has reported the first direct detection of pre-stellar helium, providing an important test of the big bang prediction;
- it strongly constrained dark energy and geometry of the universe;
- it placed new constraints on the number of neutrino-like species in the early universe;
- it has detected, with very high significance, the Sunyaev-Zeldovich effect;
- it has produced a visual demonstration of the polarization pattern around hot and cold spots.

The *Planck* mission represents the third generation CMB space experiment, an European successor to WMAP with 3 times better angular resolution, 10 times better sensitivity and nine wavelength coverage.

Chapter 3

The Planck mission

3.1 Introduction

The main objective of the Planck mission is to measure the fluctuations of the CMB with an accuracy set by fundamental astrophysical limits. To do this, Planck is imaging the the whole sky with an unprecedented combination of sensitivity ($\Delta T/T \sim 2 \cdot 10^{-6}$), angular resolution (to 5'), and frequency coverage (30–857 GHz) [28]. Planck will measure the angular power spectrum of the CMB fluctuations to high accuracy and will allow the determination of fundamental cosmological parameters such as the cold dark matter and baryon densities with an uncertainty of the order of one percent or better. In addition, the Planck sky surveys will produce a wealth of information on the properties of extragalactic sources and on the dust and gas in our own galaxy. One specific notable result will be the measurement of the Sunyaev-Zeldovich effect in many thousands of galaxy clusters: measurements of this effect can be used to study the properties of the hot cluster gas and the evolution of clusters, and to provide a direct measurement of the Hubble constant.

Planck was successfully launched on 14 May 2009 from Kourou, French Guyana, and since 13 August 2009 has been observing the sky. On 26 November 2010, Planck successfully ended its 15 months nominal mission, and has started its extended mission. Planck has started its fourth all sky survey on 14 February 2011, after successfully concluding its third survey. Planck is now scheduled to continuously acquire high-quality science data until the beginning of 2012. The mission will end at the beginning of 2012 for High Frequency Instrument, while the Low Frequency Instrument will acquire data for another year until its cryogenic requirements are satisfied.

3.2 The Planck satellite

A very important aspect for Planck, and in general for many experiments dedicated to the astronomical observations, is the observing strategy of the sky. Planck follows a Lissajous orbit around the L2 point, as shown in Figure (3.1) located along the Sun-Earth direction, the opposite side of the Sun, $1.5 \cdot 10^6$ km from the Earth (1/100 of the Sun-Earth distance) [29]. The direction of the satellite is updated to follow the motion of revolution around the Sun and keep to almost along the Sun-Earth direction, about 1 degree per day, or more specifically, $2'$ every 48 minutes. The optical axis of the Planck telescope is pointing to 85° from the axis of rotation of the satellite. Planck spin at about 1 rpm on this axis and the spin axis is repointed about hourly with a *cycloidal* scan strategy, in which the spin axis follows a circular path around the anti-Sun direction with a period of six months.

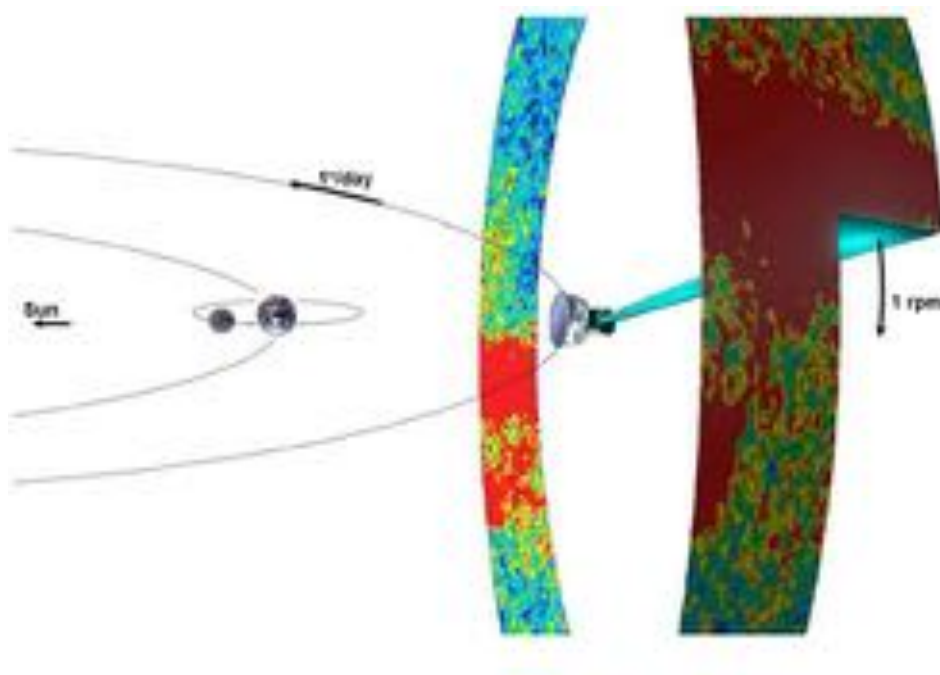


Figure 3.1: Planck is located on a Lissajous orbit around the second Lagrangian point of the Earth-Sun system. The satellite spins at 1 rpm around an axis which is pointed within $\sim 7^\circ$ of the Sun - Earth line. As it spins, the detector lines-of-sight sweep large circles around the sky.

The circles described by each detector are crossed many times in different positions in the sky so that observations taken at these intersections can be compared at the same point in the sky but in different periods and improve

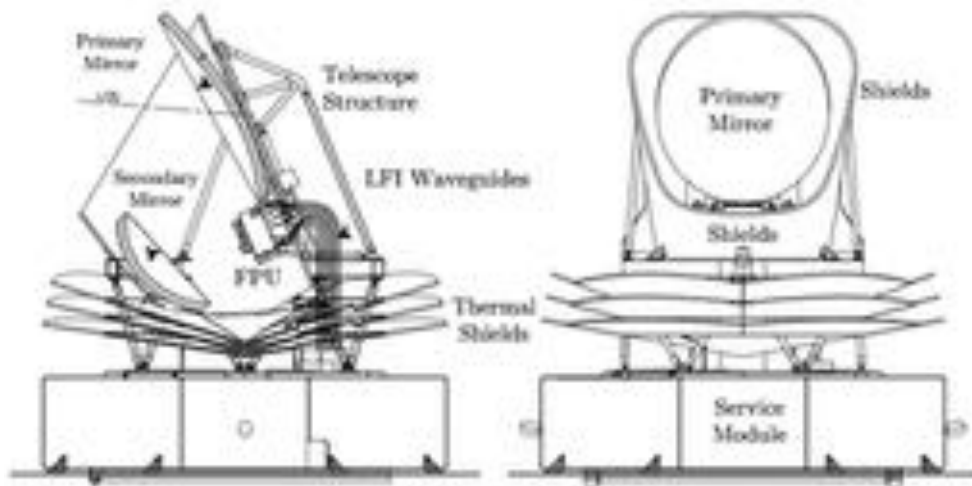


Figure 3.2: Side section (on the left) and front (on the right) view of the entire Planck Satellite

data statistics. Reordering the observations taken circle to circle the sky map is built for each detector. These maps at nine frequencies are analyzed together to obtain the map of anisotropies and those of all other astrophysical components.

The Planck telescope and instruments are surrounded by a large baffle which has the function to radiate heat and to shield stray light. The specular conical shields (called *Thermal shields* in Figure 3.2 and *V-grooves* in Figure 3.3) thermally decouple the Service Module (which contains all warm elements of the satellite) from the cold Payload Module. The satellite solar array is always exposed to the Sun and shields the payload from solar radiation.

Planck carries two scientific instruments: the High Frequency Instrument (HFI), based on bolometer technology and the Low Frequency Instrument (LFI), based on radiometer technology.

3.2.1 Planck cryogenic system

The unprecedented performance of the Planck instruments in space is enabled by their low operating temperatures, 20 K for LFI and 0.1 K for HFI, achieved through a combination of passive radiative cooling and three active coolers. This architecture is different from the previous CMB space missions. COBE used a liquid helium cryostat to enable cooling of the bolometers on its FIRAS instrument to 1.5 K. WMAP relied on passive radiative cooling alone which, while simpler, resulted in a higher operating temperature for its amplifiers and

a higher noise temperature.

Planck system represents complete novelty in the satellite CMB missions. The scheme can be seen in Figure 3.3 and it consists of a chain of cryo-coolers:

1. a hydrogen sorption cooler is the 20 K cooler system that provides the cooling stage for LFI and precooling stage for HFI;
2. a Joule-Thomson refrigerator driven by mechanical compressors, precooled to 18 K by the sorption cooler, which provides 4 K to HFI and 4 K to the reference load;
3. ^3He - ^4He dilution refrigerator which provides the final temperature of 0.1 K to HFI.

Hydrogen sorption cooler

The requirement for systematic effects minimization is the most important driver for the Planck architecture, which is particularly true for the thermal design. Cooling of the LFI front-end to 20 K is achieved with two hydrogen sorption coolers (one is considered a spare unit, but they are both used to increase the lifetime of the cryo-system). The hydrogen sorption cooler are the first continuous cycle sorption coolers to be used for a space mission. Since the spacecraft's warm end is by design located away (thermally and spatially) from the payload, this allows for excellent flexibility in integration of the cooler to the cold payload (instrument, detectors and telescope mirrors) and the warm spacecraft. The sorption compressor absorbs gas at low pressure and releases (desorbs) gas at high pressure after being heated. It is therefore a thermal compressor which is very convenient since it is a vibration free system with no moving parts.

The numerical thermal model

Prior to the launch, a numerical thermal model was developed describing the dynamic response of the LFI focal plane in order to verify the ability of the LFI instrument to reach the stringent limits of its scientific performance: $\delta T/T \sim 10^{-6}$ per pixel. Various on ground thermal tests were performed to validate the numerical model at Thales Laboratories in Milan in Italy [30] [31], at the Centre Spatial de Liege in Belgium and in-flight during the Calibration and Performance Verification (CPV) phase [32]. The numerical

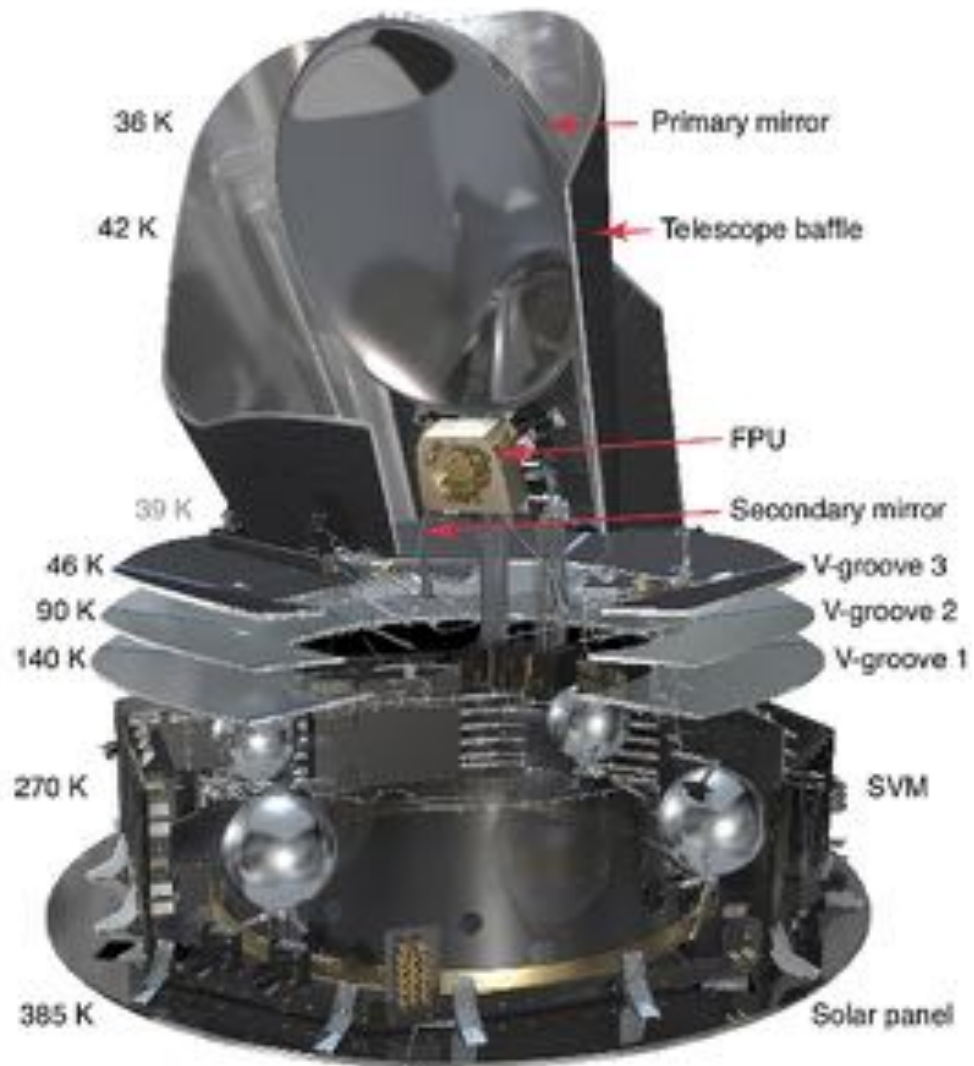


Figure 3.3: Cutaway view of Planck showing the temperature of key components. The solar panel at the bottom always faces the Sun and the Earth, and is the only part of the flight system illuminated by the Sun, the Earth, and the Moon. Temperature decreases steadily towards the telescope end, due to low-conductivity mechanical connections and aggressive use of radiative cooling. The focal plane detectors are actively cooled to 20 K and 0.1 K.

thermal model besides characterizing the steady state of each part of the instrument, quantifies the dynamical thermal function between the focal plane cold end and a set of points on the focal plane itself at three frequencies. The focal plane thermal analysis was performed by forcing thermal fluctuations at the sorption cooler cold end in cryogenic conditions, measuring the induced fluctuations on the thermometers placed on the focal plane and then comparing the results with the estimates of the thermal model.

3.2.2 High Frequency Instrument

The High Frequency Instrument provides measurements in six frequency bands: 100, 143, 217, 353, 545 and 857 GHz and it has unprecedented sensitivities down to $2.2 \mu\text{K}$ as shown in Table 3.1 [29]. These frequencies were chosen carefully to observe astrophysical foreground and for the detection of Sunyaev-Zeldovich effect. HFI consists in 52 bolometric detectors placed in the focal plane of the telescope.

Table 3.1: *High Frequency Instrument characteristics*

Instrument characteristic	100	143	217	353	545	857
Center Frequency	100	143	217	353	545	857
Angular resolution	9.5	7.1	5.0	5.0	5.0	5.0
$\Delta T/T$ Intensity [$10^{-6} \mu\text{K}/\text{K}$]	2.5	2.2	4.8	14.7	147	6700
$\Delta T/T$ Polarisation (Q and U) [$10^{-6} \mu\text{K}/\text{K}$]	4.0	4.2	9.8	29.8	n/a	n/a

To achieve these characteristics, the bolometers are operated at a temperature of 0.1 K, obtained by a complex cryogenic system.

3.2.3 Low Frequency Instrument

The Low Frequency Instrument is operative in three frequency bands 30, 44 and 70 GHz [33]. These frequencies were chose carefully: 70 GHz channel is in a frequency window remarkably clear from foreground emission, making it particularly advantageous for observing both CMB temperature and polarisation. The two lower frequency channels at 30 GHz and 44 GHz is accurately monitoring the Galactic and extra-Galactic foreground emissions.

The LFI Radiometer Chain Assemblies (RCA) are divided into two parts (see Figure 3.4). The front-end (*Front End Unit, FEU*) mounted on the focal plane which contains a first stage of amplification with ~ 30 dB), is cooled to about 20 K, and connected by a series of waveguides to the second part, called

back-end at 300 K (*Back End Unit, BEU*) in the Planck Service module, where the signal is further amplified and detected by a complex acquisition system.

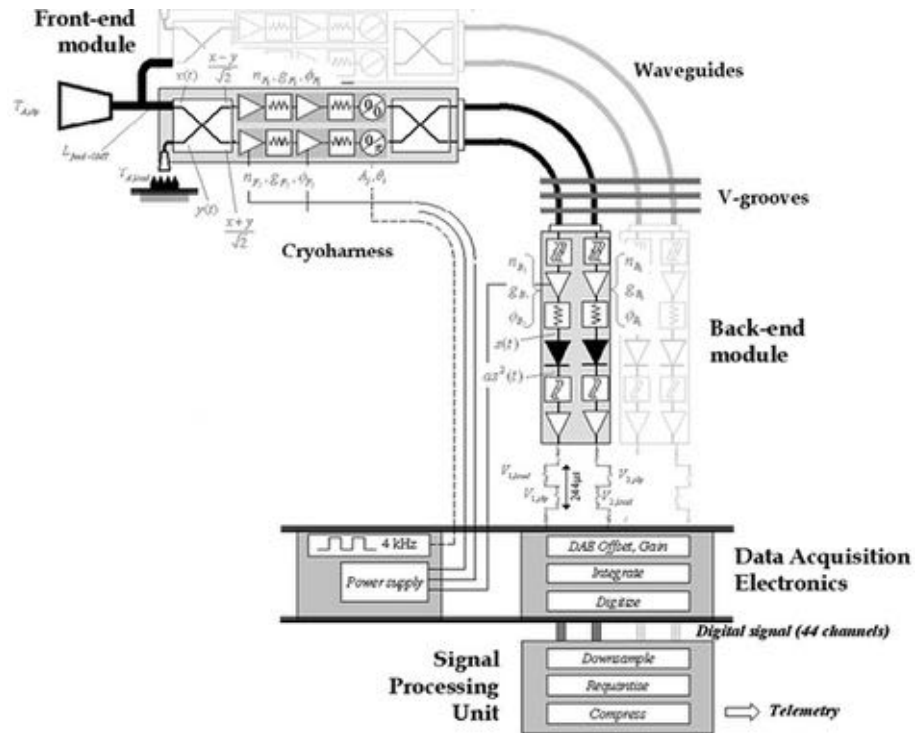


Figure 3.4: LFI receiver scheme, shown in the layout of a radiometer chain assembly (RCA).

The main components of LFI are:

- 11 feed horns working at three different frequencies (two at 30 GHz, three at 44 GHz and six at 70 GHz (see Figure 3.5),
- 11 Ortho Modal Transducers (OMT), connected directly after each feed horn. Each OMT splits the sky input signal in two orthogonal polarizations and sends each of them to the corresponding Radiometer Chain Assembly. This allows to study not only the temperature anisotropy of the CMB, but also the polarization anisotropy,
- 22 Radiometer Chain Assemblies, two for each antenna, labelled as Main and Side arms. Each RCA receives two input signals, the sky from the OMT and the reference load,
- Each radiometer has two hybrids,
- Phase switches - Each radiometer contains two phase switches,

- Amplifiers - 1 for each radiometer in the FEU and 1 in the BEU,
- 44 Detectors.

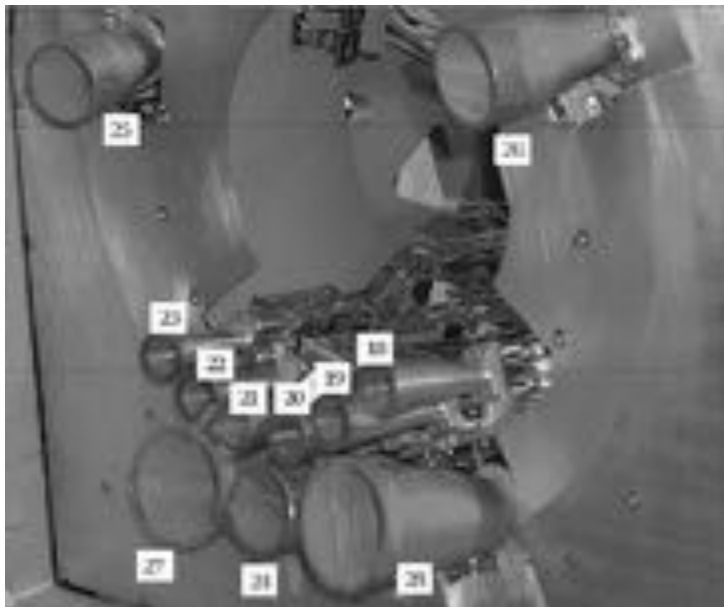


Figure 3.5: Position of the 11 feedhorns at the LFI focal plane. From 18 to 23 are 70 GHz receivers, from 24 to 26 are 44 GHz receivers and 27 and 28 are 30 GHz receivers.

Table 3.2: *Low Frequency Instrument characteristics*

Instrument characteristic	Center Frequency [GHz]		
	30	44	70
Number of feed-horns	2	3	6
Angular resolution [arcminutes FWHM]	33	24	14
Sensitivity [mK Hz ^{-1/2}]	0.17	0.20	0.27
$\Delta T/T$ Intensity [$10^{-6}\mu\text{K}/\text{K}$]	2.0	2.7	4.7
$\Delta T/T$ Polarisation (Q and U) [$10^{-6}\mu\text{K}/\text{K}$]	2.8	3.9	6.7

Pseudo-correlation model

LFI uses a differential pseudo-correlation, in which the signals from the sky are compared with a the signal from a black body called *reference load* at a temperature of ~ 4 K. This reference load has the characteristics of an emissive black body, and the differential technique allows the suppression of the impact of fluctuations due to the electronics chain. A similar technique was also used

in WMAP, where, however, the sky signal was not compared with reference load, but it subtracted the temperature of the sky in two different directions.

The differential pseudo-correlation scheme is the following (Figure 3.6):

1. the sky and reference load signal are combined by the first hybrid,
2. these signals are amplified by the Low Noise Amplifiers (LNA) with HEMT (High Electron Mobility Transistor) technology,
3. their phases changed alternatively by 180° by the phase shifts operating at 4 kHz,
4. signals are separated again by a second hybrid.

The result of this technique is that each RCA produces alternatively two output signals, the sky and reference load, with a frequency of 4 kHz. Both signals entered the same electronics chain and are delayed by $1/4 \text{ kHz} = 0.25 \text{ ms}$, a negligible time for the Planck observation strategy.

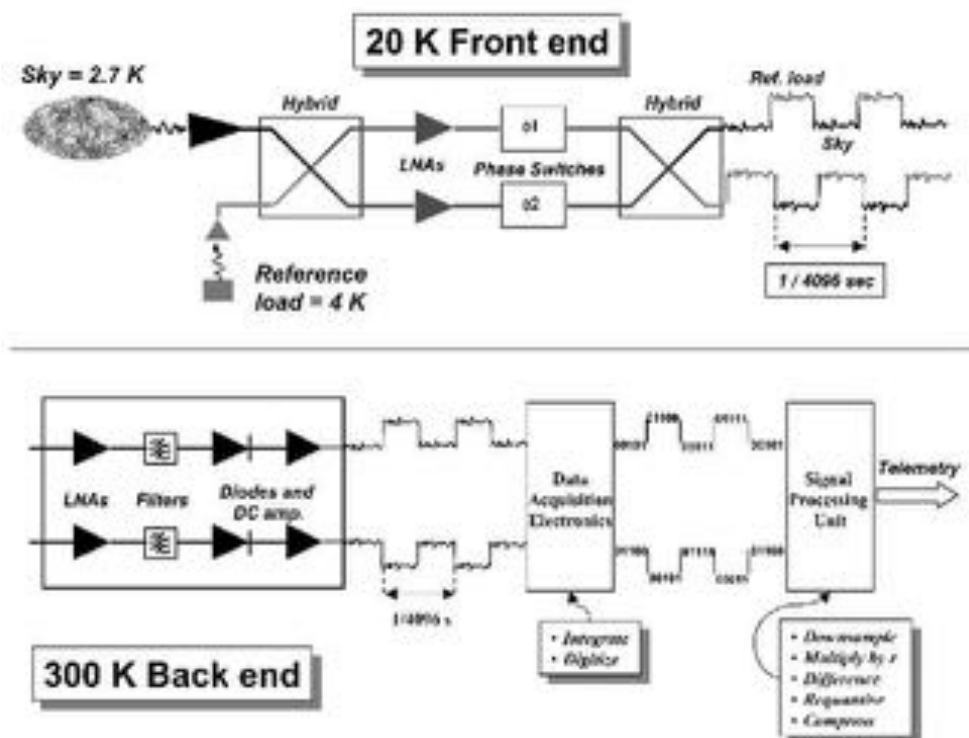


Figure 3.6: Scheme of the pseudo correlation model for LFI

If assumed a perfectly balanced radiometer behaviour, according to the scheme described above the differential output power for each diode can be

written as:

$$p_{out} = aG_{tot}k\beta[T_{sky} + T_{noise} - r(T_{ref} + T_{noise})] \quad (3.1)$$

where the r is the *gain factor* which minimizes the output effects:

$$r = \frac{T_{sky} + T_{noise}}{T_{ref} + T_{noise}} \quad (3.2)$$

and where G_{tot} is the total gain, k is the Boltzmann constant, β the receiver bandwidth, and a is the diode constant. T_{sky} and T_{ref} are the average sky and reference load antenna temperatures at the inputs of the first hybrid and T_{noise} is the receiver noise temperature. The gain factor is calculated each pointing period from the average uncalibrated total power data using the relationship:

$$r = \frac{\langle V_{sky} \rangle}{\langle V_{ref} \rangle} \quad (3.3)$$

The sky and the reference load power can then be measured and their difference calculated. Since the reference signal has been affected by the same gain variations in the two amplifier chains as the sky signal, the sky power can be recovered to high precision.

3.2.4 Systematic effects

The control of the thermal systematic effects represents a crucial point in the performance of the LFI instrument within the Planck mission. The LFI instrument was designed to minimise instabilities and systematic effects as thermal and electrical spurious fluctuations. Still, there are deviations from ideality in LFI that can be identified as main cause of systematic effects [34]:

1. Low frequency noise ($1/f$) intrinsic to the radiometers, discussed in Chapter 1. This noise is greatly reduced thanks to the pseudo-correlation model of the radiometers scheme and the destriping map-making code explained later in the next chapter.
2. 1 Hz frequency spikes due to a subtle disturbance from the housekeeping data acquisition performed by the Data Acquisition Electronics (DAE) unit. These artifacts are nearly identical in sky and reference samples, and are almost completely removed by the LFI pseudo-correlation scheme. The rest of the 1 Hz spikes are removed during TOI processing in Level 1.

3. Thermal fluctuations of the reference loads which have temperature of about 4 K coupled with the Stirling cooler (4 K). These instabilities may cause significant systematic effects since they are directly transferred to the measured signals. There is a *Proportional-Integral-Derivative* (PID) stabilisation applied to the HFI 4 K stage which significantly reduces thermal fluctuations which are dominated by the 20 K pre-cooling interface. The location of the PID on the 4 K stage leads to efficient damping for the 70 GHz reference loads. The 30 and 44 GHz reference loads are located further away from the PID source, and for them a similar damping level is not guaranteed. Again, this effect is greatly eliminated by the destriping techniques.
4. Radiometer thermal fluctuations in the front-end cooled to 20 K, which is the optimal operative temperature of the amplifiers. Fluctuations in this stage propagate in the radiometric differential signal through a complex transfer function obtained in two instrument ground test campaigns (as explained in the previous chapter).
5. Thermal fluctuations in the back-end modules. One effect detected during the first survey was the daily temperature fluctuation in the back-end unit induced by the transponder, which was turned on only for downlinks for the first 258 days of the mission [28].

3.3 Data processing

Data are continuously acquired by both instruments, packetized and transferred to the spacecraft computer, which stores the data into a solid state memory [29]. Science data are sent to Earth during the daily contact of 3 hours at a rate of 1.5 Mbps via a transponder. Every day approximately 13.4 Gbit of data are being received from the Planck satellite. This requires a coordinated and sophisticated data processing based on four centers distributed geographically (see Figure 3.7):

- The Mission Operation Centre (MOC), located at the Operations Centre at ESA in Darmstadt, Germany. This center is responsible for all aspects of flight control, health and safety of the satellite. MOC communicates with the satellite via the 36 m antenna in New Norcia, Australia every day, for 3 hours. In these three hours, it downloads the *HouseKeeping (HK)*

and scientific data obtained in the last 24 hours and sends the required telecommands to maintain the mission.

- Planck Science Office (PSO), located in Madrid at the Center for Space Astronomy, is responsible for the coordination of science operations tool for planning of the Planck scanning strategy.
- HFI Data Processing Centre located at the Institute of Space Astrophysics in Orsay and the Institute of Astrophysics in Paris is responsible for the optimal functioning of the HFI instrument and processing of its data.
- LFI Data Processing Centre, located at the Astronomical Observatory in Trieste, Italy is responsible for the optimal functioning of the LFI instrument and processing of its data.



Figure 3.7: A sketch of the centres involved in the Planck ground segment and the main data exchanges between them

The LFI DPC is organized in various logical steps [35].

Level 1: Telemetry processing and interface with the MOC;

During the operation of the satellite, the Data Processing Centres retrieves the data every day from ESA's Mission Operating Centre in a raw form, performs automatic and manual actions by the technical team including quick-look data analysis to ensure the good performance of the instrument. The first task discriminates between scientific (SCI) and HouseKeeping (H/K) telemetry packets. SCI packets are grouped according to radiometer, detector and processing type applied. Housekeeping parameters are those that refer to measurements of the health of the instrument. The output of this level is the *Time Ordered Information (TOI)*. The TOI files are always one-hour long: scientific streams longer than one hour are simply splitted into a number of files. TOI related to scientific measurements are often referred to as Time-Ordered Data (TOD). Technical processing on the TOIs was done with the software LIFE (LFI Integrated perFormance Evaluator).

Level 2: Data reduction and calibration;

At this level a data reduction and calibration is performed. The first task at this level is the creation of the differenced data from the combined computation of sky and reference load signals. In order to do this, the gain modulation factor is calculated. Among the main operations performed, there is the creation of the calibrated frequency maps. The map-making software uses the pointing information, identifying a given pointing direction ordered in time. On this temperature timeline, a map-making algorithm is applied to produce a receiver maps. The instrument model allows control of the systematic effects, and the quality of the removal performed by map-making and calibration of the receiver map. Receiver maps cleaned from systematic effects at different levels of accuracy are stored into a calibrated map archive.

Level 3: The main task of the DPC Level 3 is the production of the maps for the different astrophysical and cosmological components present in the sky signal. From the reconstructed CMB component (generated by component separation algorithms or through a suitable linear combination and/or masking of the original calibrated frequency maps), the angular power spectrum of the CMB is computed for both temperature modes (TT) as well as polarization and cross

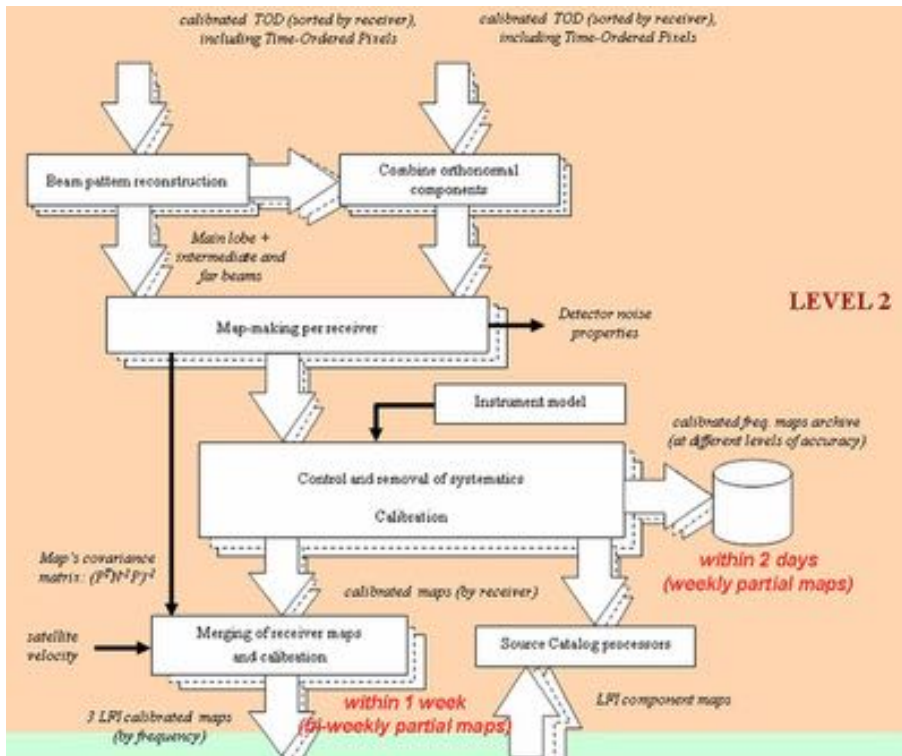


Figure 3.8: Level 2 map-making pipeline

temperature/polarisation modes. This separation and optimization requires HFI and LFI data to be analyzed jointly and this is being done at the Planck section at SISSA in Trieste.

Level 4: generation of final products (reception, archiving, preparation of public release material);

Level S: during the pre-launch phase, simulation of data acquired from the Planck mission.

This structure implies a large number of data processing codes and data products which are organized under the Planck's *Integrated Data and Information System* (abbreviated IDIS). The communication and connection between the different sites can be seen in Figure (3.7). The Planck DPCs are responsible for the delivery and archiving of the following scientific data products, which can be considered as the deliverables of the mission [36]:

- Calibrated time series data, for each receiver, after removal of systematic features and attitude reconstruction.

- Photometrically and astrometrically calibrated maps of the sky in the observed bands.
- Sky maps of the main astrophysical components.
- Catalogs of sources detected in the sky maps of the main astrophysical components.
- CMB Power Spectrum coefficients.

The Planck Collaboration announced the release of the first Planck data products and scientific results on January 11, 2011: 25 scientific papers are now available which describe the scientific performance of the Planck payload, and present results on a variety of astrophysical topics. In 2012 a release of a set of papers focused on Galactic and extragalactic science is expected; for the primary CMB cosmology results instead, the release date is set to January 2013.

Chapter 4

Assessment of thermal systematic effects on maps and power spectra

This thesis work concentrates on the thermal fluctuations in the back-end unit, front-end unit and 4 K reference loads of the LFI instrument. As we have seen in the previous chapter, the cryogenic thermal system consists of passive and active elements to reach the required working temperatures. The radiometric chain assembly begins from the cold front unit and ends in the back-end unit: controlling thermal fluctuations in these units is of fundamental importance for the systematic effects on the output signal. Temperature variations impact the sky and reference load signals at a similar level, so thanks to the pseudo correlation model, the residual spurious variations are reduced by more than one order of magnitude [36].

The method we use here in order to understand how thermal systematic effects impact on the LFI science, represents novelty in the assessment of systematic effects in a CMB experiment in general. This was possible thanks to the detailed knowledge of the instrument and the availability of a set of sensors located on various places on the instrument [31]. In particular, the numerical thermal model that allows us to translate the physical temperature behaviour at the level of the receiver components sensitive to the fluctuation [30].

Our method of studying thermal systematic effects consists in using actual flight housekeeping data coming from these sensors and projecting the effect onto maps and on the angular power spectra. The results were then compared to the scientific requirements for the LFI instrument.

The next table show the total error budgets allowed and expected for the LFI instrument [36].

Table 4.1: *LFI thermal systematic effect requirements.*

Source	Error from spin synchronous oscillations	Error from other periodic oscillations
Front end	$\pm 0.45 \mu\text{K}$	$\pm 0.90 \mu\text{K}$
Back end	$\pm 0.40 \mu\text{K}$	$\pm 0.40 \mu\text{K}$
4 K load	$\pm 1 \mu\text{K}$	$\pm 0.6 \mu\text{K}$
Total	$\pm 1.85 \mu\text{K}$	$\pm 1.90 \mu\text{K}$

We can separate the thermal fluctuations as [37]:

- low frequency range, $\tau_f > \tau_{spin}$, where τ_{spin} is the spinning period of the satellite, $\tau_{spin} = 60$ s,
- high frequency range, $\tau_f \leq \tau_{spin}$, which can be divided further in spin-synchronous frequencies (frequencies multiple of the spin period, $\tau_f = k\tau_{spin}$) e non spin-synchronous frequencies ($\tau_f \neq k\tau_{spin}$), k being an integer number.

After N observations of the same pixel, the residual signal oscillation is given by:

$$\langle \delta T_{sky}(t) \rangle_{t_N} = \frac{1}{N} \sum_{j=1}^N \delta T_{sky}(t_j) \quad (4.1)$$

where $t_j = t + (j - 1)\tau_{spin}$. If a sinusoidal oscillation is considered, $\delta T_{sky}(t) = A_f \cos(2\pi t/\tau_f)$, the equation 4.1 becomes:

$$\langle \delta T_{sky}(t) \rangle_N = \frac{A_f}{N} \sum_{j=1}^N \cos(2\pi t/\tau_f) = \quad (4.2)$$

$$= \frac{A_f}{N} \cos[\pi(2t + (N - 1)/\tau_{spin})] \frac{\sin(\pi N\tau_f)}{\sin(\pi\tau_f)} \quad (4.3)$$

Since the term $\cos[\pi(2t + (N - 1)/\tau_{spin})]$ is bounded by ± 1 , the peak-to-peak fluctuation in the data stream after averaging over N scan circles is given by

$$\langle \delta T_{sky}(t) \rangle_N = 2 \left| \frac{A_f}{N} \frac{\sin(\pi N\tau_f)}{\sin(\pi\tau_f)} \right| \quad (4.4)$$

From equation (4.4) it follows that the spin synchronous fluctuations (for which $\tau_f = \tau_{spin}/k$) are not damped by the measurement redundancy: $\lim_{x \rightarrow 1} (\sin(N\pi x)/\sin(\pi x)) = N$.

The LFI mechanical structure was build on purpose to inhibit the high frequency fluctuations. The low frequency instead, are greatly suppressed by the spinning of the satellite. The destriping technique (explained later in this chapter) plays a crucial role in the processing the effects of these fluctuations. Thus the fluctuations in spin-synchronous range frequency remain the major systematic thermal contribution and can be undistinguishable from the true sky signal.

4.1 Characteristics of thermal systematic effects

4.1.1 Front-end temperature fluctuations

The main cause of thermal fluctuations on the cold front-end unit comes from the sorption cooler, in particular from the cycling of the sorbent compressors [31]. In order to control this feature, a Temperature Stabilisation Assembly (TSA) was developed by the team responsible for the sorption cooler to control the low frequency fluctuations, which are the ones that are not efficiently damped by the instrument mechanical structure. The TSA is able to damp the temperature fluctuations which are of order of ~ 0.5 K to about 100 mK (peak-to-peak). Over time the sorption cooler is expected to degrade and the TSA to reduce its efficiency. Indeed there are two sorption cooler units on board Planck to increase the lifetime of the cryo-chain and on the *Operational Day* (OD) 457 the first sorption cooler unit was switched over with the second one. To verify the possible deterioration, we estimated the sorption cooler effect on the final maps in two periods, the first from OD 91 to 215 and the second from OD 275 to 389. Also the maps and power spectra were generated for the entire period from OD 91 to OD 389.

4.1.2 Back-end temperature fluctuations

Similar requirements (Table 4.1), were imposed to the stability of the back-end modules where further amplification takes place. During the first 258 days of the mission, the transponder which transmits and receives the data was turned on in the 3-hours daily contact, and then back off. After the 258th day of the mission it was left always on, since it was understood that the change in the

total power budget due to the transponder switching on and off, was causing daily thermal fluctuations in the whole service module and on the LFI BEMs. To study the effect on the signal of this operation, we considered two identical observed regions of the sky of same duration 115 days each: OD 91-215 and OD 275-389. We first analysed the behaviour of the BEU thermal sensors, and then, based on these results, it was analysed how the scientific data was affected before and after the turn on of the transponder by building the corresponding maps. Also the maps and power spectra were generated for the entire period from OD 91 to OD 389.

4.1.3 4 K reference load temperature fluctuations

As shown in the previous chapter, the fluctuations in the reference loads on 4 K are the key factor in the systematic effects [34], in particular for the 30 and 44 GHz channel since they are farther from the PID stabilisation source.

4.2 Time-ordered data generation

In order to have the control of the instrument thermal stability, there are thermometers (or temperature sensor) placed on different places on the FEU and BEU. In order to enhance the thermal systematic effects on the scientific data due to the different sources, this analysis aims at producing maps and power spectra of the housekeeping temperature sensors treating them as they were a scientific data i.e. using pointing and sampling rate of each scientific channel.

Scientific and housekeeping sensors have different sampling rates: science data are all acquired at a frequency of 8192 Hz but are then elaborated and compressed so that they are finally sampled at 18 Hz (30 GHz), 12 Hz (44 GHz) and 8 Hz (70 GHz) while HK sensors at 1 Hz. For each scientific channel, housekeeping sensors were artificially sampled to the corresponding frequency.

All the analyses were performed using pipelines in the Python software language. The LFI Data processing centre has a cluster of 115 available nodes with 2 processor cores per node.

We have considered the housekeeping data from different sensors:

- LM207332, corresponding to the reference sensor placed on the BEU,

- SM020540 which corresponds to the sorption cooler TSA temperature sensor,
- LM305322 and LM202322, corresponding to two reference sensors placed respectively on the right and left part of the focal plane,
- L1_A5 corresponding to sensor for the 4 K reference load near to the 30 and 44 GHz radiometer and PIDN corresponding to sensor for the 4 K reference load near to the 70 GHz.

The operations that are performed on the housekeeping data are the following:

1. Take the TOIs from the different temperature sensor corresponding to the considered thermal stage;
2. The low-noise filter is applied to remove the high-frequency noise of the sensors;
3. Thermal and radiometric transfer functions which are available on the LFI DPC database are applied;
4. Resample at the science data rate, calibrate and build differenced TOI;
5. Use these TOIs to build maps with the code Madam explained below (see section 4.3);
6. Calculate the power spectra with Anafast, explained below (see section 4.3) and compared them with a reference CMB power spectrum taken from the WMAP online archive. The average of the signal is subtracted so that only the fluctuations remain.

The thermal transfer functions come from the numerical thermal model developed and tested before the launch (as explained in Chapter 3). These functions give the propagation of physical temperature behaviour at the point of the component under analysis. The radiometric transfer functions f_{trans} instead, converts the physical temperature fluctuation into the antenna temperature fluctuation i.e. the corresponding fluctuations on the sky signal measurement [38]:

$$\delta T_{out} = f_{trans} \delta T_{phys} \quad (4.5)$$

where the f_{trans} can be estimated analytically from the differential power output given in equation 3.1. The analytical form of radiometric transfer functions can be derived by taking into account the various terms from: insertion losses of the radiometric system and of the 4K reference horn, the thermal stability of front end gain and noise temperature, and on the gain modulation factor, r .

4.3 Destriping and map generation

When the low frequency fluctuations are coupled with the Planck scanning strategy they produce artefacts in the final CMB maps. These artefacts express themselves as *stripes* which are clearly visible in the maps and they follow the circular trajectories that the telescope beam scans in the sky. The noise stripes clearly follow the pole-to-pole scanning circles. The stripes will increase the overall noise level and introduce correlations that affect the statistical analysis of the CMB pattern in the sky which is an important input data when the angular spectrum of the CMB is determined. The stripes will degrade the accuracy of these angular spectra.

The destriping method makes use of the fact that Planck's scanning is organized in successive closed nearly polar circles and each scan circle is observed 60 times before the spin axis is repointed [39]. During the nominal 14 months mission time there are around 10 000 scanning circles. In order to reduce the level of instrumental noise, the signal can be averaged over these 60 scan circles.

The effect of the instrumental noise, in particular the $1/f$ noise, on the average scan circle signal can be approximated by a uniform offset or *baseline*. When the baseline values are appropriately determined they can be subtracted from the original map and a new map is produced where the stripes have been removed. The key point here is how to determine the baseline values. The destriping technique uses the redundancy of the observing strategy, i.e. it considers all intersections (crossing points) between the scan circles, to obtain these magnitudes. Madam also allows the use of an optional noise prior, if the noise spectrum can be reliably estimated, which further improves the accuracy of the output map.

MADAM is the map-making code designed for the production of full-sky maps of the cosmic microwave background anisotropy [40]. This code

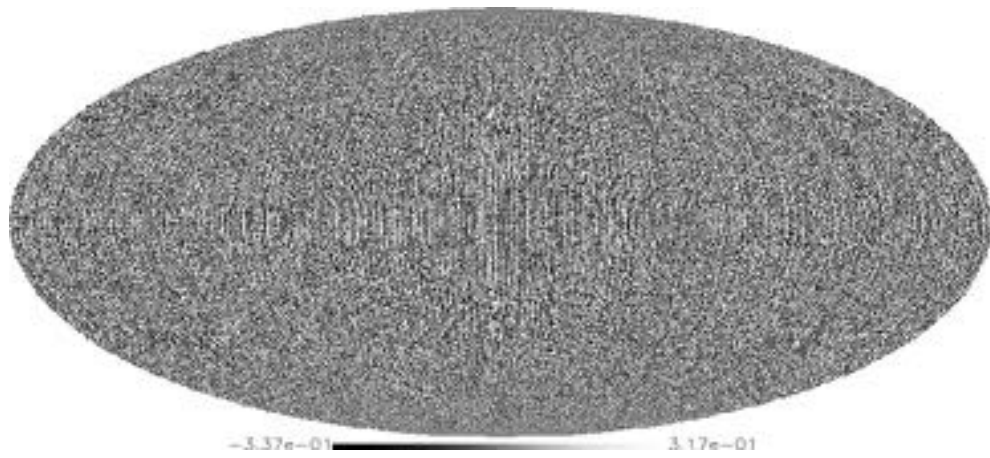


Figure 4.1: Pure noise (white and $1/f$ noise together) map before destripping: stripes are clearly present and follow the pole-to-pole scanning circles. The units are in mK.

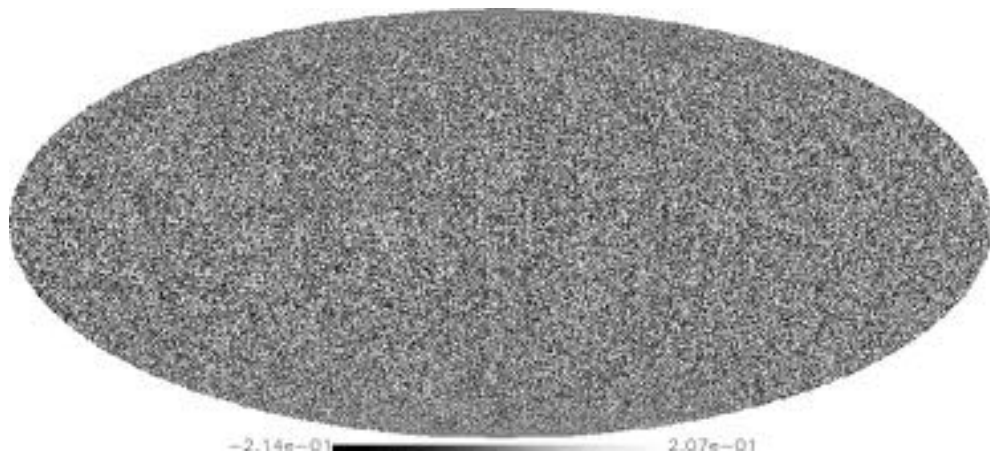


Figure 4.2: Noise map after destripping for the same case illustrated in Figure 4.1: stripes are no more visible

was developed for the Planck satellite, but is applicable to any total power CMB experiment. In our case, Madam was used to build maps of the different systematic effects. Madam requires as input 1) simulation file (which defines the input data set) and 2) parameter file (which contains the input parameters). The map-making pipeline takes as an input the calibrated time-ordered data stream and pointing information in the form of three angles (θ, ϕ, ψ) describing the orientation of the feed horns for each single sample considered. Angles ϕ and θ define a point on the celestial sphere, while ψ defines the orientation of the polarization sensitivity.

The outline of the map-making algorithm and its assumptions is that the time-ordered data, \mathbf{d} , which consist of N_d sky observations made with a given scanning strategy and at a given sampling rate. A map, \mathbf{m} , can be thought as a vector containing N_d temperature values, associated with sky pixels of dimension $\sim FWHM/3$. A map of the full sky contains $12N_d^2$ pixel. The maps are of the entire celestial sphere in an equal-area Mollweide projection. In the Mollweide projection the equator is represented as a straight horizontal line perpendicular to a central meridian one-half its length. The other parallels compress near the poles, while the other meridians are equally spaced at the equator.

The power spectra are generated with HEALPix which is a NASA's software programs for fast simulation and analysis of full-sky maps of CMB temperature and polarization anisotropy. The 30 GHz maps are produced at HEALPix with resolution parameter $N_{side} = 512$, while the 44 GHz and 70 GHz maps were produced at $N_{side} = 1024$.

Chapter 5

Results and discussion

5.1 Back-end temperature fluctuations

5.1.1 Analysis of the period from OD 91 to OD 389

The analysis of the overall thermal systematic effects was performed with the housekeeping time-ordered data from LM207332, corresponding to the reference sensor placed on the BEU. The resulting maps and power spectra are here displayed for each frequency band.

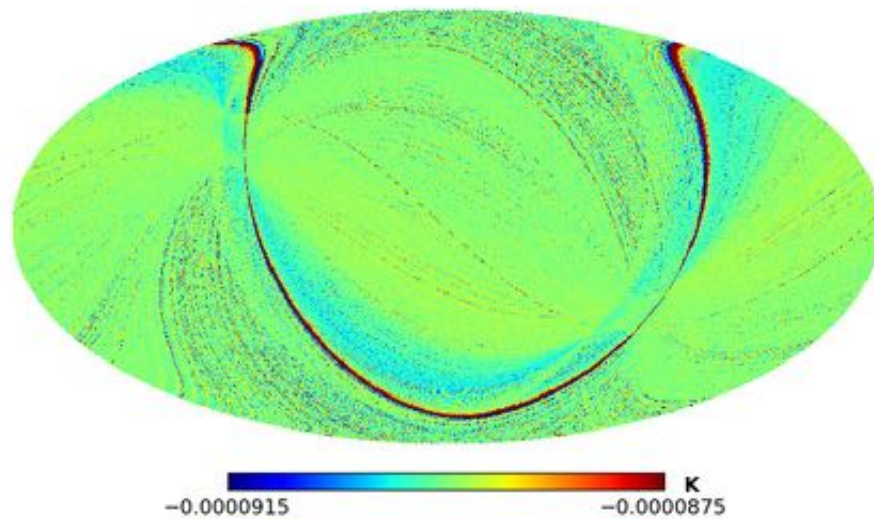


Figure 5.1: Map in intensity of the systematic effect from BEU fluctuations, 30 GHz channel, OD 91-389

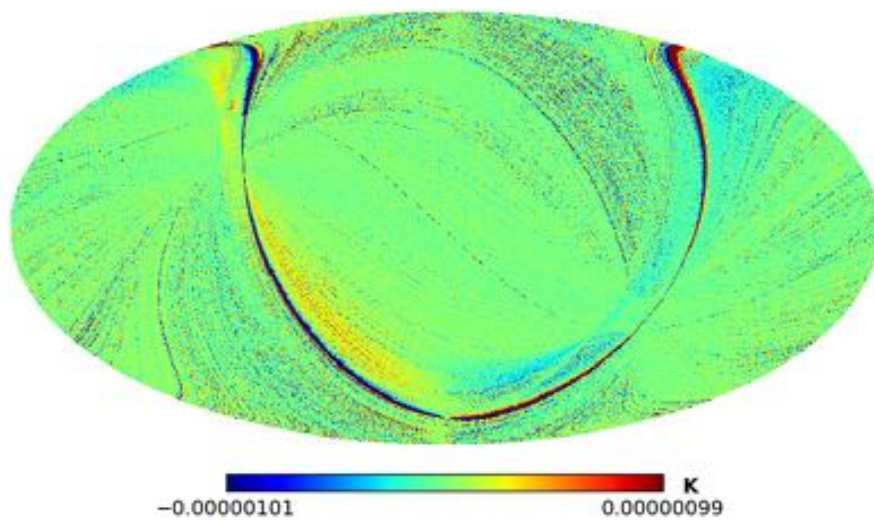


Figure 5.2: Map in polarisation Q of the systematic effect from BEU fluctuations, 30 GHz channel, OD 91-389

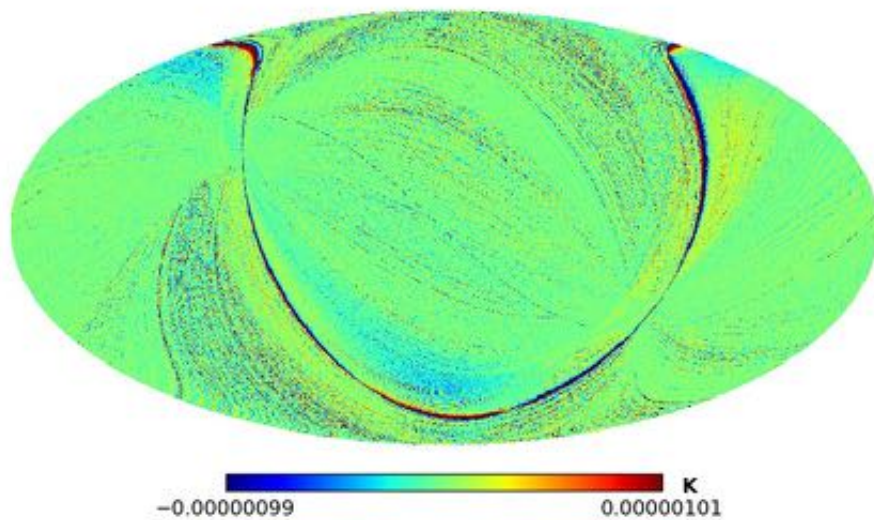


Figure 5.3: Map in polarisation U of the systematic effect from BEU fluctuations, 30 GHz channel, OD 91-389

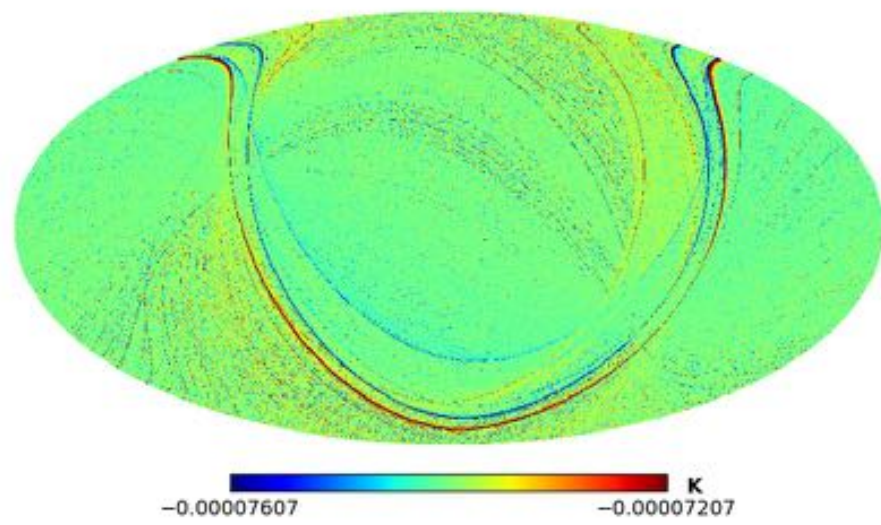


Figure 5.4: Map in intensity of the systematic effect from BEU fluctuations, 44 GHz channel, OD 91-389

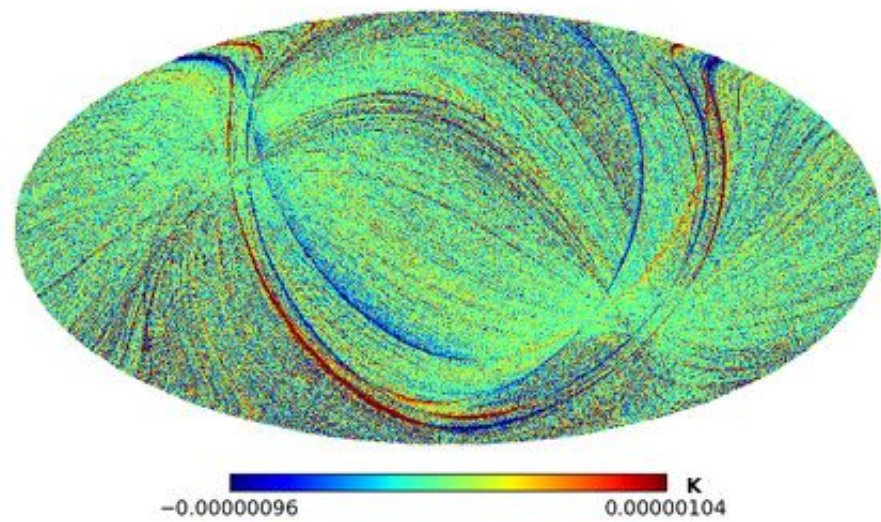


Figure 5.5: Map in polarisation Q of the systematic effect from BEU fluctuations, 44 GHz channel, OD 91-389

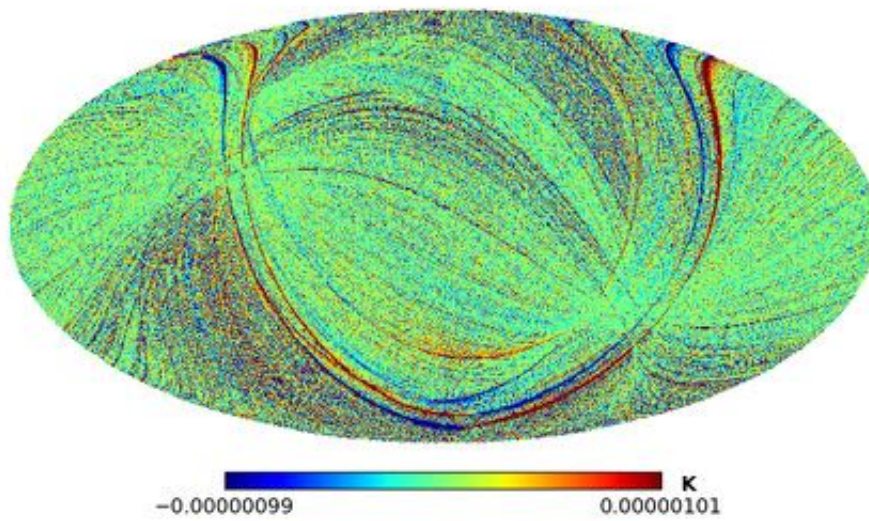


Figure 5.6: Map in polarisation U of the systematic effect from BEU fluctuations, 44 GHz channel, OD 91-389

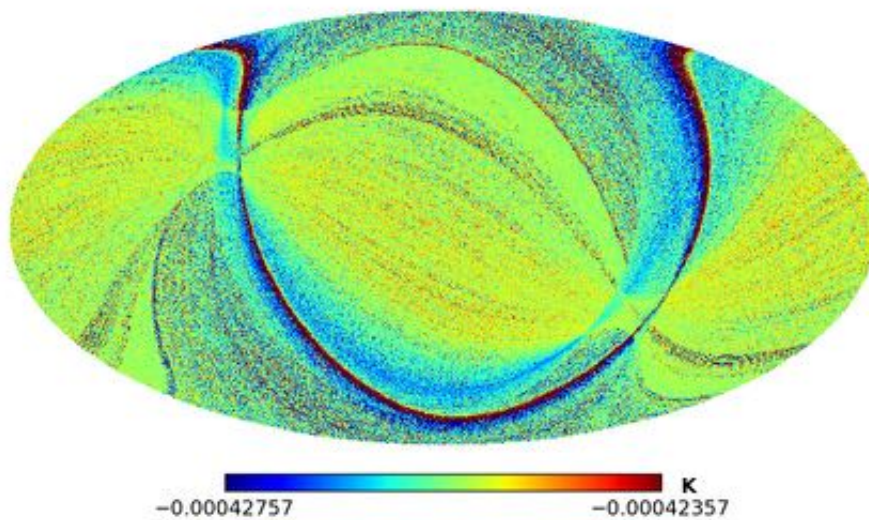


Figure 5.7: Map in intensity of the systematic effect from BEU fluctuations, 70 GHz channel, OD 91-389

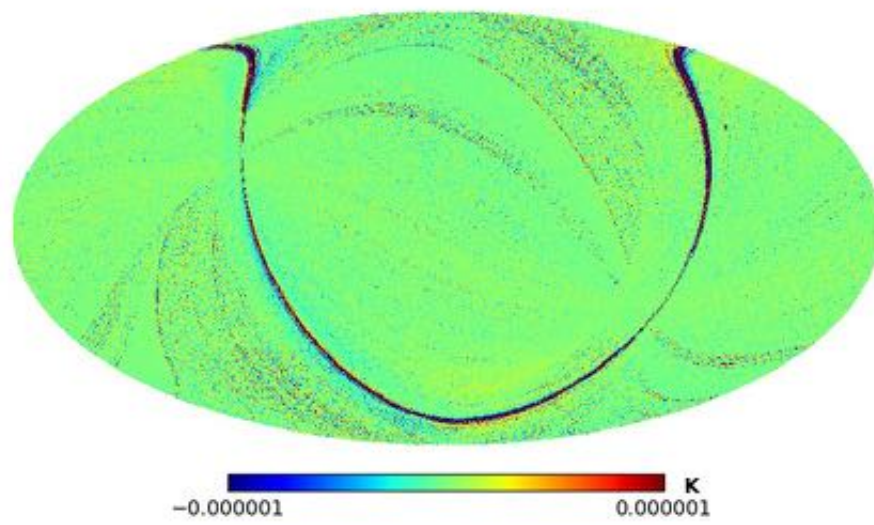


Figure 5.8: Map in polarisation Q of the systematic effect from BEU fluctuations, 70 GHz channel, OD 91-389

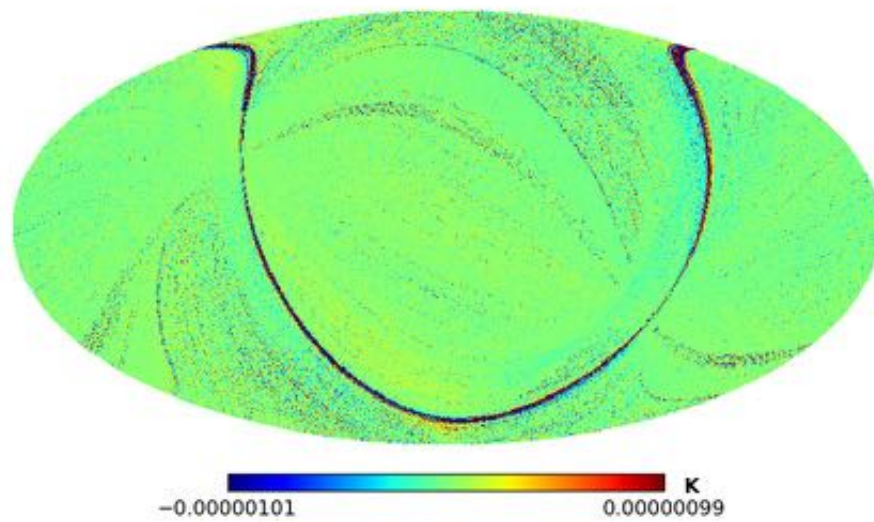


Figure 5.9: Map in polarisation U of the systematic effect from BEU fluctuations, 70 GHz channel, OD 91-389

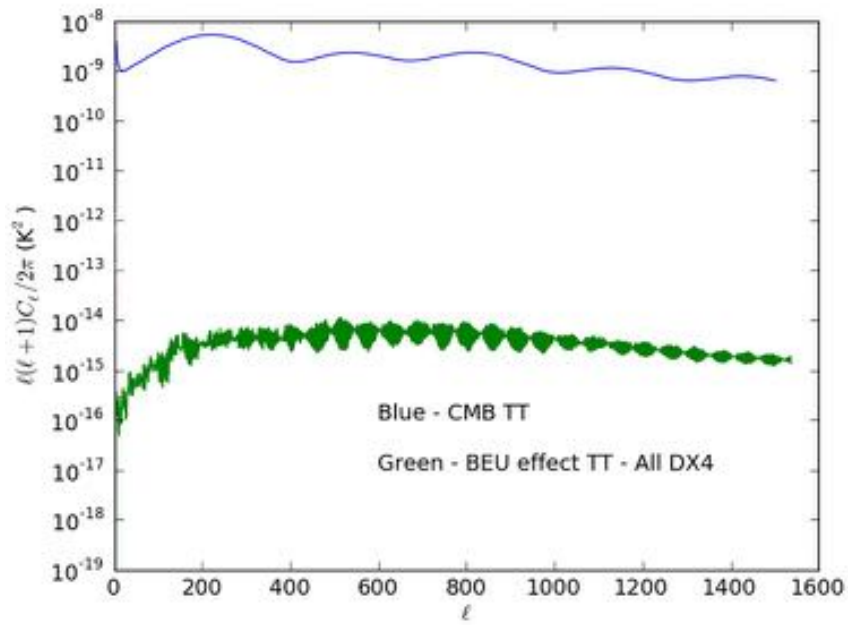


Figure 5.10: Power spectrum from the effect of the BEU temperature fluctuations (TT), 30 GHz channel, OD 91-389

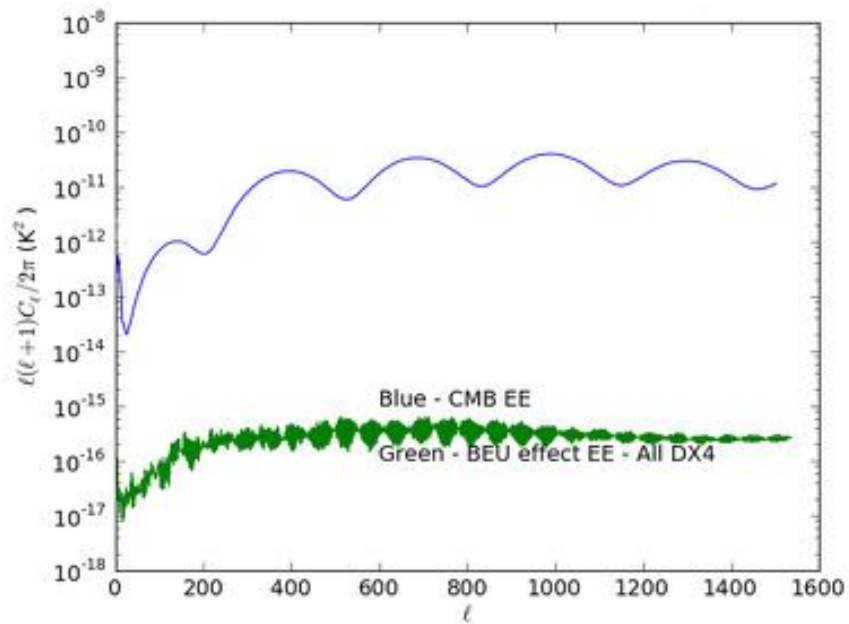


Figure 5.11: Power spectrum from the effect of the BEU temperature fluctuations (EE), 30 GHz channel, OD 91-389

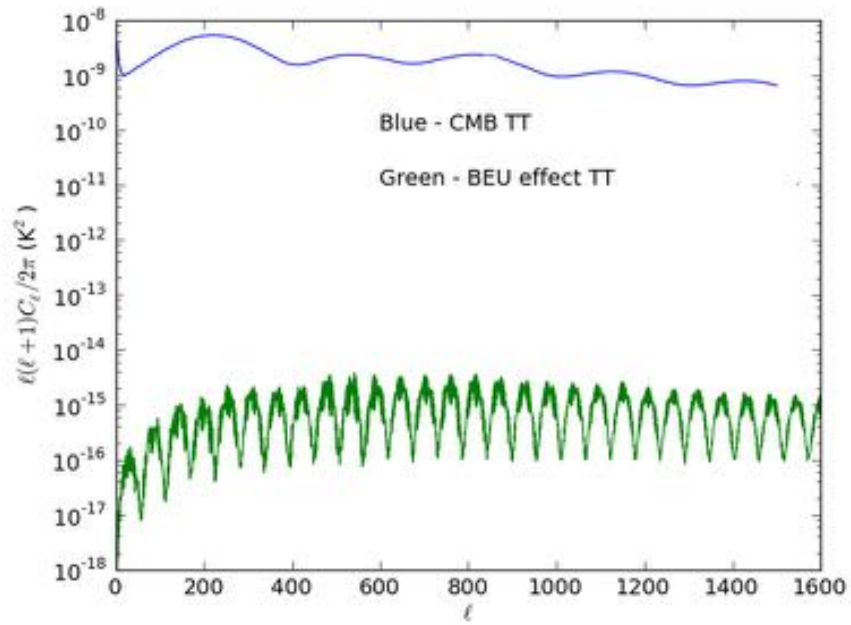


Figure 5.12: Power spectrum from the effect of the BEU temperature fluctuations (TT), 44 GHz channel, OD 91-389

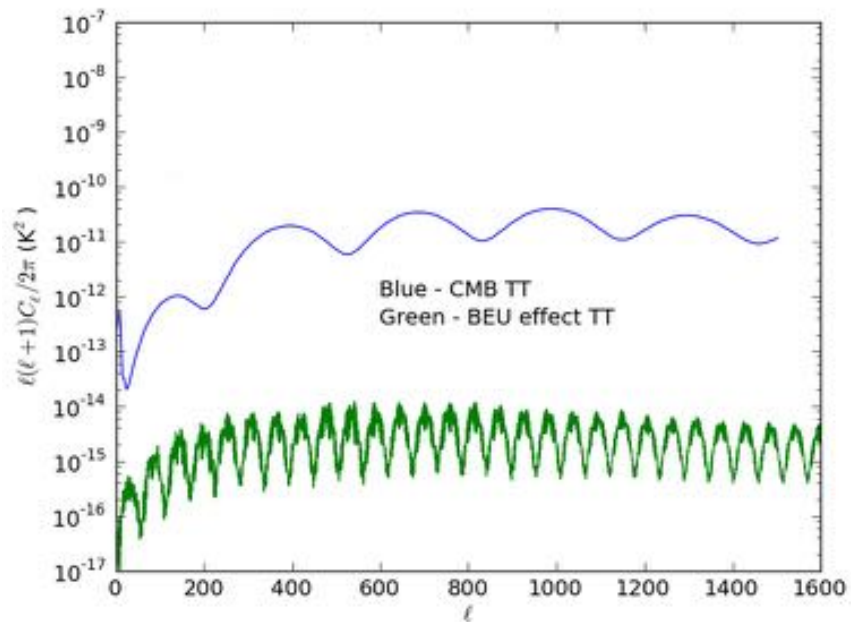


Figure 5.13: Power spectrum from the effect of the BEU temperature fluctuations (EE), 44 GHz channel, OD 91-389

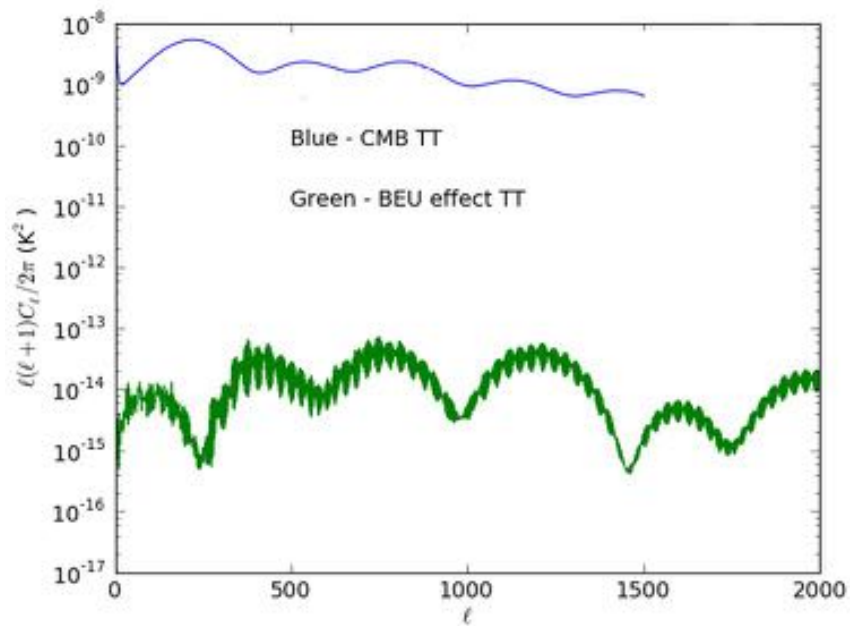


Figure 5.14: Power spectrum from the effect of the BEU temperature fluctuations (TT), 70 GHz channel, OD 91-389

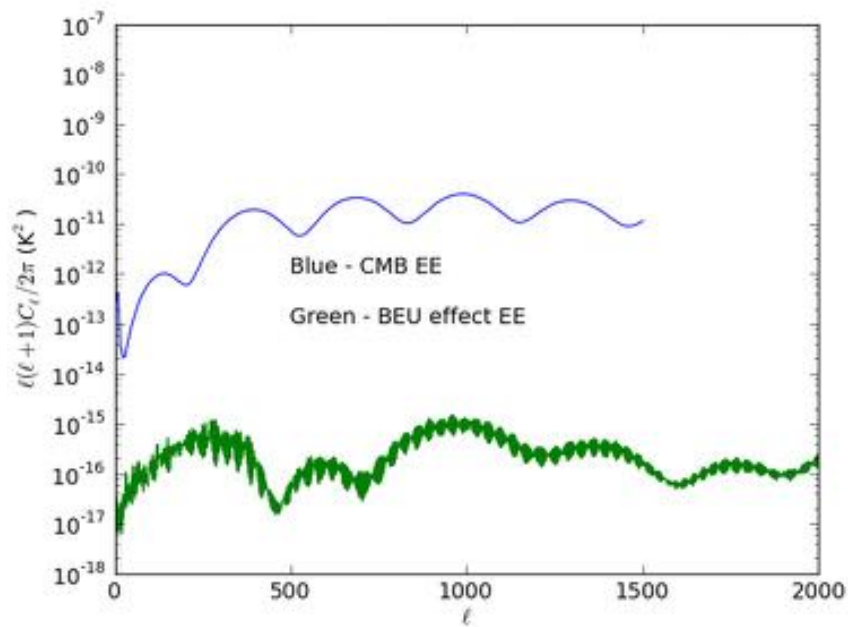


Figure 5.15: Power spectrum from the effect of the BEU temperature fluctuations (EE), 70 GHz channel, OD 91-389

5.1.2 Analysis in the periods OD 91-115 and OD 275-389

In order to enhance the possible effect from transponder switching on, we considered two identical observed regions of the sky of same duration 115 days each: OD 91-215 and OD 275-389. Again, the housekeeping time-ordered data from LM207332, corresponding to the reference sensor placed on the BEU was considered. The resulting maps and power spectra are here displayed for each frequency band.

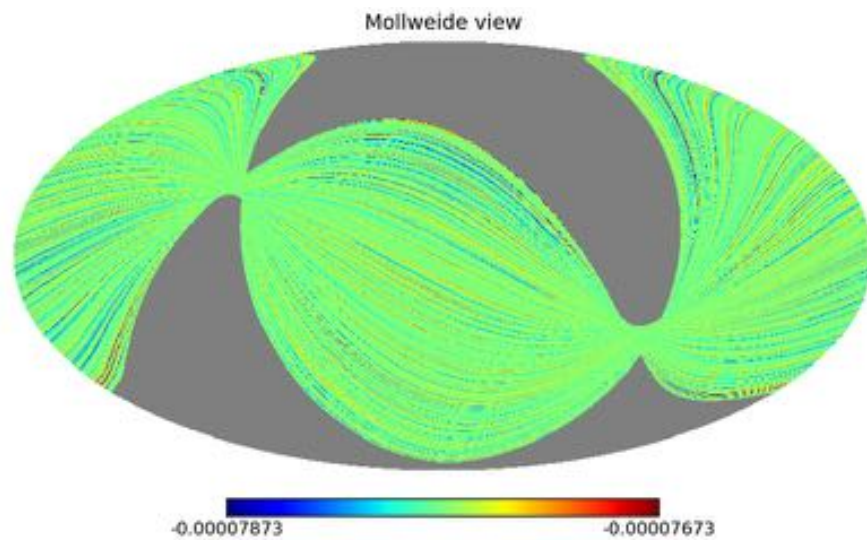


Figure 5.16: Map in intensity of the systematic effect from BEU fluctuations, 30 GHz channel, OD 91-215

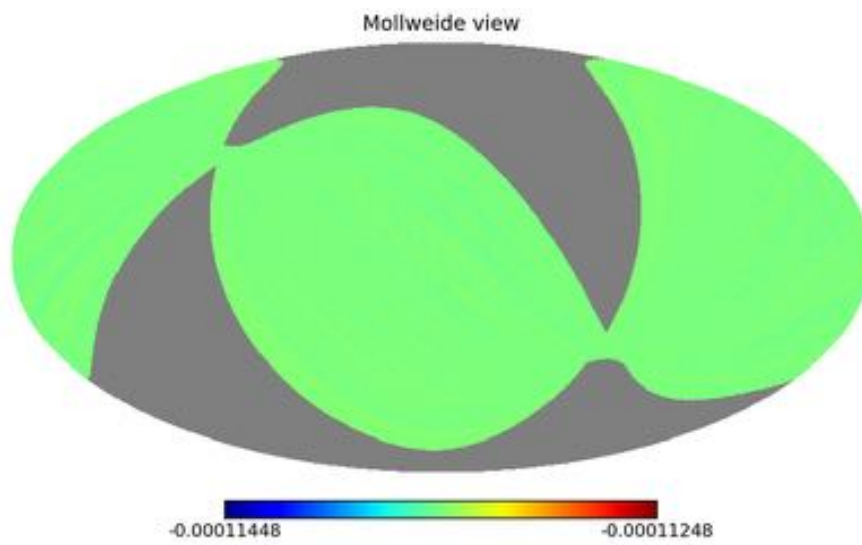


Figure 5.17: Map in intensity of the systematic effect from BEU fluctuations, 30 GHz channel, OD 275-389

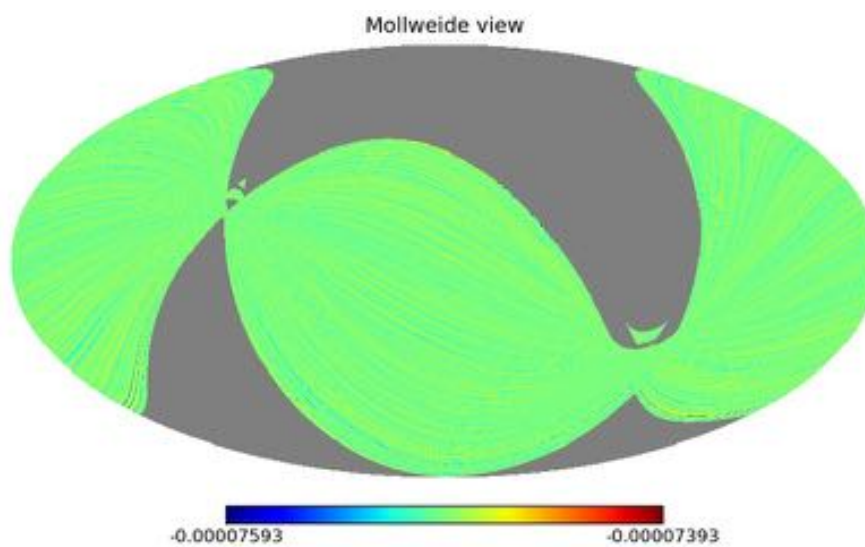


Figure 5.18: Map in intensity of the systematic effect from BEU fluctuations, 44 GHz channel, OD 91-215

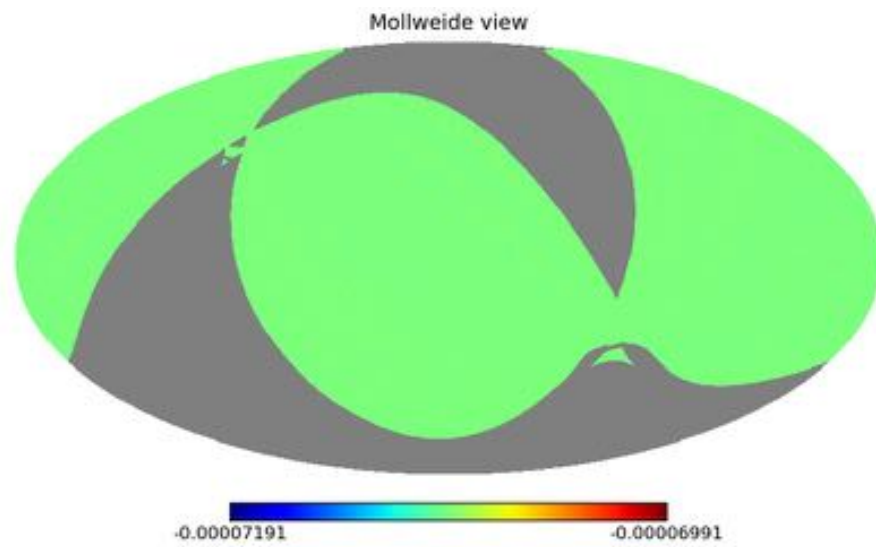


Figure 5.19: Map in intensity of the systematic effect from BEU fluctuations, 44 GHz channel, OD 275-389

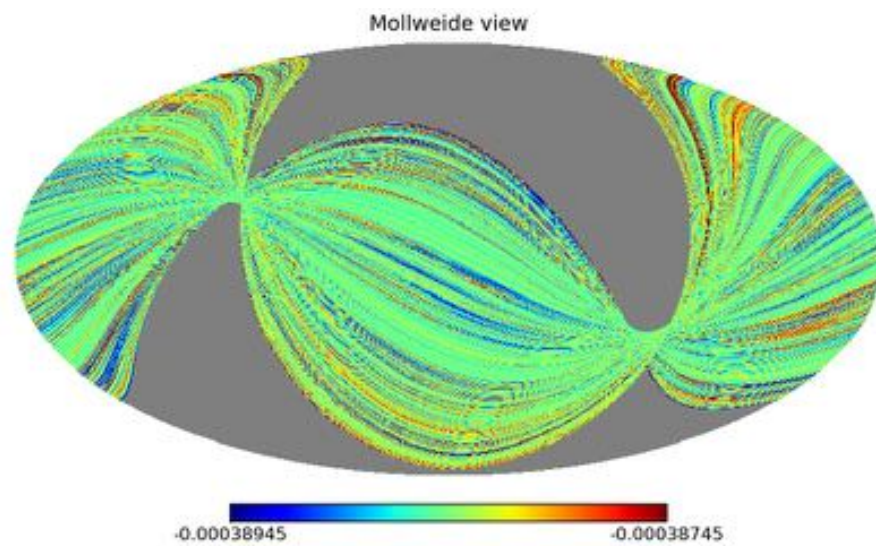


Figure 5.20: Map in intensity of the systematic effect from BEU fluctuations, 70 GHz channel, OD 91-215

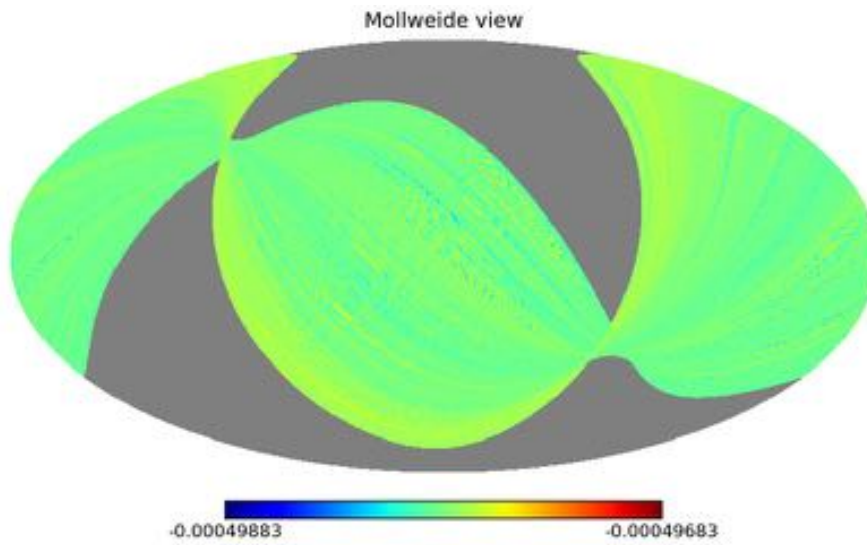


Figure 5.21: Map in intensity of the systematic effect from BEU fluctuations, 70 GHz channel, OD 275-389

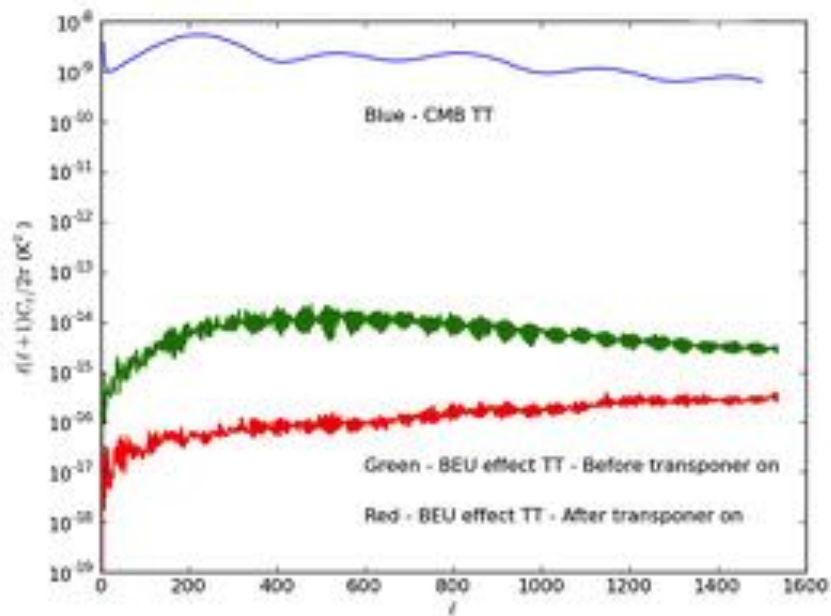


Figure 5.22: Power spectrum from the effect of the BEU temperature fluctuations (TT), 30 GHz channel, OD 91-215 and OD 275-389

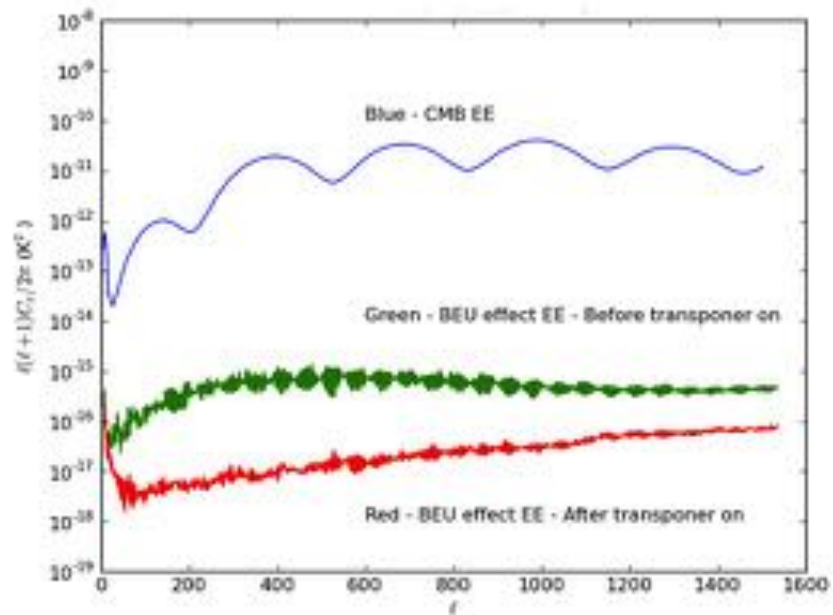


Figure 5.23: Power spectrum from the effect of the BEU temperature fluctuations (EE), 30 GHz channel, OD 91-215 and OD 275-389

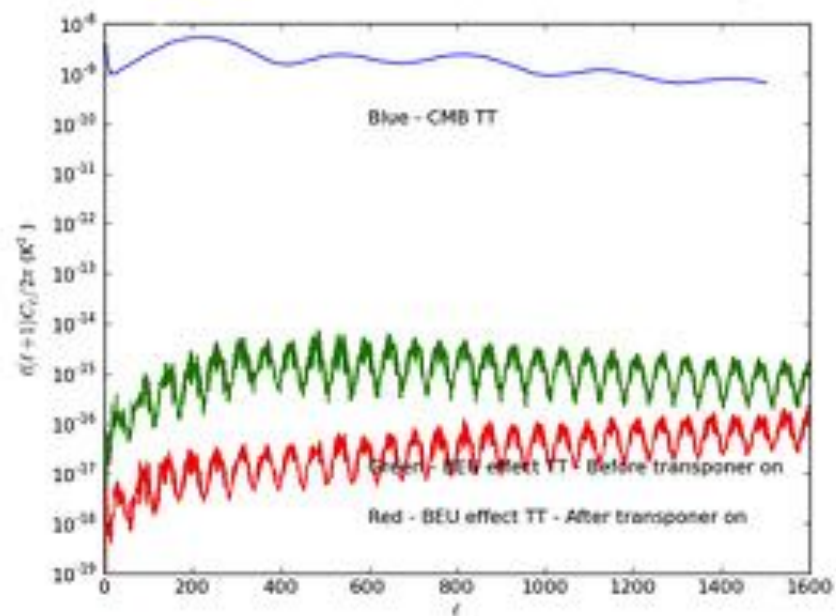


Figure 5.24: Power spectrum from the effect of the BEU temperature fluctuations (TT), 44 GHz channel, OD 91-215 and OD 275-389

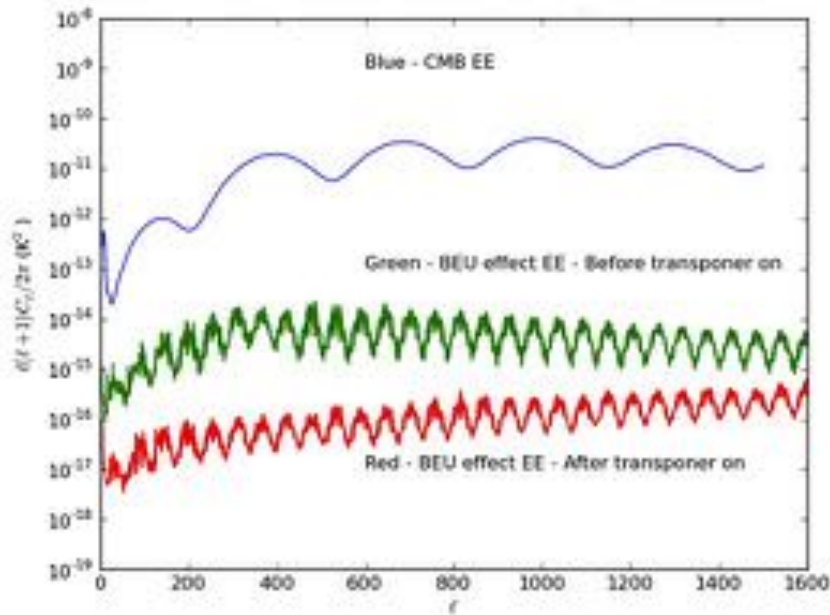


Figure 5.25: Power spectrum from the effect of the BEU temperature fluctuations (EE), 44 GHz channel, OD 91-215 and OD 275-389

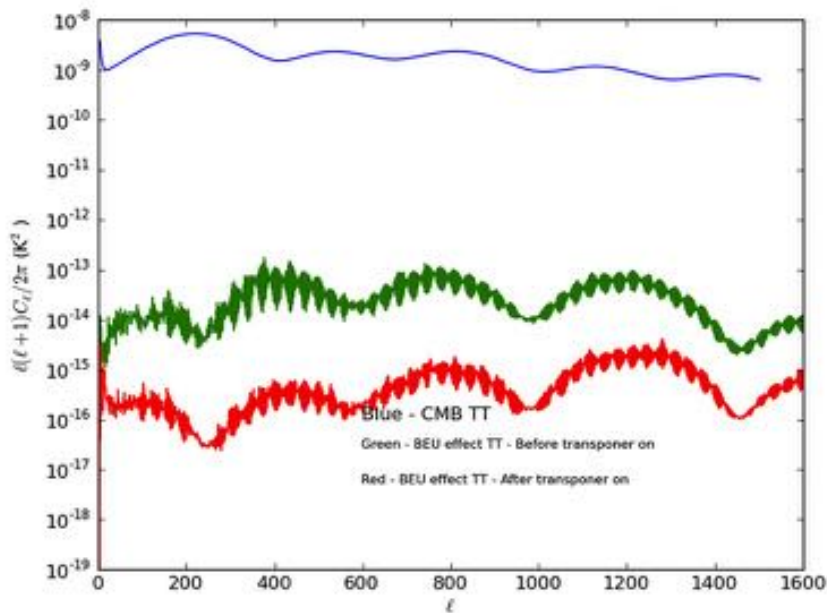


Figure 5.26: Power spectrum from the effect of the BEU temperature fluctuations (TT), 70 GHz channel, OD 91-215 and OD 275-389

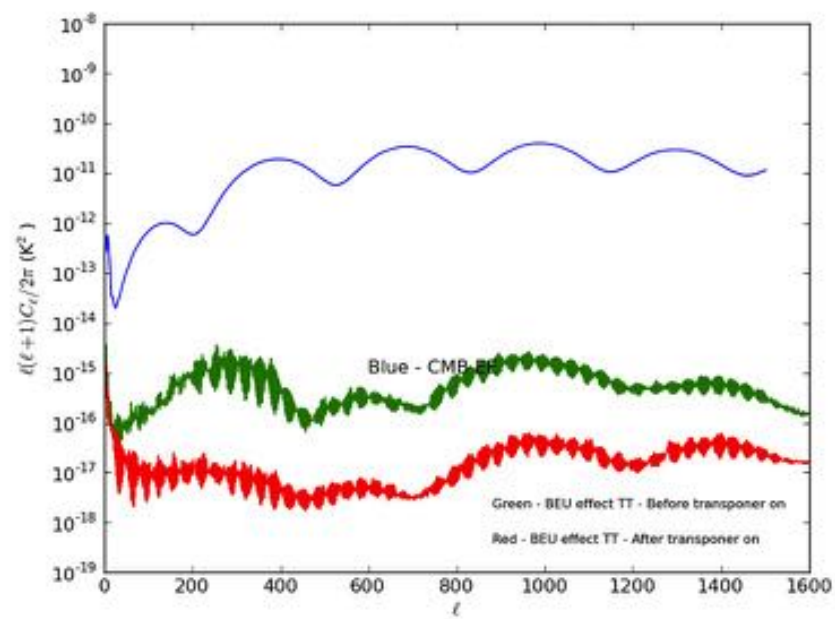


Figure 5.27: Power spectrum from the effect of the BEU temperature fluctuations (EE), 70 GHz channel, OD 91-215 and OD 275-389

5.2 Front-end temperature fluctuations

5.2.1 Analysis of the period from OD 91 to OD 389

The analysis of the overall thermal systematic effects was performed with the housekeeping time-ordered data from LM305322 and LM202322, corresponding to two reference sensors placed on the right and left part of the focal plane, respectively. The resulting maps and power spectra are here displayed for each frequency band.

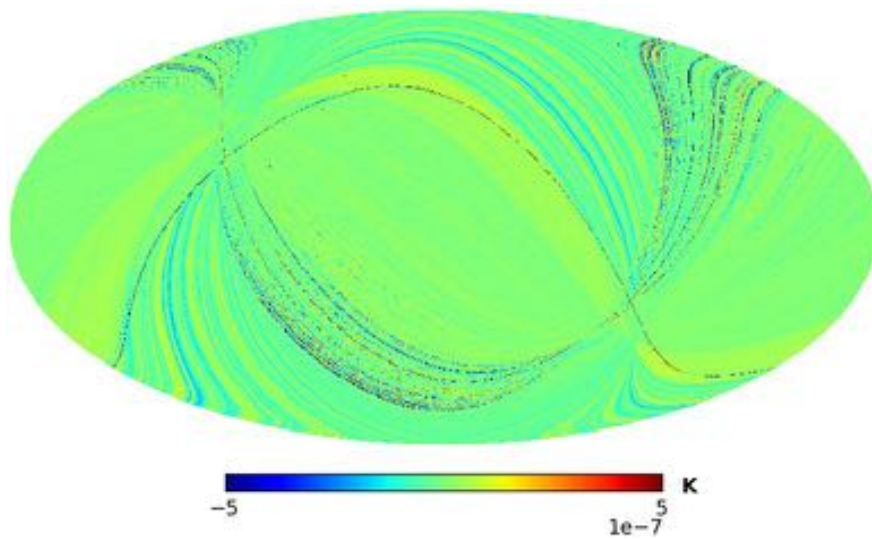


Figure 5.28: Map in intensity of the systematic effect from FEU fluctuations, 30 GHz channel, OD 91-389

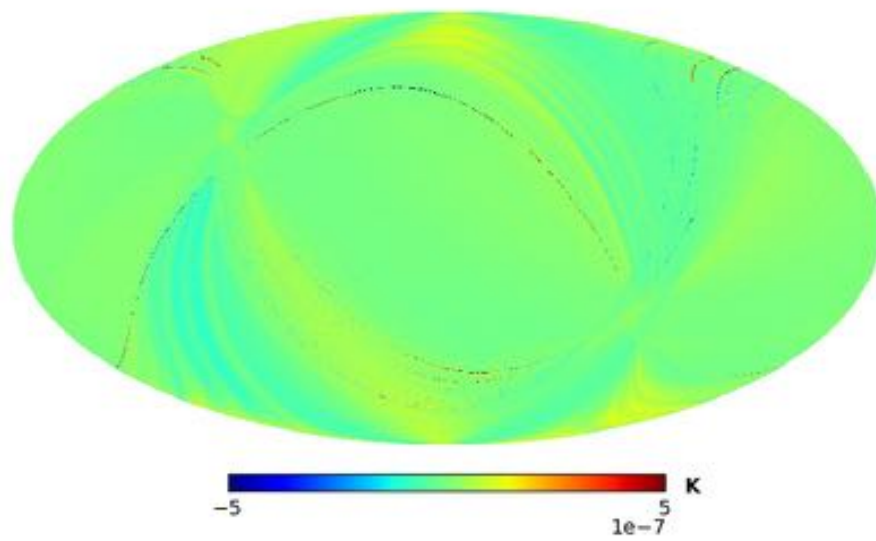


Figure 5.29: Map in polarisation Q of the systematic effect from FEU fluctuations, 30 GHz channel, OD 91-389

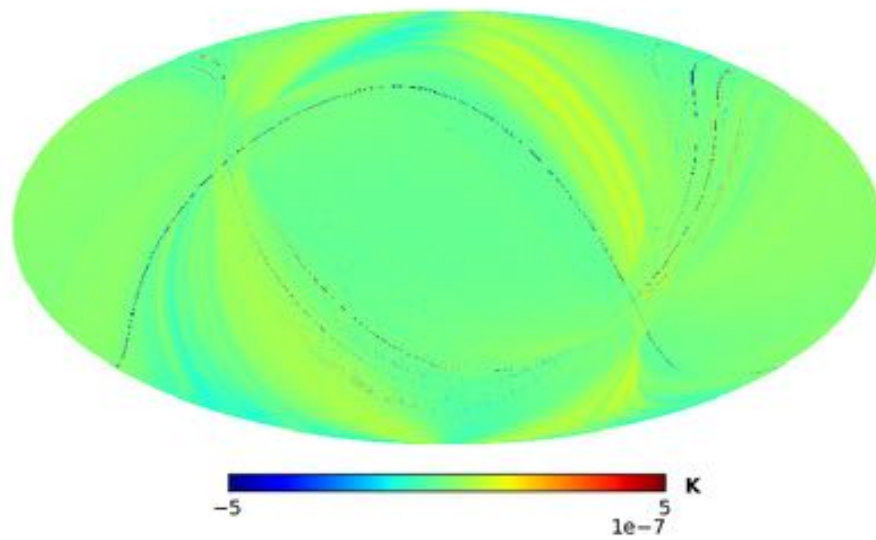


Figure 5.30: Map in polarisation U of the systematic effect from FEU fluctuations, 30 GHz channel, OD 91-389

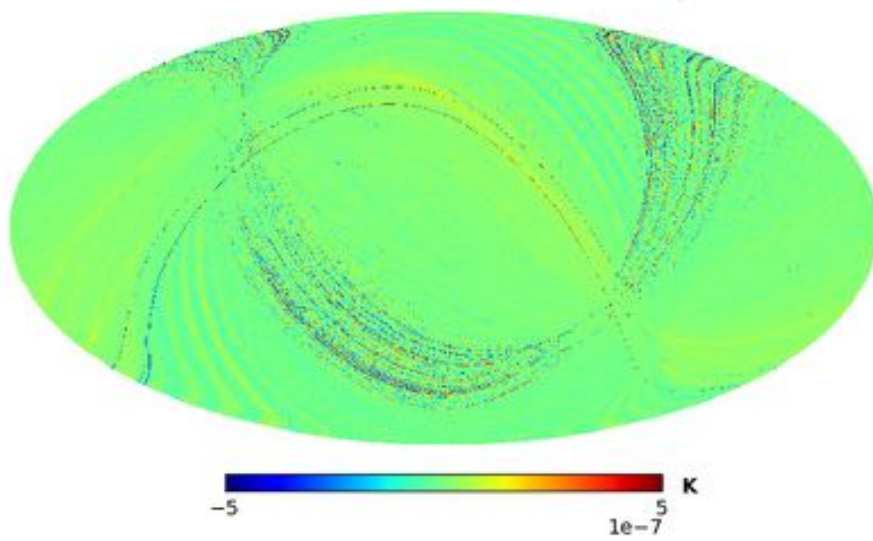


Figure 5.31: Map in intensity of the systematic effect from FEU fluctuations, 44 GHz channel, OD 91-389

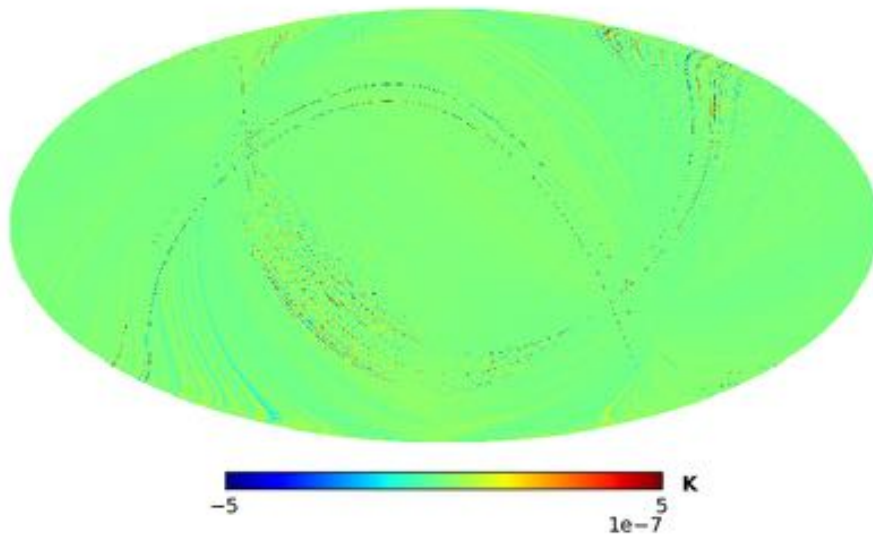


Figure 5.32: Map in polarisation Q of the systematic effect from FEU fluctuations, 44 GHz channel, OD 91-389

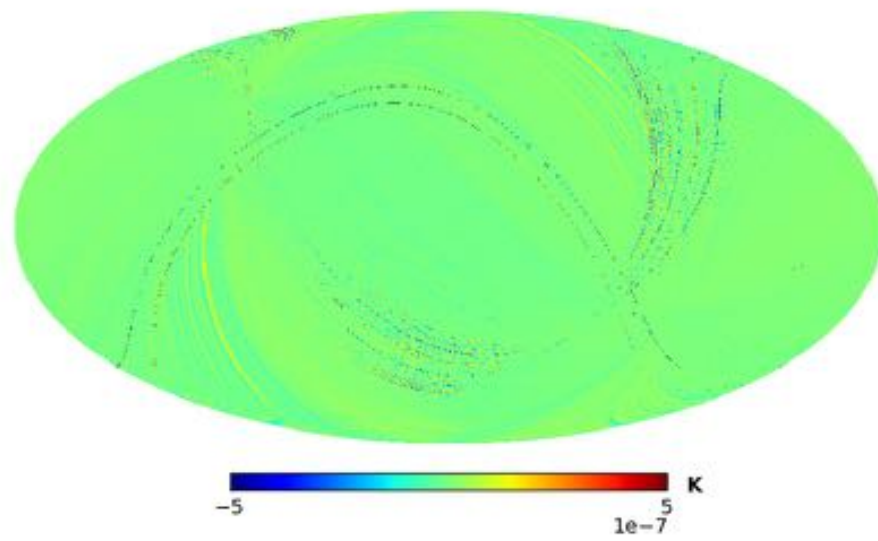


Figure 5.33: Map in polarisation U of the systematic effect from FEU fluctuations, 44 GHz channel, OD 91-389

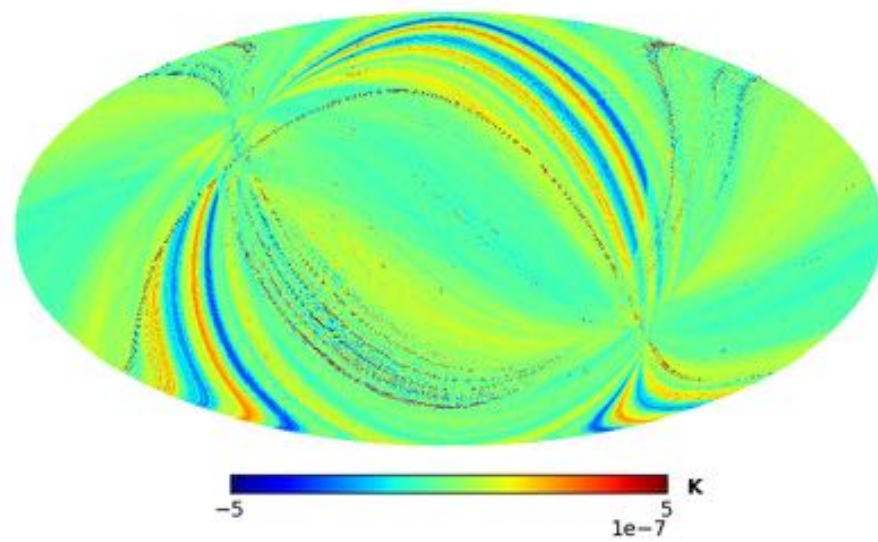


Figure 5.34: Map in intensity of the systematic effect from FEU fluctuations, 70 GHz channel, OD 91-389

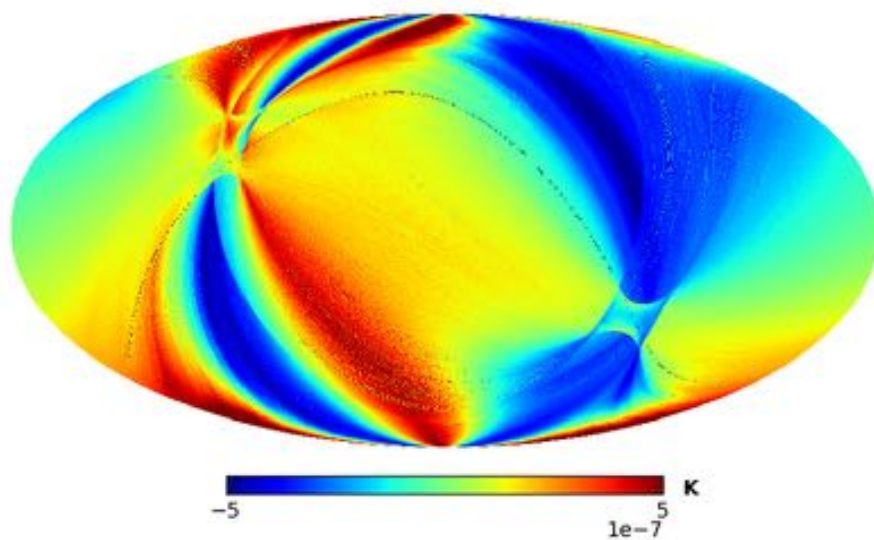


Figure 5.35: Map in polarisation Q of the systematic effect from FEU fluctuations, 70 GHz channel, OD 91-389

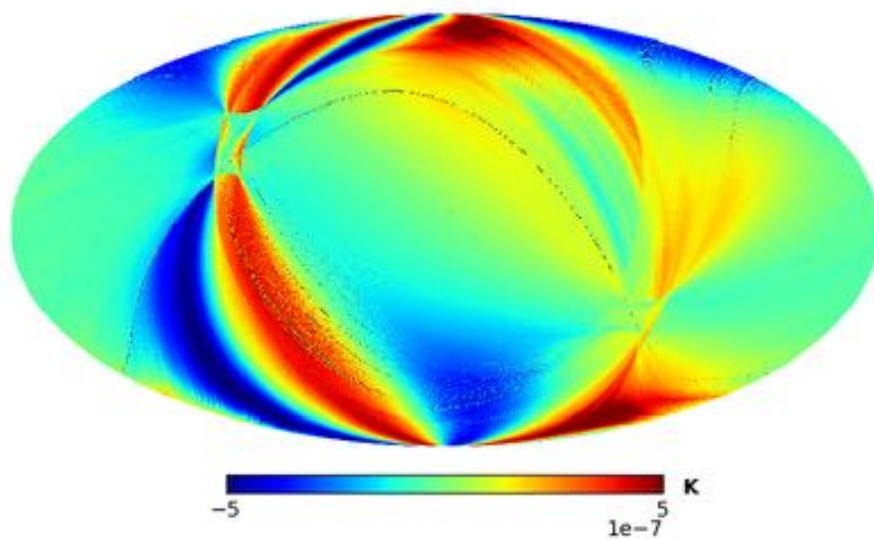


Figure 5.36: Map in polarisation U of the systematic effect from FEU fluctuations, 70 GHz channel, OD 91-389

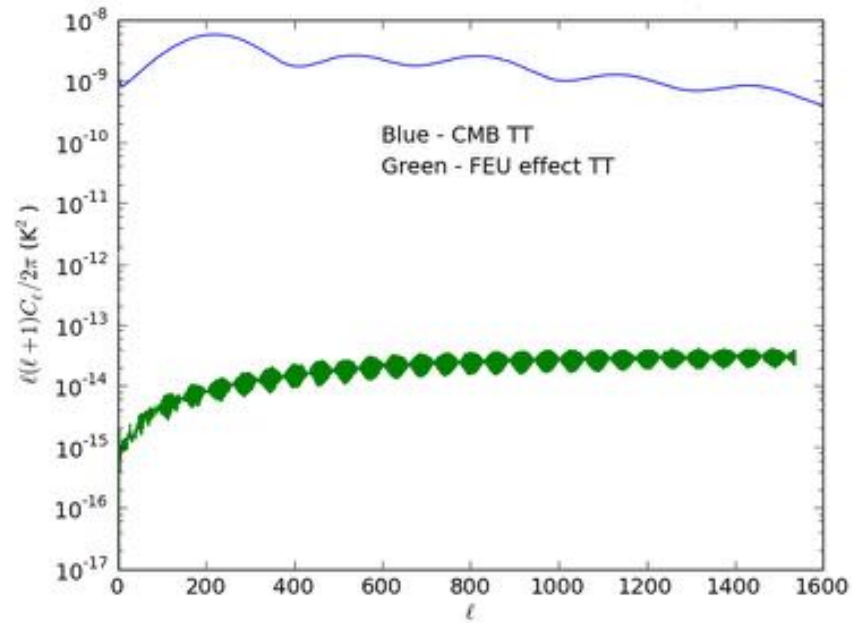


Figure 5.37: Power spectrum from the effect of the FEU temperature fluctuations (TT), 30 GHz channel, OD 91-389

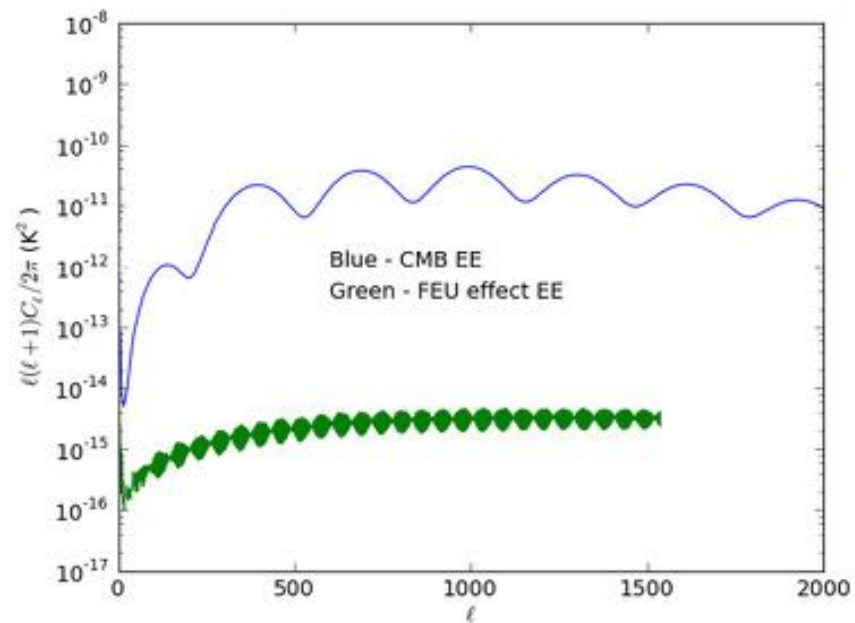


Figure 5.38: Power spectrum from the effect of the FEU temperature fluctuations (EE), 30 GHz channel, OD 91-389

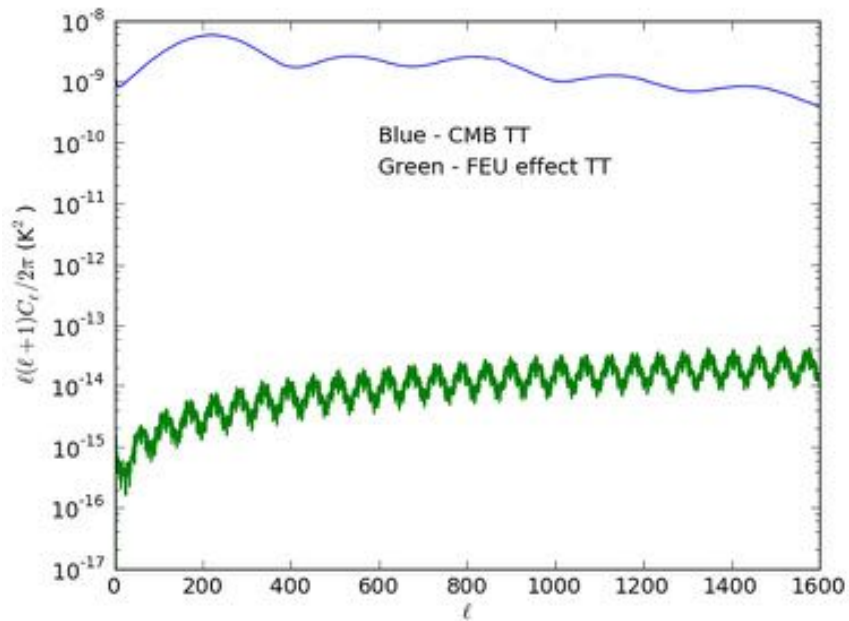


Figure 5.39: Power spectrum from the effect of the FEU temperature fluctuations (TT), 44 GHz channel, OD 91-389

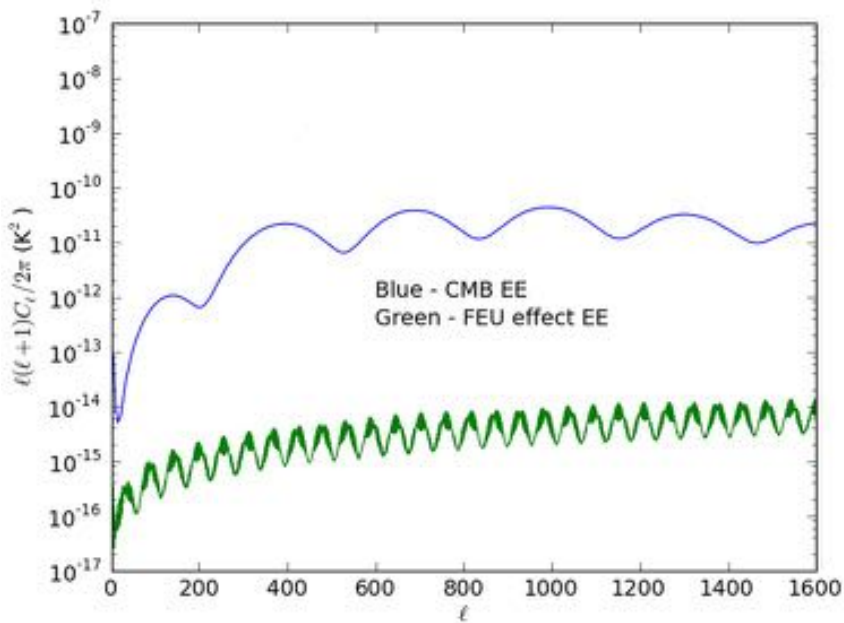


Figure 5.40: Power spectrum from the effect of the FEU temperature fluctuations (EE), 44 GHz channel, OD 91-389

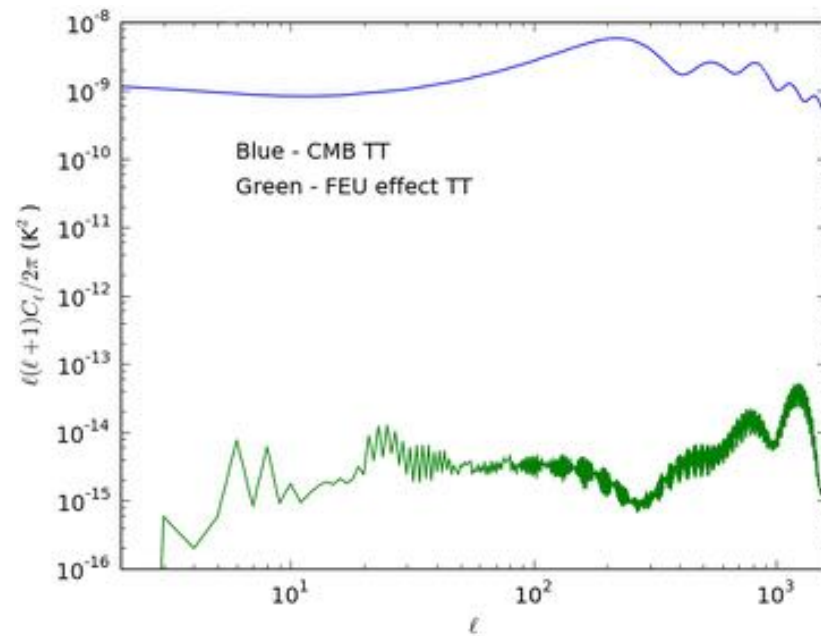


Figure 5.41: Power spectrum from the effect of the FEU temperature fluctuations (TT), 70 GHz channel, OD 91-389

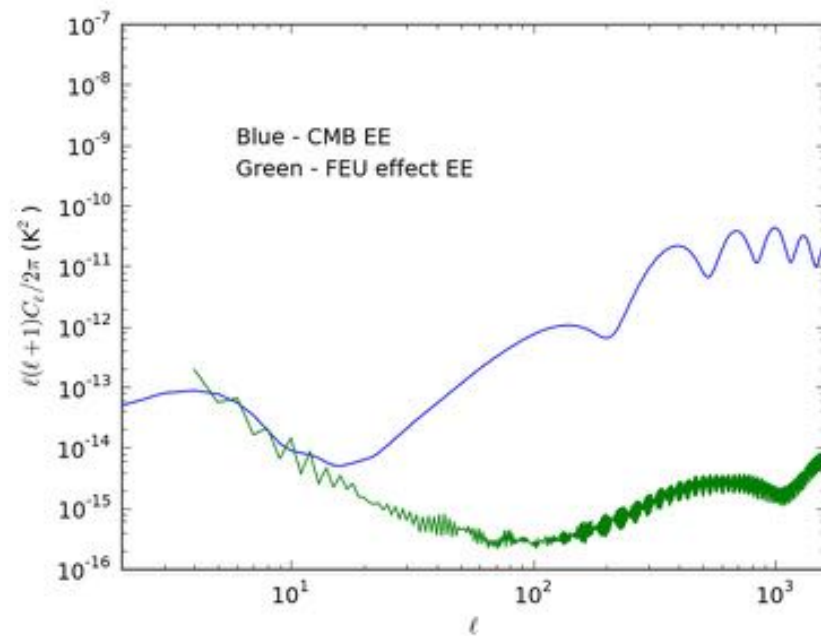


Figure 5.42: Power spectrum from the effect of the FEU temperature fluctuations (EE), 70 GHz channel, OD 91-389

5.2.2 Analysis in the periods OD 91-115 and OD 275-389

Here we estimated the sorption cooler effect using housekeeping time-ordered data from SM020540 which corresponds to the sorption cooler TSA temperature sensor. We confront two periods of the first survey, the first from OD 91 to 215 and the second from OD 275 to 389. The resulting maps and power spectra are here displayed for each frequency band.

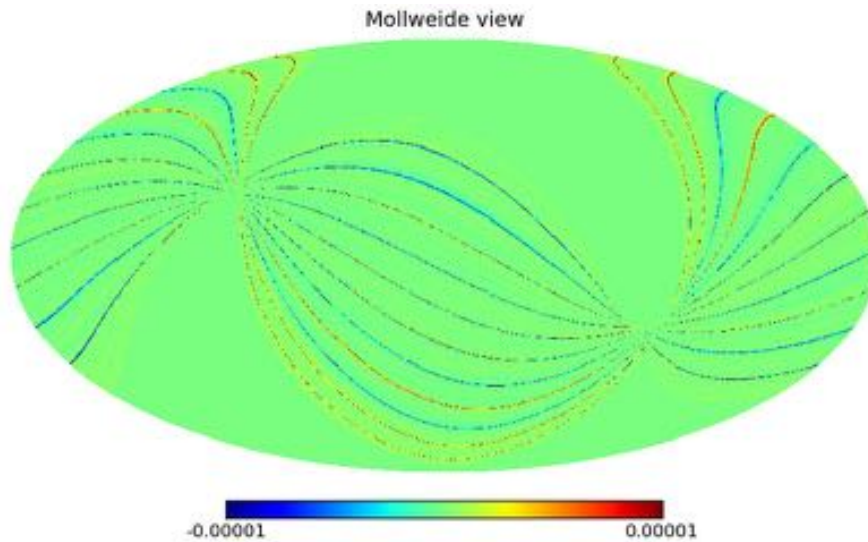


Figure 5.43: Map in intensity of the systematic effect from FEU fluctuations, 30 GHz channel, OD 91-215

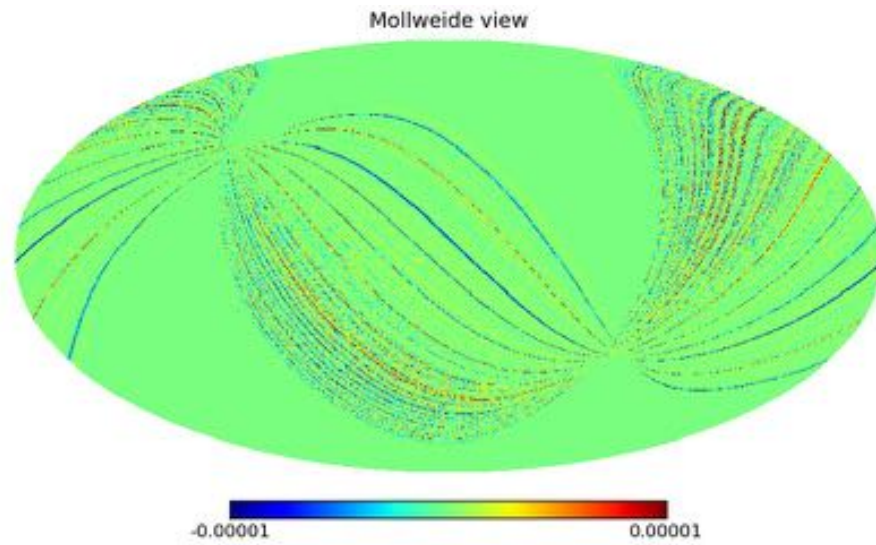


Figure 5.44: Map in intensity of the systematic effect from FEU fluctuations, 30 GHz channel, OD 275-389

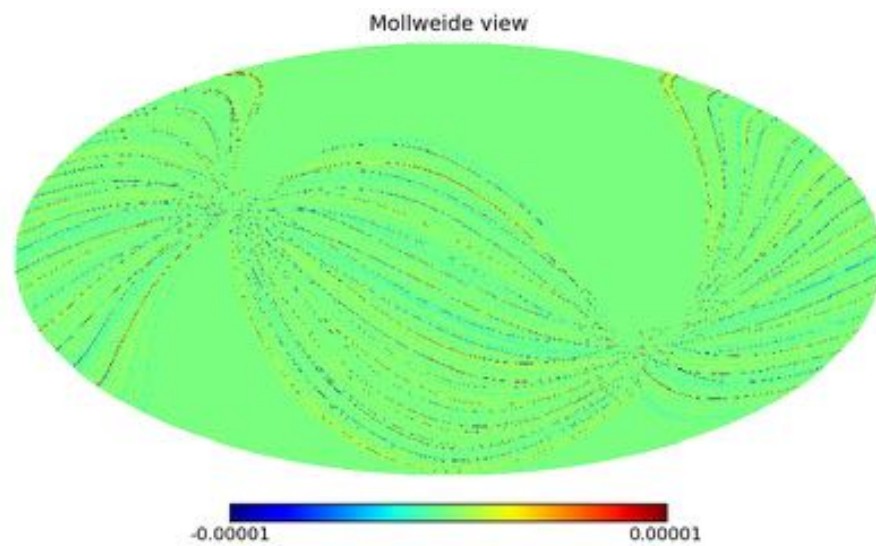


Figure 5.45: Map in intensity of the systematic effect from FEU fluctuations, 44 GHz channel, OD 91-215

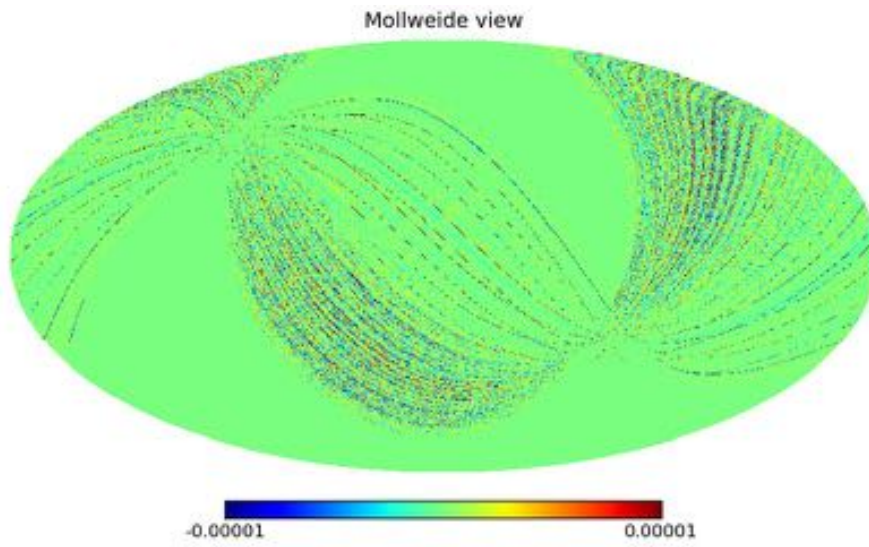


Figure 5.46: Map in intensity of the systematic effect from FEU fluctuations, 44 GHz channel, OD 275-389

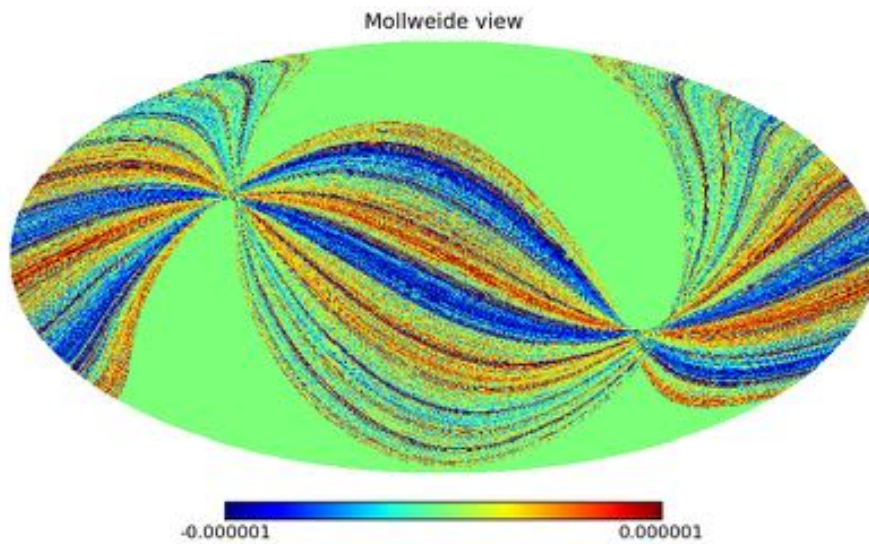


Figure 5.47: Map in intensity of the systematic effect from FEU fluctuations, 70 GHz channel, OD 91-215

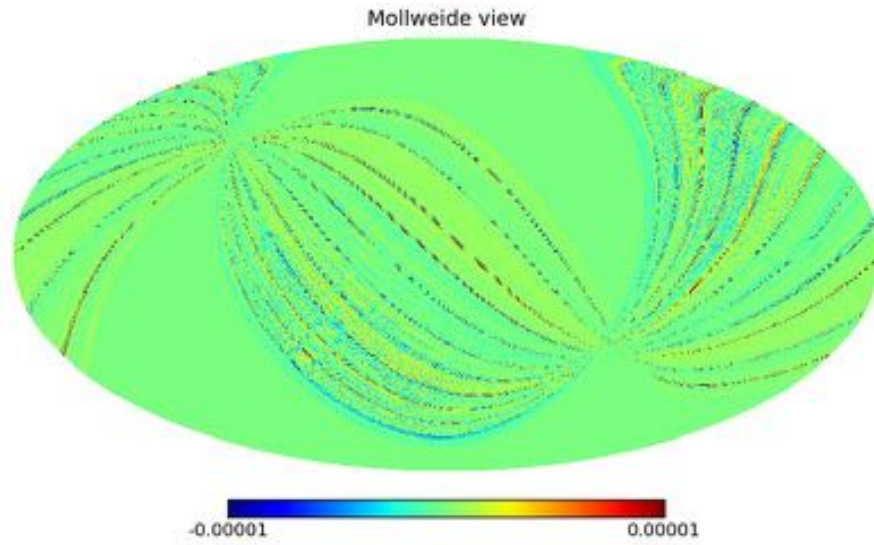


Figure 5.48: Map in intensity of the systematic effect from FEU fluctuations, 70 GHz channel, OD 275-389

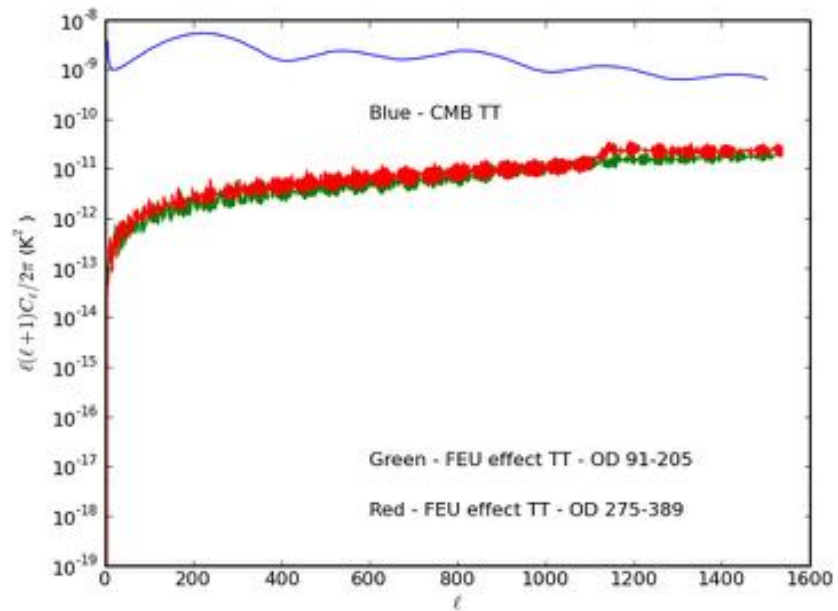


Figure 5.49: Power spectrum from the effect of the FEU temperature fluctuations (TT), 30 GHz channel, OD 91-215 and OD 275-389

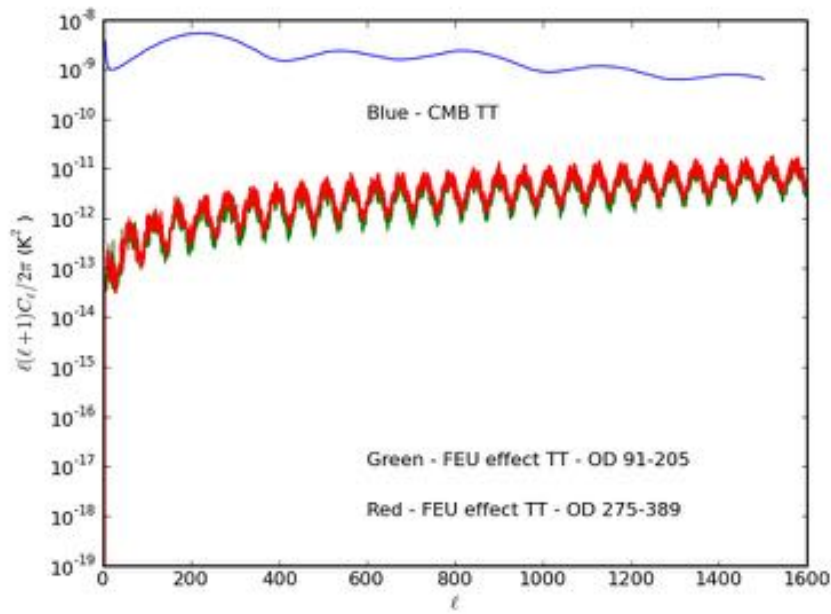


Figure 5.50: Power spectrum from the effect of the FEU temperature fluctuations (TT), 44 GHz channel, OD 91-215 and OD 275-389

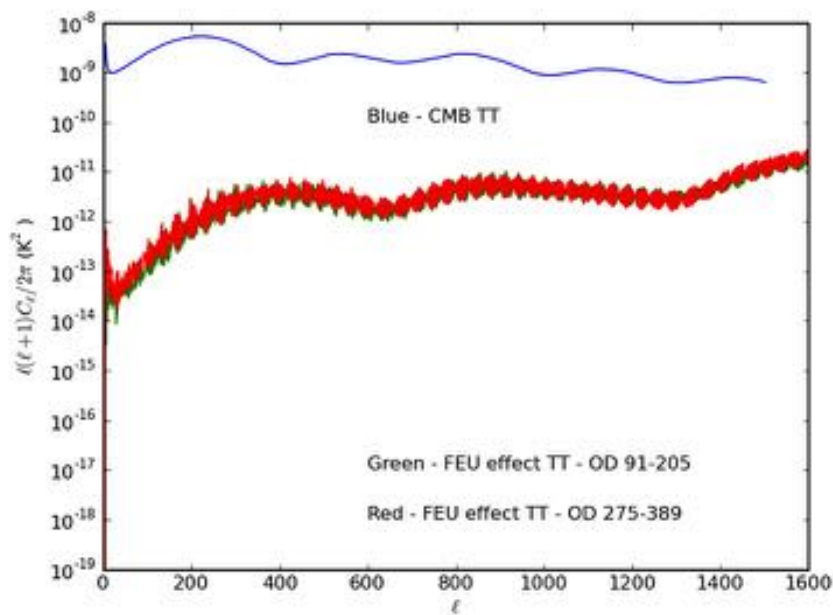


Figure 5.51: Power spectrum from the effect of the FEU temperature fluctuations (TT), 70 GHz channel, OD 91-215 and OD 275-389

5.3 4 K reference load temperature fluctuations

5.3.1 Analysis of the period from OD 91 to OD 389

The analysis of the overall thermal systematic effects was performed with the housekeeping time-ordered data from L1_A5 corresponding to sensor for the 4 K reference load near to the 30 and 44 GHz radiometer and PIDN corresponding to sensor for the 4 K reference load near to the 70 GHz. The resulting maps and power spectra are here displayed for each frequency band. The white noise is also plotted for comparison.

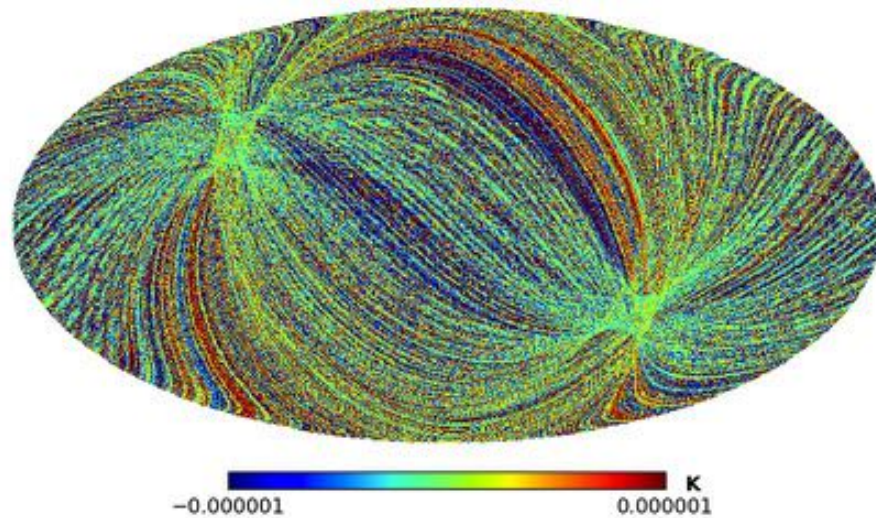


Figure 5.52: Map in intensity of the systematic effect from 4 K reference load fluctuations, 30 GHz channel, OD 91-389

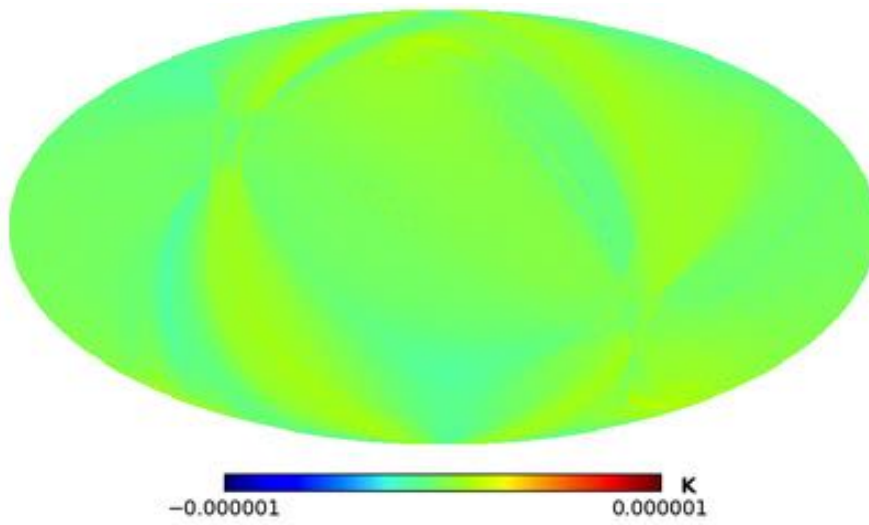


Figure 5.53: Map in polarisation Q of the systematic effect from 4 K reference load fluctuations, 30 GHz channel, OD 91-389

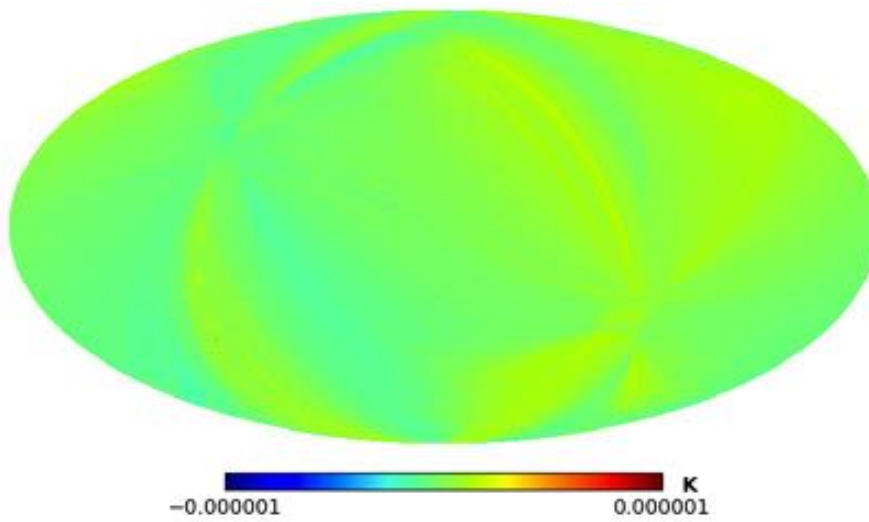


Figure 5.54: Map in polarisation U of the systematic effect from 4 K reference load fluctuations, 30 GHz channel, OD 91-389

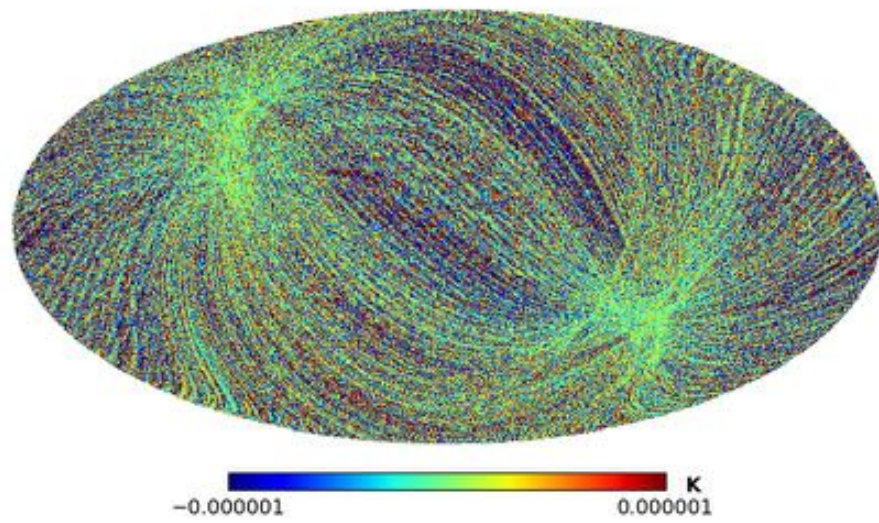


Figure 5.55: Map in intensity of the systematic effect from 4 K reference load fluctuations, 44 GHz channel, OD 91-389

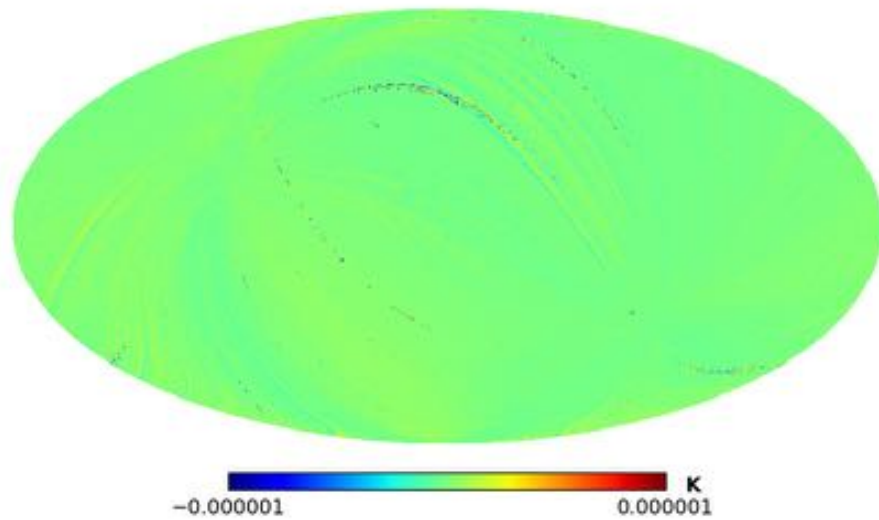


Figure 5.56: Map in polarisation Q of the systematic effect from 4 K reference load fluctuations, 44 GHz channel, OD 91-389

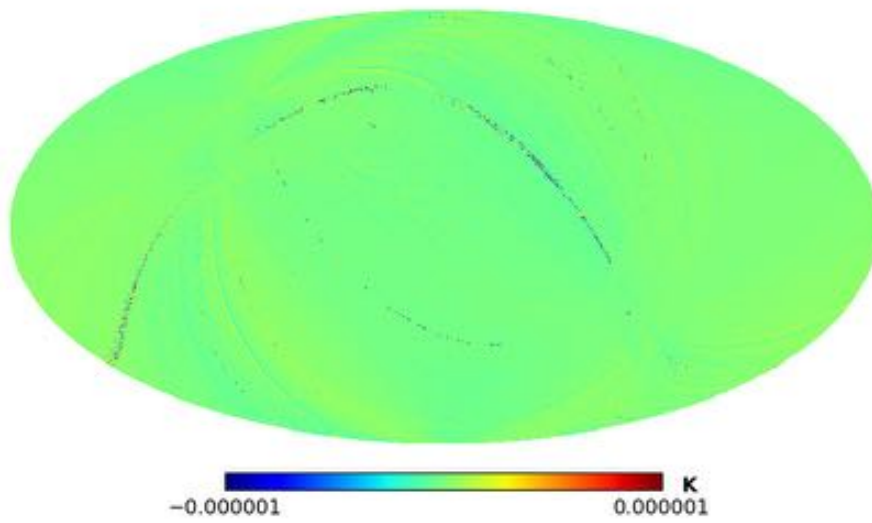


Figure 5.57: Map in polarisation U of the systematic effect from 4 K reference load fluctuations, 44 GHz channel, OD 91-389

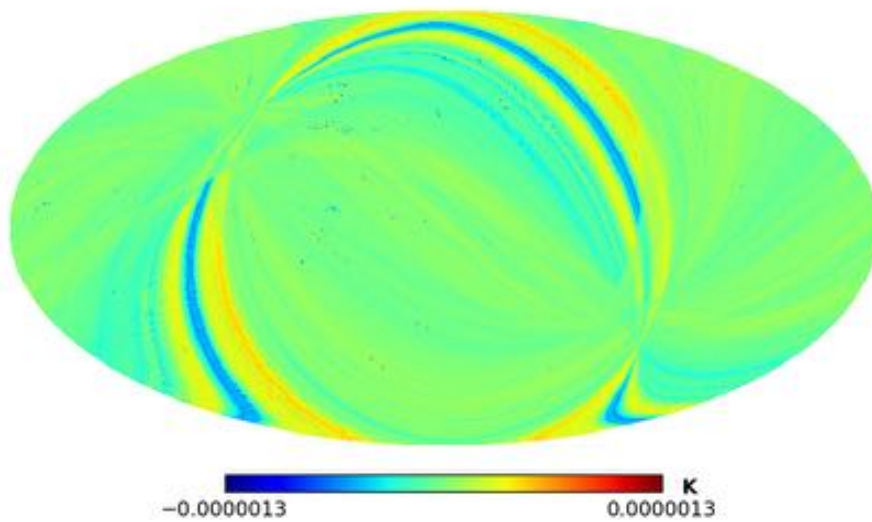


Figure 5.58: Map in intensity of the systematic effect from 4 K reference load fluctuations, 70 GHz channel, OD 91-389

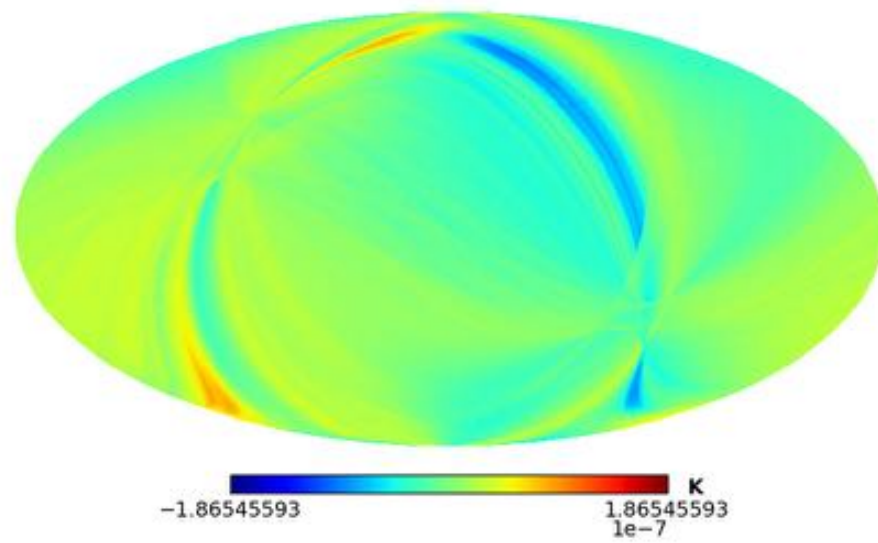


Figure 5.59: Map in polarisation Q of the systematic effect from 4 K reference load fluctuations, 70 GHz channel, OD 91-389

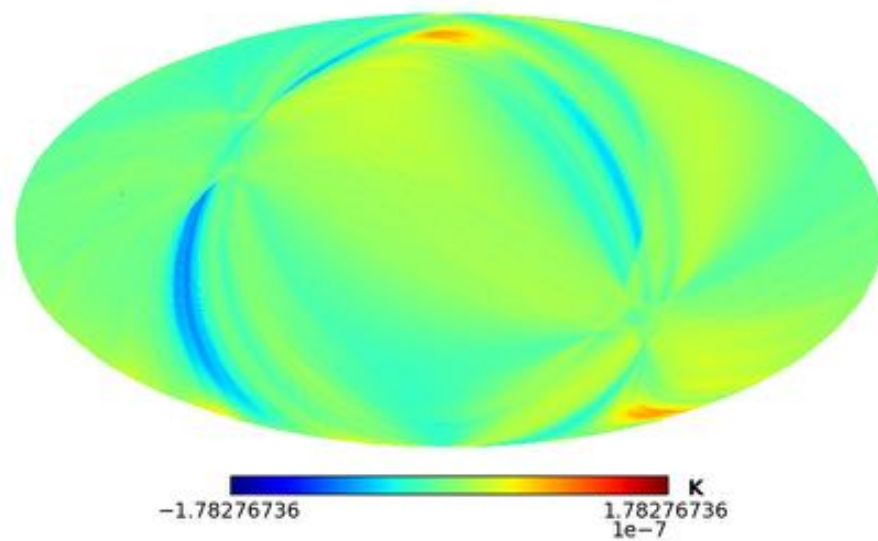


Figure 5.60: Map in polarisation U of the systematic effect from 4 K reference load fluctuations, 70 GHz channel, OD 91-389

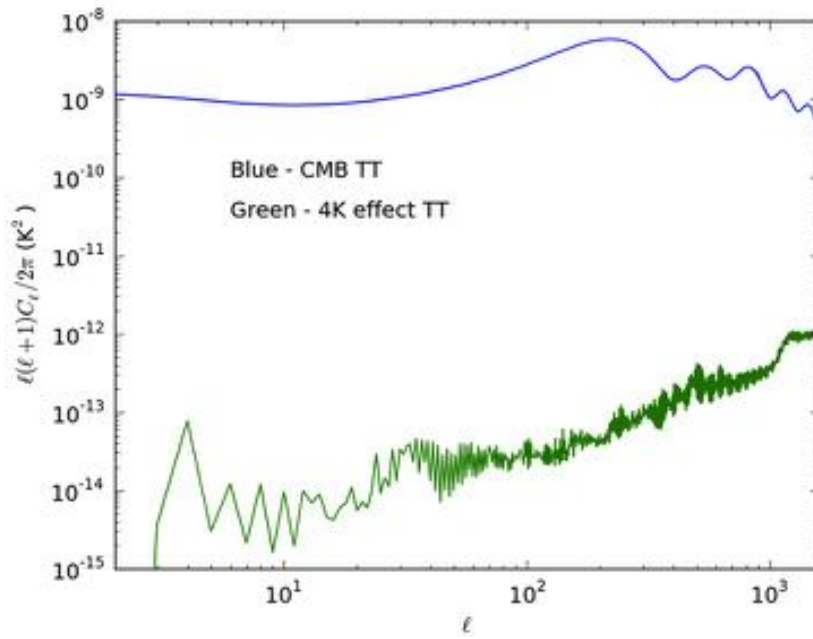


Figure 5.61: Power spectrum from the effect of the 4 K reference load temperature fluctuations (TT), 30 GHz channel, OD 91-389

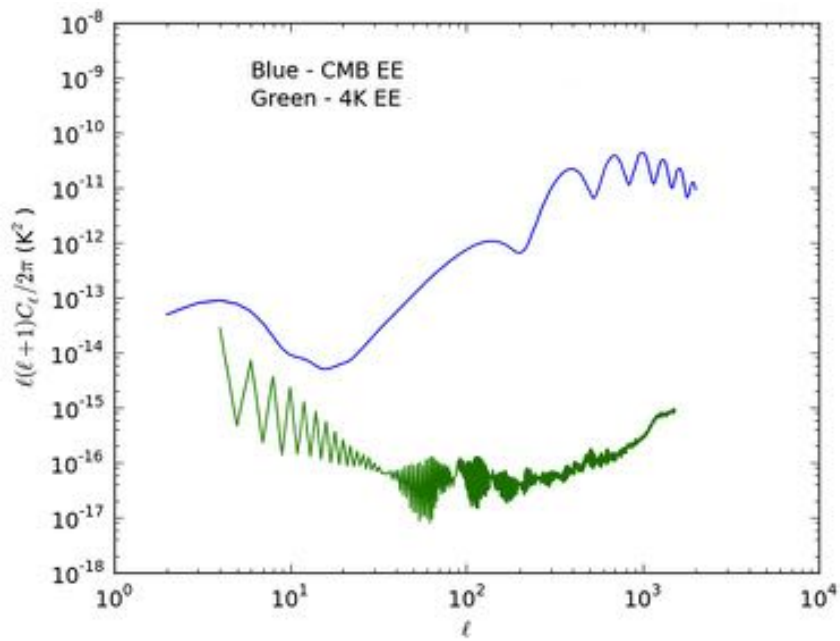


Figure 5.62: Power spectrum from the effect of the 4 K reference load temperature fluctuations (EE), 30 GHz channel, OD 91-389

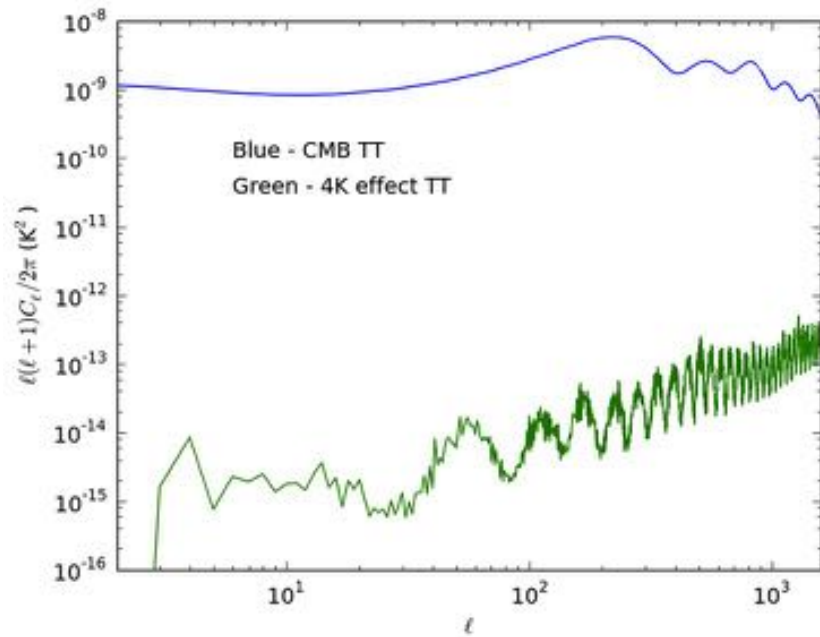


Figure 5.63: Power spectrum from the effect of the 4 K reference load temperature fluctuations (TT), 44 GHz channel, OD 91-389

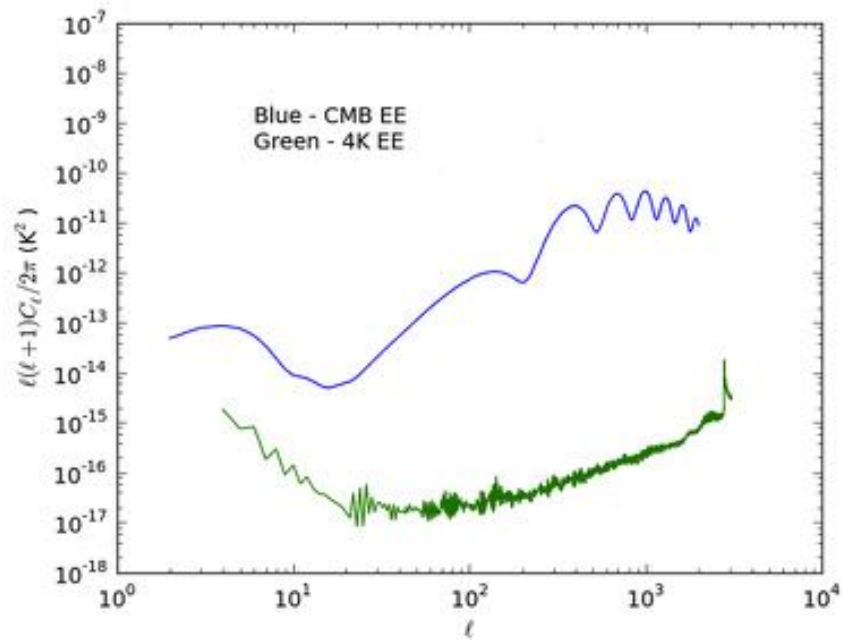


Figure 5.64: Power spectrum from the effect of the 4 K reference load temperature fluctuations (EE), 44 GHz channel, OD 91-389

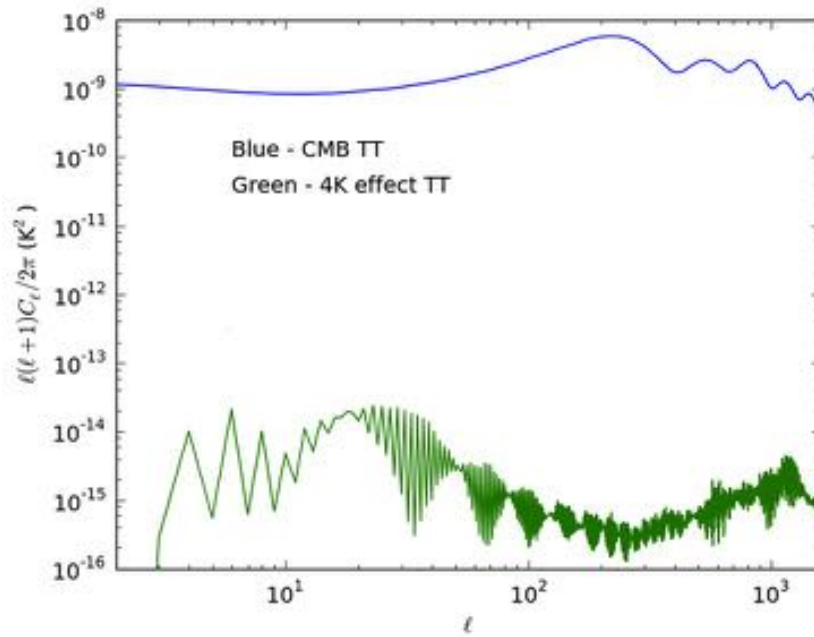


Figure 5.65: Power spectrum from the effect of the 4 K reference load temperature fluctuations (TT), 70 GHz channel, OD 91-389

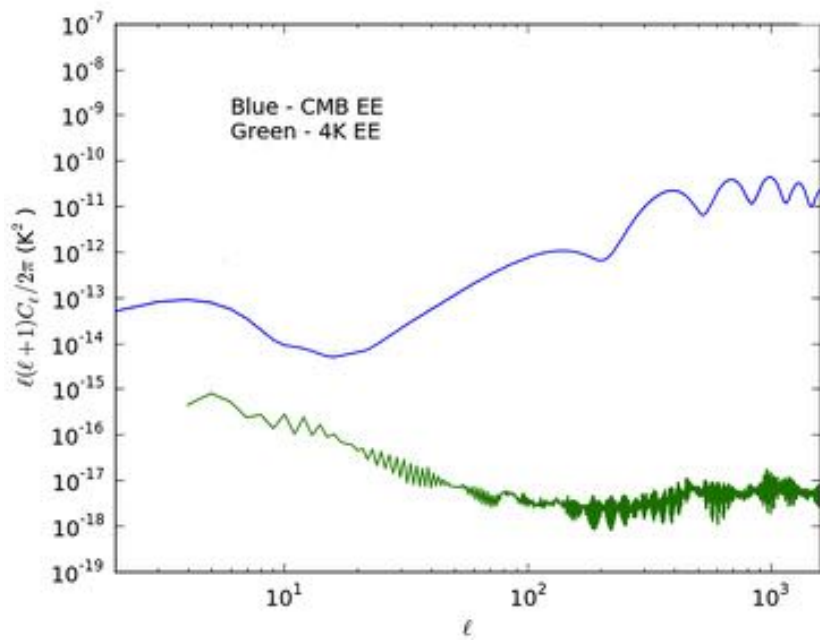


Figure 5.66: Power spectrum from the effect of the 4 K reference load temperature fluctuations (EE), 70 GHz channel, OD 91-389

Power spectra of the ratio of the systematic effect and of the instrument noise

Here we show the power spectra of the ratio $\rho_l = C_l^{syst}/C_l^{noise}$, where C_l^{syst} is the noise angular power spectrum of the systematic effect map and C_l^{noise} is the angular power spectrum of the instrument noise contribution including the residual $1/f$ component remaining after destriping [34]. The power spectra are shown for the three LFI frequency channels.

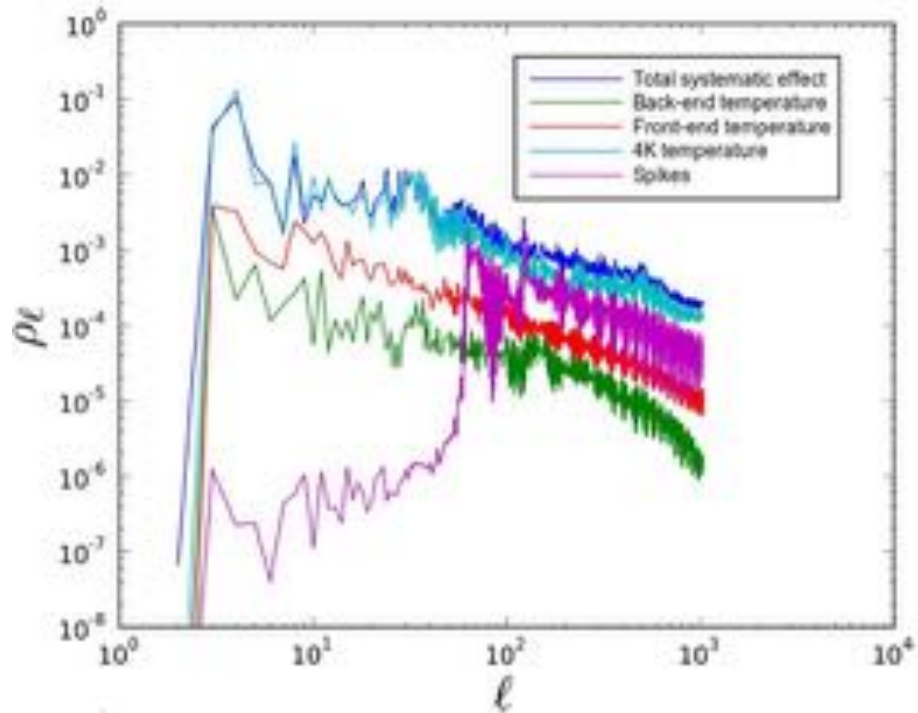


Figure 5.67: Ratio $\rho_l = C_{syst}/C_{noise}$ for the 30 GHz LFI frequency channel.

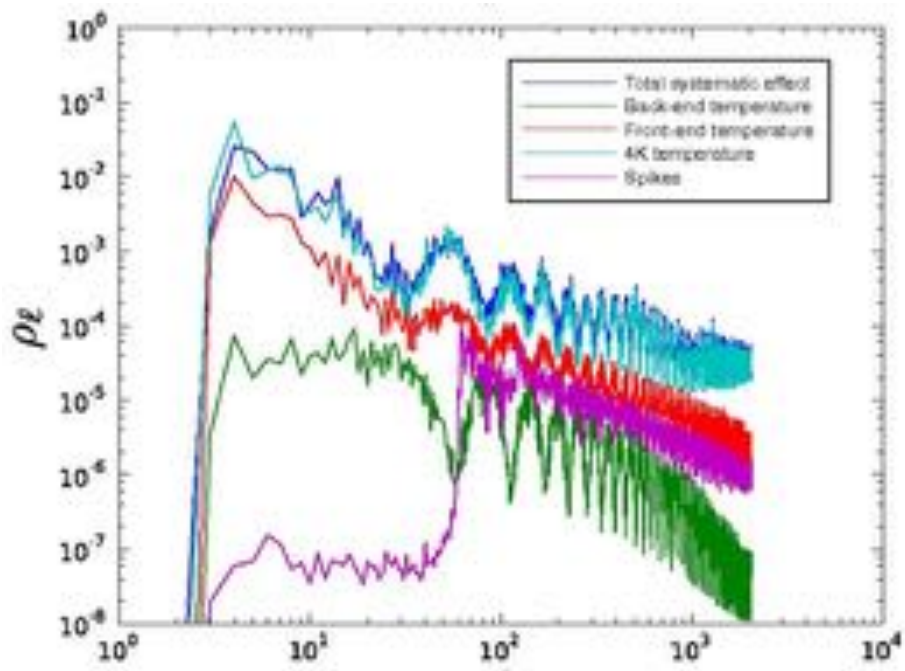


Figure 5.68: Ratio $\rho_\ell = C_{syst}/C_{noise}$ for the 44 GHz LFI frequency channel.

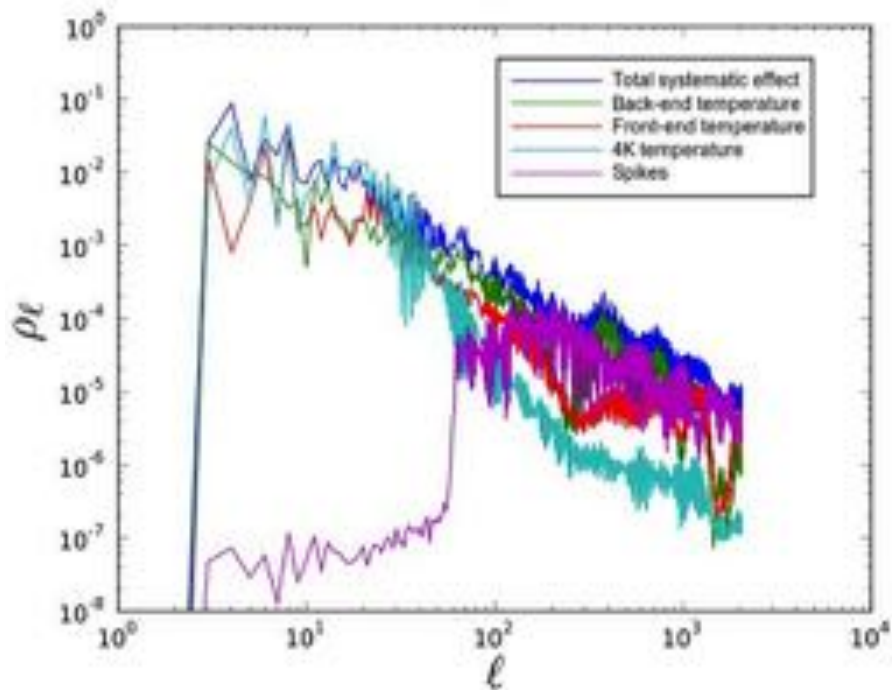


Figure 5.69: Ratio $\rho_\ell = C_{syst}/C_{noise}$ for the 70 GHz LFI frequency channel.

Table 5.1: Overview of our current assessment of residual peak-to-peak and rms thermal systematic effects per pixel on LFI temperature maps. The units are μK_{CMB} . The total has been estimated from the maps combining all systematic effects. [34]

Source	30 GHz		44 GHz		70 GHz	
	p-p	r.m.s	p-p	r.m.s	p-p	r.m.s
BEU	1.27	0.11	0.63	0.05	2.70	0.24
FEU	1.05	0.23	1.15	0.22	1.12	0.21
4 K load	9.76	0.98	9.73	0.98	1.30	0.16
Total	10.92	1.10	9.73	0.98	4.28	0.45

Chapter 6

Conclusions and perspectives

The work of this thesis studied the thermal systematic effects by producing maps and power spectra exploiting flight radiometric and housekeeping data from sensors located on the back-end unit, front-end unit and 4 K reference loads. We performed this analysis first on full-sky maps, then we applied it to two different periods covering the same area of the sky in order to enhance the eventual change in the fluctuations. We can summarize the results as:

- the back end unit fluctuations in the period from Operational Day 91 to 389 show ≈ 5 orders of magnitude below the compared CMB signal, while the EE power spectra are $\approx 4 - 5$ orders of magnitude below. Regarding the analysis in the two periods (OD 91-115 and OD 275-389), we can notice improvement by an order of magnitude in the second period due to the transponder's constant power ON;
- the back end unit fluctuations in the period from Operational Day 91 to 389 show ≈ 6 orders of magnitude below the compared CMB signal, while the EE power spectra are $\approx 4 - 5$ orders of magnitude below. Regarding the analysis in the two different periods (OD 91-115 and OD 275-389), we can notice that the deterioration in the later period due to the degradation of the sorption cooler is almost irrelevant;
- The 4 K reference loads fluctuation for 30 and 44 GHz show ≈ 4 orders of magnitude, while the 70 GHz show ≈ 5 orders of magnitude below compared to the CMB signal. The EE power spectra are $\approx 3 - 4$ orders of magnitude below the compared CMB signal;

In the power spectra in Figure 5.67, Figure 5.68 and Figure 5.69 the thermal instabilities in the 300 K, 20 K and 4 K stages are several orders of

magnitude below the instrumental noise at all angular scales smaller than 10° and less than 10% at larger scales. Figure 5.67, Figure 5.68 also show that at 30 and 44 GHz the largest contribution to systematic effects is determined by temperature fluctuations of the 4 K reference loads, while the residual systematic uncertainty in the 70 GHz channel is mainly caused by back-end temperature fluctuations and, at small angular scales, by frequency spikes (Figure 5.69).

Table 5.1 gives an overview of our current assessment of residual peak-to-peak and rms systematic effects per pixel on LFI temperature maps. We compared the results from Table 5.1 to the error budgets requirements for the LFI instrument in Table 4.1:

- The focal plane stability requirements (Table 4.1) demand periodic fluctuations to be less than $0.9 \mu\text{K}$ per pixel peak-to-peak in the final maps. All the frequency channels have similar peak-to-peak fluctuations $\approx 1 \mu\text{K}$ ($1.05 \mu\text{K}$ for 30 GHz, $1.15 \mu\text{K}$ for 44 GHz and $1.12 \mu\text{K}$ for 70 GHz) and what is more important the rms residual systematic uncertainty is under $1 \mu\text{K}$ per pixel $\approx 0.2 \mu\text{K}$ ($0.23 \mu\text{K}$ for 30 GHz, $0.22 \mu\text{K}$ for 44 GHz and $0.21 \mu\text{K}$ for 70 GHz).
- The back-end unit requirements (Table 4.1) demand periodic fluctuations less to be than $0.4 \mu\text{K}$ per pixel peak-to-peak in the final maps. The three frequency channels have different peak-to-peak fluctuations ($1.27 \mu\text{K}$ for 30 GHz, $0.63 \mu\text{K}$ for 44 GHz and slightly higher for 70 GHz $2.70 \mu\text{K}$). But again, what is more important the rms residual systematic uncertainty is under $1 \mu\text{K}$ per pixel ($0.11 \mu\text{K}$ for 30 GHz, $0.05 \mu\text{K}$ for 44 GHz and $0.24 \mu\text{K}$ for 70 GHz).
- The 4 K reference load requirements (Table 4.1) demand periodic fluctuations less to be than $0.6 \mu\text{K}$ per pixel peak-to-peak in the final maps. The three frequency channels have different peak-to-peak fluctuations ($9.76 \mu\text{K}$ for 30 GHz, $9.73 \mu\text{K}$ for 44 GHz and $1.30 \mu\text{K}$ 70 GHz). The 4 K load peak-to-peak fluctuations for the 30 and 44 GHz are ≈ 10 times higher than in the 70 GHz channel and this can represent significant contribution to the systematic overall effects. It is important that the rms residual systematic uncertainty is under $1 \mu\text{K}$ per pixel ($0.98 \mu\text{K}$ for 30 and 44 GHz and $0.16 \mu\text{K}$ for 70 GHz). The reasons for this

behavior for the 30 and 44 GHz reference loads is due to the distance from the PID source (discussed in chapter 3).

In conclusion, we can confirm that the scientific requirements are satisfied, but our work contributes to enhance that the most critical thermal systematic effect in the LFI instrument is the one which comes from the 30 and 44 GHz 4 K reference loads fluctuations. Further work in the data analysis and the destriping technique will be aimed to further reduce the residual effect caused by these fluctuations.

Appendix

List of Abbreviations

CMB - Cosmic Microwave Background

COBE- Cosmic Background Explorer

DAE - Data Acquisition Electronics

HEALPix - Hierarchical Equal Area isoLatitude Pixelization

HFI - High Frequency Instrument

IDIS - Integrated Data and Information System

LFI - Low Frequency Instrument

LNA - Low Noise Amplifier

OD - Operational Day

OMT - Ortho-Mode Transducer

TOI - Time Ordered Information

WMAP - Wilkinson Microwave Anisotropy Probe

Bibliography

- [1] S. Weinberg. *Cosmology*. Oxford University Press, 2008.
- [2] P. Coles and F. Lucchin. *Cosmology: The Origin and Evolution of Cosmic Structure, Second Edition*. 2002.
- [3] H. P. Robertson. Kinematics and World-Structure. *The Astrophysical Journal*, 82:284-+, 1935.
- [4] A. Friedman. On the Curvature of Space. *General Relativity and Gravitation*, 31:1991-+, 1999.
- [5] C. J. MacTavish, P. A. R. Ade, J. J. Bock et al. Cosmological Parameters from the 2003 Flight of BOOMERANG. *The Astrophysical Journal*, 647:799-812, 2006.
- [6] P. J. Peebles and B. Ratra. The cosmological constant and dark energy. *Reviews of Modern Physics*, 75:559-606, 2003.
- [7] G. Gamow. The Evolution of the Universe. *Nature*, 162:680-682, 1948.
- [8] R. A. Alpher, R. Herman and G. A. Gamow. Thermonuclear Reactions in the Expanding Universe. *Physical Review*, 74:1198-1199, 1948.
- [9] A. A. Penzias and R. W. Wilson. A Measurement of Excess Antenna Temperature at 4080 Mc/s.. *The Astrophysical Journal*, 142:419-421, 1965.
- [10] M. Bersanelli, D. Maino and A. Mennella. Anisotropies of the cosmic microwave background. *Nuovo Cimento Rivista Serie*, 25:090000-82, 2002.
- [11] A. Kogut, C. Lineweaver, G. F. Smoot et al. Dipole Anisotropy in the COBE Differential Microwave Radiometers First-Year Sky Maps. *The Astrophysical Journal*, 419:1-+, 1993.

- [12] J. C. Mather, E. S. Cheng, D. A. Cottingham et al. Measurement of the cosmic microwave background spectrum by the COBE FIRAS instrument. *The Astrophysical Journal*, 420:439-444, 1994.
- [13] R. K. Sachs and A. M. Wolfe. Perturbations of a Cosmological Model and Angular Variations of the Microwave Background. *The Astrophysical Journal*, 147:73-+, 1967.
- [14] J. Silk. Cosmic Black-Body Radiation and Galaxy Formation. *The Astrophysical Journal*, 151:459-+, 1968.
- [15] J. E. Gunn and B. A. Peterson. On the Density of Neutral Hydrogen in Intergalactic Space.. *The Astrophysical Journal*, 142:1633-1641, 1965.
- [16] R. A. Sunyaev and Y. B. Zeldovich. Small-Scale Fluctuations of Relic Radiation. *The Astrophysical Journal*, 7:3-19, 1970.
- [17] W. Hu and M. White. A CMB polarization primer. *A&A*, 2:323-344, 1997.
- [18] D. Baumann, M. G. Jackson, P. Adshead et al. Probing Inflation with CMB Polarization. In *American Institute of Physics Conference Series*, 1141:10-120, 2009.
- [19] A. Kosowsky and M. S. Turner. CBR anisotropy and the running of the scalar spectral index. *Physical Review*, 52:1739-+, 1995.
- [20] A. N. Lasenby, A. W. Jones and Y. Dabrowski. Review of Ground-Based CMB Experiments. *ArXiv Astrophysics e-prints*, 1998.
- [21] C. O'Sullivan. Observations of Anisotropies in the CMBR with the Cosmic Anisotropy Telescope. *Irish Astronomical Journal*, 23:161-+, 1996.
- [22] A. C. Taylor, P. Carreira, K. Cleary et al. First results from the Very Small Array - II. Observations of the cosmic microwave background. *The Astrophysical Journal*, 341:1066-1075, 2003.
- [23] T. J. Pearson, B. S. Mason, S. Padin et al. The Cosmic Background Imager. In *New Cosmological Data and the Values of the Fundamental Parameters*, 201:23-+, 2005.
- [24] E. M. Leitch, J. M. Kovac, N. W. Halverson et al. Degree Angular Scale Interferometer 3 Year Cosmic Microwave Background Polarization Results. *The Astrophysical Journal*, 624:10-20, 2005.

- [25] B. Rabii, C. D. Winant, J. S. Collins et al. MAXIMA: A balloon-borne cosmic microwave background anisotropy experiment. *Review of Scientific Instruments*, 77:071101-+, 2006.
- [26] W. C. Jones, P. A. R. Ade, J. J. Bock et al. Observations of the temperature and polarization anisotropies with BOOMERANG 2003. *The Astrophysical Journal*, 50:945-950, 2006.
- [27] C. L. Bennett, M. Halpern, G. Hinshaw et al. First-Year Wilkinson Microwave Anisotropy Probe (WMAP) Observations: Preliminary Maps and Basic Results. *The Astrophysical Journal*, 148:1-27, 2003.
- [28] Planck Collaboration, P. A. R. Ade, N. Aghanim et al. Planck Early Results: The Planck mission. *ArXiv e-prints*, 2011.
- [29] The Planck Collaboration. The Scientific Programme of Planck. *ArXiv Astrophysics e-prints*, 2006.
- [30] M. Tomasi, B. Cappellini, A. Gregorio et al. Dynamic validation of the Planck-LFI thermal model. *Journal of Instrumentation*, 5:1002-+, 2010.
- [31] L. Terenzi, M. J. Salmon, A. Colin et al. Thermal susceptibility of the Planck-LFI receivers. *Journal of Instrumentation*, 4:2012-+, 2009.
- [32] A. Gregorio, A. Mennella, F. Cuttaia et al. The in-flight calibration and verification of the Planck-LFI instrument. *To be submitted to Journal of Instrumentation*, 2011.
- [33] N. Mandolesi, M. Bersanelli, R. C. Butler et al. Planck pre-launch status: The Planck-LFI programme. *A&A*, 520:A3+, 2010.
- [34] A. Mennella, M. Bersanelli, R. C. Butler et al. Planck early results: First assessment of the Low Frequency Instrument in-flight performance. *ArXiv e-prints*, 2011.
- [35] A. Zacchei, D. Maino, C. Baccigalupi et al. Planck Early Results: The Low Frequency Instrument data processing. *ArXiv e-prints*, 2011.
- [36] M. Bersanelli, N. Mandolesi, R. C. Butler et al. Planck pre-launch status: Design and description of the Low Frequency Instrument. *A&A*, 520:A4+, 2010.

-
- [37] A. Mennella, M. Bersanelli, C. Burigana et al. PLANCK: Systematic effects induced by periodic fluctuations of arbitrary shape. *A&A*, 384:736-742, 2002.
- [38] M. Seiffert, A. Mennella, C. Burigana et al. 1/f noise and other systematic effects in the Planck-LFI radiometers. *A&A*, 391:1185-1197, 2002.
- [39] T. Poutanen, D. Maino, H. Kurki-Suonio, E. Keihänen and E. Hivon. Cosmic microwave background power spectrum estimation with the destriping technique. *Monthly Notices of the Royal Astronomical Society*, 353:43-58, 2004.
- [40] E. Keihänen, R. Keskitalo, H. Kurki-Suonio, T. Poutanen and A.-S. Sirviö. Making cosmic microwave background temperature and polarization maps with MADAM. *A&A*, 510:A57+, 2010.